ANALYSIS OF MODE I FATIGUE CRACK GROWTH IN CARBON FIBRE REINFORCED POLYMER LAMINATES

by

Joseph Anthony O'Gara

A Thesis

Submitted to the Faculty of Purdue University

In Partial Fulfillment of the Requirements for the degree of

Master of Science in Aeronautics and Astronautics

School of Aeronautics and Astronautics

West Lafayette, Indiana

December 2021

THE PURDUE UNIVERSITY GRADUATE SCHOOL
STATEMENT OF COMMITTEE APPROVAL

Dr. Michael Sangid, Chair

School of Aeronautics and Astronautics

Dr. Tyler Tallman

School of Aeronautics and Astronautics

Dr. Alten Grandt

School of Aeronautics and Astronautics

Approved by:

Dr. Gregory Blaisdell

ACKNOWLEDGMENTS

I wish to thank the Royal Australian Air Force for funding my study and living expenses whilst here in the United States.

Secondly I wish to sincerely thank Dr Michael Sangid for his mentoring, assistance, direction, patience and expertise without which this work would not have been possible.

Witchita State University contributed their time, expertise and materials for the creation of the all specimens used in this work and for this I am very grateful.

Additional thanks are made to Dr Imad Hanhan for this work in scoping this work and assistance in specimen design and specimen polishing, Dr Greg Scofield for his assistance in Impact specimen creation, Sven Gustafson for his assistance in lab access and specimen polishing, as well as John Ferguson, Brandon Mackey and other members of the ACME2 lab for their expertise and company during my time here in West Lafayette.

Many thanks to Dr Alten Grandt and Dr Tyler Tallman for giving up their time to be on my defence committee - it is greatly appreciated.

Lastly sincere thanks to my girlfriend Hilary for her patience and support during the course of this work.

TABLE OF CONTENTS

LIST OF TABLES

LIST OF FIGURES

ABSTRACT

With the growing use of composites in aircraft structures to decrease weight, there is a necessity to apply a damage tolerant lifing methodology to increase safety. The strain energy release rate (SERR) range ($\Delta\sqrt{G}$) has been shown to itself not be a similitude metric in literature (like ΔK for metals), however it can be used as the basis for the modified Hartman-Schijve similitude parameter ($\Delta\kappa$) which has solid support for being such a parameter. Most literature on damage tolerance in composite materials study delamination growth in double cantilever beam (DCB) specimens which only look at damage growth in a single dimension and therefore does not take into account the growth interactions of intralaminar and interlaminar damage in a multi-directional ply layup as would be used in real aerospace applications. This study examined these interconnected damage growth mechanisms in two multi-directional layups in Compact Tension specimens, with and without pre-existing damage in order to examine SERR. This work has shown that SERR range appeared to have a connection to increasing damage across the lead crack cross-section in both damaged and undamaged specimens. Baseline specimens had increased delamination lengths at higher SERR ranges, and compression damaged specimens had increasing intralaminar crack quantities in plys perpendicular to the lead crack direction. Regardless, large amounts of scatter was seen in the 18 tests carried out, well above that seen in DCB test literature. Analysis through the average SERR per cycle (G^*) proved to produce less scatter and more intuitive results, and may work well as a similitude parameter. This study has shown more complex fatigue scenarios in composite materials beyond 1D delamination growth must also be understood for any similitude parameters proposed. This will allow for more well rounded understanding of composite material fatigue performance in aerospace applications.

1. INTRODUCTION

The first commercial aircraft composite primary structure was the Boeing 737 horizontal tail in 1984[1]. The structure was certified at this time using the 1984 Federal Aviation Authority (FAA) Airworthiness Advisory Circular 20-107A[2] which allowed for the use of a test-based no-detrimental damage growth design philosophy. This philosophy is akin to safe-life methodology in metals.

Since this time, the use of composite structure on aircraft has increased significantly with aircraft such as the Boeing 787 Dreamliner [3] and the Lockheed Martin F-35A [4] having almost entirely composite skins, leading to a 30-40% ratio of composite structure to aircraft weight. Whilst many decades have passed the composite structure on the Boeing 787 is still lifed under a no-detrimental growth philosophy[3], primarily through test.

The continued use of a non-detrimental growth strategy is inherently costly in terms of money spent on testing, and due to conservatism greatly increasing composite laminate thickness and therefore aircraft weight. In 2009 the FAA released updated guidance[5] which allows composite materials to be lifed under a damage tolerant system as long as growth was shown to be slow, stable and consistent.

This updated guidance has increased the amount of research into fatigue damage growth in composite materials. The majority of this work specifically focuses on fatigue delamination growth, looking at delamination growth in double cantilever beam specimens.

1.1 Research Gap

Double cantilever beam (DCB) tests allow for the analysis of one dimensional delamination growth within a composite laminate. They however disregard the inherent link between intralaminar (through-ply) and interlaminar (between ply) matrix damage growth in a complex multi-directional composite laminate. Whilst not evident from DCB test loading, these mechanisms have significant interactions and may even compete for growth. These factors may be equally as important to understand and quantify in a composite damage tolerant analysis.

Further there are also concerns as to how inherent testing artefacts from DCB testing such as fibre bridging influence Strain Energy Release Rate (SERR) parameters and therefore how the use of DCB test data applies in the creation of a composite fatigue crack growth similitude parameter.

1.2 Research Contribution

This research will conduct fatigue tests to assess slow crack growth metrics in carbon fibre reinforced polymers in a multi-directional layup using a more complex stress state than what is seen commonly in literature.

This work specifically aims to:

- Assess the efficacy of the maximum SERR and SERR range in describing fatigue crack growth in Mode I loading of Compact Tension specimens.
- Assess presently proposed similitude parameters $\Delta\kappa$ and dU/dN (or dU_{cycle}/dN) for their ability to numerically describe various loading and material configurations that should affect damage tolerance.
- Analyse damage growth along the lead crack in a multi-directional laminate through microscopy.

2. LITERATURE REVIEW

The analysis of a material's characteristics is fundamental to its use in engineering design. Therefore with the increased use of composite materials in aerospace since the 1950s and 1960s, a significant amount of research has been carried out into these new materials, their properties and failure modes.

This chapter will provide an overview of composite materials and further review information available on the fatigue loading of carbon fibre composite laminates and their associated failure mechanisms.

2.1 Composite Material Overview

Composites are a general term for the description of using a combination of two different materials to produce an enhanced material with the benefit of both material properties.

Baker et al. [6] describes that fibre reinforced polymer (FRPs) composites are the those where a filamentry-phase material is embedded in a continuous matrix phase. Baker et al. note that fibres which are commonly created from glass or carbon can take numerous forms, such as continuous, discontinuous and whiskers. These fibres may be aligned or randomly orientated within the matrix material. The matrix material is often epoxy resin, but like fibres, there are multiple options for designers, each with their own pros and cons.

From the two constituent materials, composite plys can be formed in various orientations, with multiple plys being able to be adhered together to form a composite panel of low weight and significant strength. Baker et al. note that this process normally requires an elevated temperature cure which requires a vacuum to remove retained air from within the layup, and an elevated temperature to melt the matrix material to bond it to the fibres. Typical matrix materials cure at elevated temperatures (120-180 °C for epoxy).

2.1.1 Fibre Overview

Fibres are of significant strengths and stiffness but due to their length-width ratio are very susceptible to buckling related failure modes. Fibres are the primary load carrying

material within a composite, but their orientation must be carefully considered in order to only carry tensile loads.

Baker et al. [6] state that fibres used in composite materials are generally single elements, or compounds of, low atomic number such as Carbon, Boron, Aluminium or formed from organic compounds that have long chain molecules including carbon, hydrogen or nitrogen, in order to create fibres such as Aramid or Kevlar. They note that once formed from manufacturing processes such as chemical vapour deposition (CVD) for Boron, or pyrolysis for Carbon, fibres can take forms such as single filaments, whiskers (short but stiff fibres of large length-to-diameter ratios), or even nanotubes. Each individual fibre can have a diameter in the order to microns - with carbon having fibre diameters as low as $5\mu m$.

Discussing carbon fibre, Baker et al. [6] state that carbon fibres used in aerospace applications are generally made from the precursor materials - Polyacrylonitrile (PAN) fibres, where PAN is an acrylic textile fibre that is spun to create a circle cross-section. The fibre is then stretched to size and to orientate the molecular chain along the axis of the fibre. Additional steps in the manufacture include oxidisation, carbonisation and graphitisation, which aim to produce a thermally-stable, inert and strong fibre respectively.

Individual fibres are generally woven together to form a weave known as tows. These tows can have as many as 25,000 fibres and when woven, braided or knitted together can form a wide variety of high-strength fabrics.

2.1.2 Matrix Overview

In Baker et al. [6] they discuss the matrix of a composite as providing the basis for the size and shape of the finished composite material. As fibres perform the role of primary load carrier, the matrices are a more compliant material ensures that any load from failed fibres is transferred to other neighbouring fibres. The matrix also supports the majority of any transverse loading, and thus the matrices compressive strength significantly affects the overall compressive strength of the final composite part.

Matrix materials in CFRPs are typically a polymer, though the type of polymer used depends on the required specifications of the composite. Both thermosetting and thermo-

plastics/thermosoftening polymers can be used for the matrix, though thermosetting resins, such as epoxy resins, are typically used in aerospace due their excellent mechanical properties and ability to be formed and set at low temperatures. Bismaleimide resins (BMI) are also commonly used in aerospace where a high temperature environment is envisaged due to BMIs higher melting point, allowing them to have operating temperatures up to 180 °C [6].

Baker et al. [6] states that polymers are built of long chains of molecules, though the molecules can be made to form linear, cross-linked, branched or networked chains depending on manufacturing processes used, with their relative strengths being low to high respectively. Polymers with three-dimensional network chains form thermosetting polymers after curing in the presence of a curing agent/hardener, typically at an elevated temperature. Resin epoxies fit in this category and as a thermosetting polymer, undergo irreversible chemical changes that make them not possible to be melted and reformed. Resins before curing are free-flowing which allows them to be added to a fibre layup with little change to fibre orientation.

When epoxy resins cure, it is possible for multiple chemical reactions to occur even if the temperature and other environmental elements are unchanged [6]. These alternative chemical compositions are why it is imperative that the exact cure cycle per the manufacturers data is followed. In a typical epoxy, as it cures the resin will go through a low viscosity state, fuelled by externally applied heat. This step ensures that the complete circumferential surface area of the fibres are covered with resin. After being held at a constant temperature, local viscosity increases significantly as the resin extends its molecular chains. Gelation then occurs within the resin - a process that encourages the long molecular chains to cross-link with other chains. Cross links now being formed stops any further flow or movement by the resin. The final step is know as vitrification where the chemical reactions finishes. The epoxy resin cure cycle can be see in Figure 2.1 below.

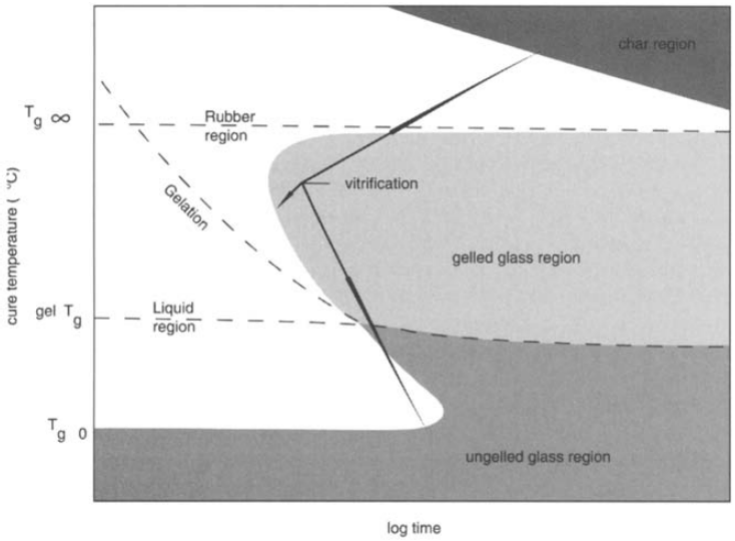

Figure 2.1. Resin cure cycle [6]

2.1.3 Composite Ply Layups

Composite structure in aircraft has traditionally been continuous fibre multi-ply laminates. As described previously, fibres only have stiffness and therefore load carrying ability in the longitudinal/axial direction, and thus fibre direction relative to the loading is crucial. If multiple plys are stacked at different angles to each other it is possible to get a strong component in multiple directions. A composite stacked with plys at 0°, 45°, 90 °, -45° will have relatively isotropic mechanical characteristics[6]. The following are explanations of important composite ply terminology.

Layup Angles

Individual plys are aligned within with layups in order to meet a design property (stiffness or strength) that is required. Plys are orientated at angles from -90° to 90° relative to the loading axis (defined as 0°) with the longitudinal fibre direction defining the angle of a uni-directional ply.

Symmetric Laminates

Symmetric Laminates are those that have a symmetric ply angle layup with respect to the mid-plane of the composite laminate[7].

Balanced Laminates

Balanced laminates are defined as having no stretching or shear coupling, which in general means that for every ply of $+\theta$ there is an opposing ply of $-\theta$ of the same thickness and material[7].

2.2 Fatigue

As discussed in the introduction, the current understanding of slow fatigue crack growth within a composite material is still unable to life composite primary structure without the aid of a significant amount of testing. This section will identify the core concepts of fatigue growth in CFRP composite materials.

2.2.1 Fatigue Overview

When composite materials started to be analysed for their fatigue characteristics, issues arose due to the many assumptions embedded in fatigue analysis techniques that were based upon isotropic, homogeneous behaviour. This basis, along with the assumption that the material can be cyclically loaded a stress state lower than its maximum stress and fail is not-necessarily applicable to composite materials[8]. Additionally, metallic crack growth also normally revolves around a single crack that grows with each cycle - a concept that does not carry over to composite materials due to the complex interaction of damage between and across plys as will be discussed in Section 2.3.

As composites have a naturally high resistance to fatigue, it was once common to believe that composite materials did not exhibit fatigue crack growth behaviour at all. This understanding typically came from the notion that because of the high stiffness levels of the composite in the fibre direction, strain levels required to initiate damage in the fibres to any

meaningful level could be designed out. In action, this methodology meant that composite materials would be over-designed for their particular application in order to ensure a low applied stress/strain as a percent of their maximum allowable - at significant cost to cost and weight. Additionally due to the anisotrophy of composite layups, even unexpected small out-of-plane loads/strains could cause damage initiation and growth resulting in eventual failure. The growth of damage in CFRPs is therefore an important concept for research and study in aerospace.

In this work, Mode I crack growth will primarily be addressed. Mode I fatigue is the crack opening mode which addresses load applied in-plane in the 2-direction.

2.2.2 Damage Progression in Fatigue Loaded Composites

Damage initiation in a composite material can occur even at low stress levels. This damage can occur anywhere in the stressed region but may not reduce the overall strength of the material but rather only decrease the material's stiffness [8]. In fact these small failures can slightly improve composite strength by increasing fibre alignment. This is in part why at sufficiently low loading, crack growth curves may flatten out or stop growing all together.

As the number of cycles increases, so does the damage accumulating within the stressed region. Once this damage reaches a critical point, the residual load capacity can be reduced beneath that required to support the maximum load within the fatigue cycle, as seen in the Hashin-Rotem cumulative-damage theory. Fracture occurs at this point as seen in 2.2a. It has also been shown that after the initial reduction in stiffness, a further stiffness reducing may not occur until directly before fatigue failure, particularly in CFRPs [8].

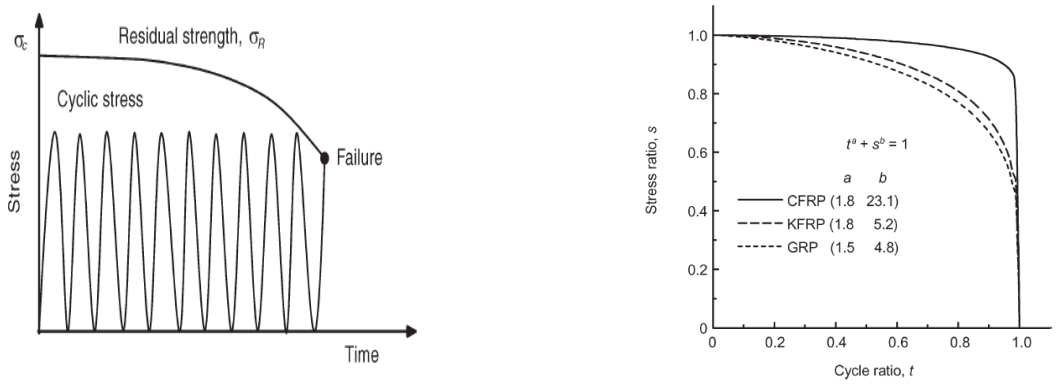

(a) Hypothetical [8] (b) For a group of real specimens [8]

Figure 2.2. Damage propagation leading to residual strength failure

This effect can be significant as illustrated in a study by Stinchcomb et al. [9]. A multi-ply composite fibre-reinforced polymer (CFRP) composite with a through hole was monotonically loaded to failure. A specimen of the same design was then cyclically loaded for a number of cycles. The specimen was then monotonically loaded as before. It was found that the fatigue loaded specimen had a tension strength of 126% of the specimen that was not cyclically loaded, owing to the fact that very early on in the cyclical loading, cracks had emanated from the through-hole to relieve stresses and reduce stress concentrations present. This ability to stress relieve and not-reduce the overall strength of the part is a core feature of a continuous fibre reinforced composite material.

In a particular study of damage growth in a CFRP under uni-axial tension it was found that there were five stages of damage growth[9], as seen in Figure 2.3.

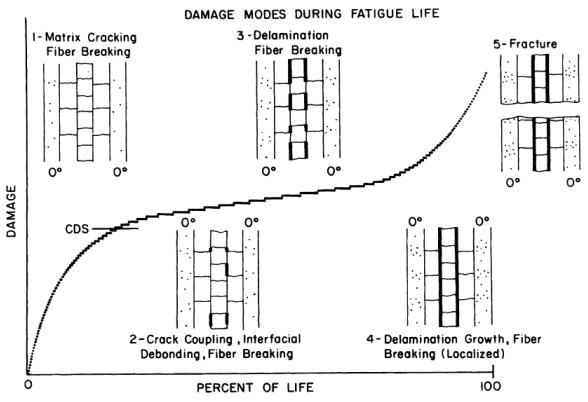

Figure 2.3. Damage occurring through fatigue life of a composite [10]

The stages of damage growth were:

1. Matrix Cracking and Fibre Breaking. Damage initiates at a rapid rate.
2. Crack coupling, interfacial debonding and fibre breaking.
3. Delamination and Fibre Breaking.
4. Delamination Growth, and localised fibre breaking.
5. Fracture.

2.2.3 Damage Tolerance of Composites

As per [5], aircraft composite structures must be lifed in accordance with a damage tolerant (slow growth) or safe-life (no-detrimental crack growth) philosophy. At present, the application of a no-detrimental crack growth philosophy is easier to apply as it requires less analysis and instead relies on a series of tests in a build-block approach to prove that no damage growth is expected over the life of the final part. These tests look for both visible and non-visible damage expected to occur through the design life.

Ideally, and as is required for the application of a damage-tolerant/slow-growth approach, the fatigue life of a CFRP component could be predicted based on a set of material and loading parameters. Unfortunately this analysis has unresolved issues surrounding the the strength of a CFRP material due to damage progress through out the material – a problem exacerbated by trying to analytically characterise damage growth in a cyclical loading regime[11].

Additionally, in contrast to metal fatigue where crack growth is perpendicular to the loading direction (for Mode I), this is not the case for composites. Instead the composite may fail through a complex network of intralaminar, interlaminar damage and fibre failures, which are often parallel to the load axis[4]. This is the crux of the problem for damage tolerant analysis in composite fatigue. It requires a qualitative and quantitative understanding of complex damage initiation, growth and interaction under fatigue loading, making it hard to simulate and reliably predict.

Additional issues surround the historical conduct of fatigue testing of composites which predominately look at single axis loading which in unlikely to be fully applicable of real

life loading. Without a detailed understanding of composite damage growth, composites will continue to be oversized for their application within aerospace removing potentially reducing the cost benefit over traditional metal structure [12].

2.2.4 Crack Driving Force in Composites

In order to certify composite structure without extensive tests through the slow crack growth methodology offered per FAA AC 20-10B [5], the lifing needs to be both slow and predictable. To be predictable testing of the material needs to be able to uniquely characterise its slow crack growth for its geometry and load, known as the similitude parameter. In metals, for comparison, this parameter would be the ΔK (Stress Intensity Factor Range $K_{max} - K_{min}$) parameter which when plotted against the crack growth rate, da/dN, provides a unique fatigue crack growth curve for each material. That is, every crack exposed to the same similitude parameter quantity in the same material will grow at the same rate.

Initial search for such a parameter in composite materials looked specifically at the ΔG parameter ($G_{max} - G_{min}$), that is, the strain energy release rate (SERR) per cycle of the material, or even the maximum strain energy release rate in a cycle, G_{max}. The SERR, G, can be found from Equation 2.1, where $P = P_{max}$ for G_{max}, and $P = P_{min}$ for G_{min}.

$$G = \frac{1}{2t} P^2 \frac{dC}{da} \tag{2.1}$$

However, the use of the SERR, G, and its derivatives G_{max} and ΔG, is susceptible to scatter and does not produce a viable similitude parameter. Moreover it has been shown to produce non-physical results, such that increasing R-ratio leads to a reduction in SERR, or a change in pre-crack length changes the crack growth rate [13, 14, 15, 16, 17, 18, 19]. Yao et al. [20] states when using G_{max} delamination growth can be shown to decrease with increasing stress-ratios, whilst when using ΔG the opposite can be shown.

Further work by Jones et al.[14] introduces the SERR parameter $\sqrt{\Delta G}$ which mathematically aligns the SERR, G, with the initial Paris formulation for the stress intensity factor K, showing that G is actually proportional to K^2. A number of other issues arising from the use of the ΔG parameter are listed by Jones et al.[14], all of which are negated with the

implementation of a revised da/dN formulation in the form of a modified Hartman-Schijve equation, shown in Equation 2.2, taken from [18].

$$da/dN = D\left[\frac{\Delta\sqrt{G} - \Delta\sqrt{G_{thr}}}{\sqrt{(1 - \sqrt{G_{max}/\sqrt{A}}}}\right]^n \tag{2.2}$$

where

$$\Delta\sqrt{G} = \sqrt{G_{max}} - \sqrt{G_{min}} \tag{2.3}$$

and the fatigue threshold is found by

$$\Delta\sqrt{G_{thr}} = \sqrt{G_{thr.max}} - \sqrt{G_{thr.min}} \tag{2.4}$$

n and D are constants, and A is the cyclic fracture toughness.

Jones [18, 21] states that plotting Equation 2.2 verse da/dN results in a unique material curve that is independent of material thickness, temperature, laminate and adhesive thickness, R-ratio, pre-crack length and ply configuration which should allow the analysis of delamination growth in composites.

It is worth noting that most authors are only looking at delamination growth within a CFRP, with the vast majority of research looking at delamination resistance in double cantilever beams (DCB) using various material and layup types. This is in the guise that delamination is the quickest growing and most damaging form of damage growth within a fatigue loaded CFRP [22]. There has however been discussion about the propensity of the DCB derived similitude parameters to work in complex stress states [23] that have more than one damage type, or when the material has a different fracture toughness in the interlaminar and intralaminar directions [24].

Other authors discuss the use of the maximum SERR and the SERR Range as the crack driving force as misguided. In Irwin's work [25] for example it is stated that the SERR is not the cause of crack extension but the result. Amaral et al. [26] discuss that SERR parameters; G_{max}, ΔG and $\Delta\sqrt{G}$ and other G derivatives, as able to be obtained from measured fatigue data (crack length, force and displacement) and provide a energy release rate output even

if there is no crack extension. The study continues to describe these SERR parameters as not having a physics based theory behind them. This is also supported by others in the field [27].

Amaral et al. also discuss authors such as Murri [28] who have normalised fatigue strain energy release rates against fracture toguhness, G_{IC}, which they argue has no theoretical basis. Murri states that the normalisation of delamination resistance curves enable fibre bridging effects to be taken into account in the fatigue test data. The normalisation of the data worked well in Murri et al.'s study of double cantilever beam specimens but it may be harder to apply to other specimen types. Yao et al. [15] similarly states that normalisation is incorrect unless the damage growth method is the same or very similar.

An alternative master relationship is offered by Yao et al.[20] in Equation 2.5, however the author admits the model which works well has an unknown physics basis.

$$\Delta G_{eff} = f(G_{max}, \Delta G) = \Delta G^{[1-(\frac{G_{max}}{G_C})^{\gamma}]} G_{max}^{[1-(\frac{G_{max}}{G_C})^{\gamma}]} \tag{2.5}$$

Alternatives to the majoritively used SERR G based similitude parameters include Griffith energy balance methods which aim to quantify change in amplitude of potential stored energy (U) per cycle. In a similar way to G, the slope of the this curve per cycle, dU/dN is shown against da/dN. Yao et al. [15] also state that fibre bridging effects are less present within fatigue crack growth data in the form; da/dN vs. dU/dN which makes it promising for use. Two forms of the Griffith energy balance are expressed in Equation 2.6 and 2.7.

$$U = \frac{1}{2} P_{max,N} \delta_{max,N} \tag{2.6}$$

$$U_{cycle} = \frac{1}{2} P_{max,N} \delta_{max,N} - \frac{1}{2} P_{min,N} \delta_{min,N} \tag{2.7}$$

Amaral et al. [26] present the parameter, G^* as a theory based alternative, where G^* is the average strain energy release rate in a cycle which has the benefit of being able to be normalised against the quasi-static fracture toughness. G^* is defined in Equation 2.8.

$$G^* = \frac{1}{b}\frac{dU/dN}{da/dN} = \frac{dU}{dA} \tag{2.8}$$

2.3 Composite Failure Mechanisms

A broad overview of damage types was given in previous chapters however this chapter will have a deeper look at damage that occurs in CFRPs under fatigue loading.

2.3.1 Intralaminar and Interlaminar Failure

Both intralaminar and interlaminar damage mechanisms are matrix failure mechanisms. Intralaminar failure is failure of the matrix transverse to the fibre direction, whilst conversely interlaminar failure is failure of the matrix parallel to the fibre direction (through the thickness of a composite), between adjacent plies of a multi-ply composite. Together these mechanisms form the method for which damage can propagate through a composite matrix.

The above differentiation between interlaminar and intralaminar failure can be seen in Figure 2.4.

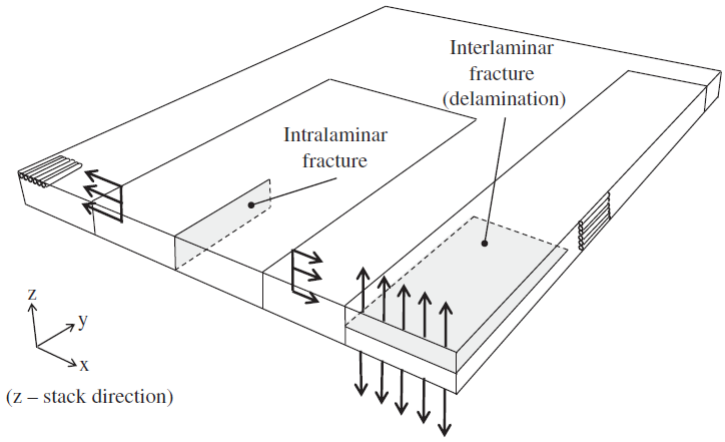

Figure 2.4. Interlaminar and intralaminar failure [24]

Both intralaminar and interlaminar cracks are inherently linked in CFRP materials, with delamination typically being initiated from intralaminar damage. Delamination growth has

a reduced energy cost due to the inferior properties (strength and toughness) of the ply-ply interface region due to the increased volume of the epoxy resin located between plys [29]. In the work of Ni et al. [29], they found using both microscopy and micro-computed tomography that intralaminar cracks typically bifurcate into the interlaminar region due to the inherent weakness of the area. To mitigate the inherent reduced strength of this interlaminar space, Ni et al. introduce aligned carbon fibre nanotubes in the transverse direction between plys which allowed for a 10% increase in interlaminar fracture toughness due to the damage growth being forced into the intralaminar region, parallel to the ply-ply interface.

Altus et al. [22] showed in their study the intrinsic relation between both interlaminar and intralaminar cracking. They stated that transverse cracks originate on the outer ply and propagate until an adjacent ply is reached (Figure 2.5a). More intralaminar cracks will then form surrounding the original crack causing a dense array of cracks (b), leading to high localised stresses on the second ply leading to delamination initiation (c) and growth (d).

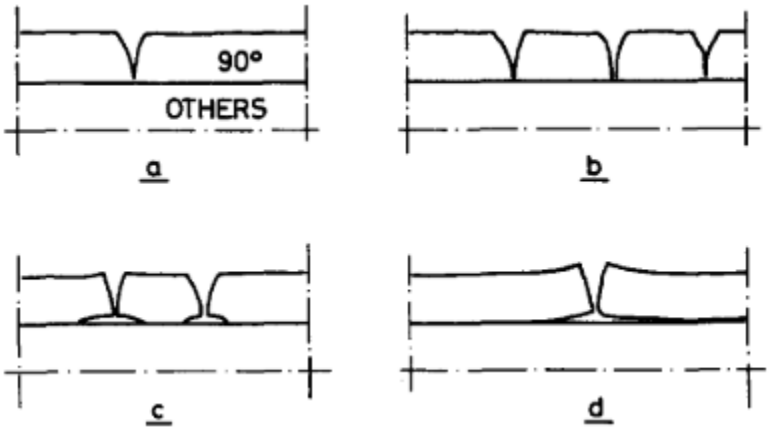

Figure 2.5. Delamination formation [22]

The stresses found at the crack tip of a transverse (interlaminar) crack sheds some more light on why delamination accompanies intralaminar cracks between plys. Figure 2.6 shows the contours of equal maximum principle stress surrounding an intralaminar crack as found in [22]. The figure shows that the contours have an increased derivative, or increased separation, in the x-direction (interlaminar or delamination direction) which the author postulates will

be the direction of crack extension. This should mean that it is energetically favourable for an intralaminar crack to evolve into a delamination.

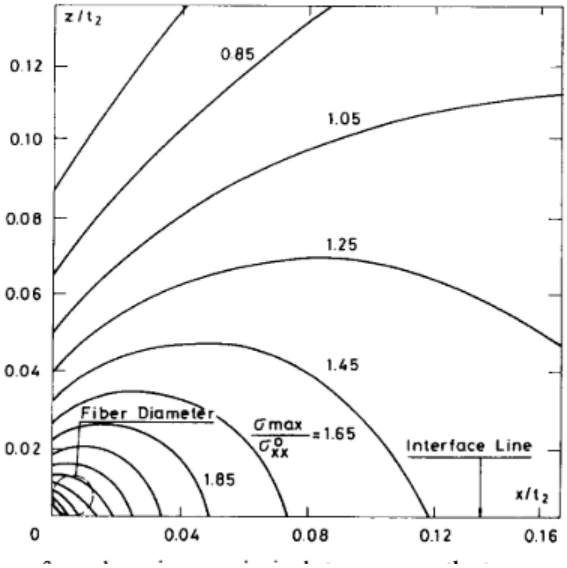

Figure 2.6. Intralaminar crack tip stress distribution [22]

A study by Czbaj et al. [24] looked at Compact Tension (CT) and Double Cantilever Beam (DCB) specimens to determine and compare the interlaminar and intralaminar fracture toughness in an IM7/8552 CFRP. Fatigue pre-cracking of 1mm was used additional to the cut notch in the CT specimens. The author found that the interlaminar and intralaminar fracture toughness were essentially equal for both damage mechanisms when crack growth was parallel to the fibre direction.

Wang et al. [30] found in their study of interlaminar crack tip intensity factors in a balanced, symmetric CFRP of layup $[\theta/–\theta/–\theta/\theta]$ under uni-axial tension, that the tearing-mode stress intensity factor (K_{III}) was two orders of magnitude higher than K_I and K_{II}. Further, they discuss that G, the energy release rate and driver force for delamination fracture, is smallest when $\theta = 45°$ which led them to the believe that intralaminar cracking is more likely to occur than delamination.

2.3.2 Visualising Composite Failure

The use of non-destructive testing (NDT) techniques are very important for the assessment of damage growth within a composite layup. Due to CFRP materials having a series of angled plys, it is impossible to visually assess the delamination growth between plys or intralaminar cracks on plys that are not on the exterior of the layup. NDT methods such as computed tomography (CT) and ultrasonic testing bridge this gap by allowing sub-surface damage to be visualised. Computed tomography will be the focus of this inspection however Figure 2.10 shows the inspection of impact damage using ultrasonic testing.

In a particular study completed by Ortiz-Morales et al. [31] regarding damage growth in tensile monotonic testing of both $[+45]_6$ and $[+45/-45/+45]_s$ T650/5320 CFRP compact tension specimens using Synchrotron-based X-ray microcomputed tomography (μXSCT). As the specimens were monotonically loaded, the damage around the notch tip was periodically examined. The micro-CT image data was then segmented and analysed to determine the size and amount of damage that had accumulated at each load level, which once viewed in sequence allowed the visualisation of damage growth within a multi-layer CFRP. Numerous other studies have completed similar work including [32, 33].

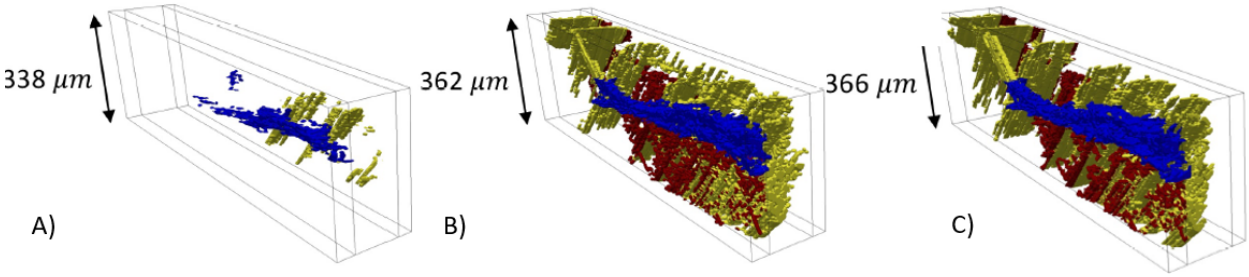

Figure 2.7. Damage found in a $[+45/-45/+45]_s$ T650/5320 CFRP under monotonic tension loading at A) $F = 0.3F_{ULT}$, B) $F = 0.95F_{ULT}$, and C) $F \approx F_{ULT}$. Extracted and rearranged [31].

Figure 2.7 shows that damage that accrued in the composite layup across all plys. Through further analysis, the author quantified the damage found at the notch tip as that in Table 2.1.

Table 2.1. Damage Percent of Overall Damage. Extracted from [31]

Load Level	**Intralaminar Cracking Present [%]**	**Delamination Present [%]**
$F = 0$	0	0
$F = 0.3F_{ULT}$	100	0
$F = 0.6F_{ULT}$	98.7	1.3
$F = 0.95F_{ULT}$	82.5	17.5
$F \approx F_{ULT}$	79.8	20.2

The research found that the first damage initiated in both layup types was intralaminar cracking. When this damage initiated, fibre breakage was only occurring at the notch tip for the $[+45/-45/+45]_s$ specimen. Fibre breakage only occurred in the $[+45]_6$ specimen near fracture. It was found that for the $[+45/-45/+45]_s$ specimen, as the matrix damage grew, there were consistent fibre breakage events, with matrix cracking leading to 54 out of 82 (66%) of all fibre breakage events. Fibre bridging was found in neighbouring +45 degree plys however there was no evidence of fibre bridging in adjacent $+45/-45$ plys.

In the $[+45/-45/+45]_s$ specimen, the combination of intralaminar cracking and delamination did not occur until over halfway to ultimate load. The delaminations that occurred appeared to be a stress relieving mechanism for the layup, to allow the intralaminar crack to transition to adjacent plys orientated in the oppose layup direction, increasing the ductility of the specimen overall.

In a further study by the same authors, Hanhan et al. [34], used the same μXSCT setup to understand damage initiation and growth in the same $[+45/-45/+45]_s$ specimen under tension-tension fatigue loading. The testing was carried out under force-control with a $P_{max} = 0.8F_{ULT}$, R=0.5 and at 1Hz for a total of 5802 cycles. Using image segmentation and scripted MATLAB crack length detection, a crack growth curve for the lead crack was created. FEA was then used to sequentially apply the incrementally growing crack size and geometry to a model CT specimen, allowing for the applied work (U) of the specimen to be

calculated at each cycle with each damage present in the composite. The stored energy per cycle for crack growth (dU/dN) in a ply was then calculated.

Cracks grew quickly in the experiment with the lead cracks growing in excess of the tomography window of 1.6mm within the first cycle. Intralaminar cracking continued to be the most prevalent damage type as per [31] but delamination was seen to grow to a higher percent of the overall damage amount after 330 cycles. In contrast to the original monotonic study [31], fibre bridging was seen to occur in adjacent oppositely orientated plys for a large amount of cycles. The change in energy per cycle for experimentally found cracks in each ply can be seen in Figure 2.8. The figure shows that the da/dN vs. dU/dN curve for intralaminar cracking collapses to a single line approximately 10^{-2} higher than that expected for delamination from literature.

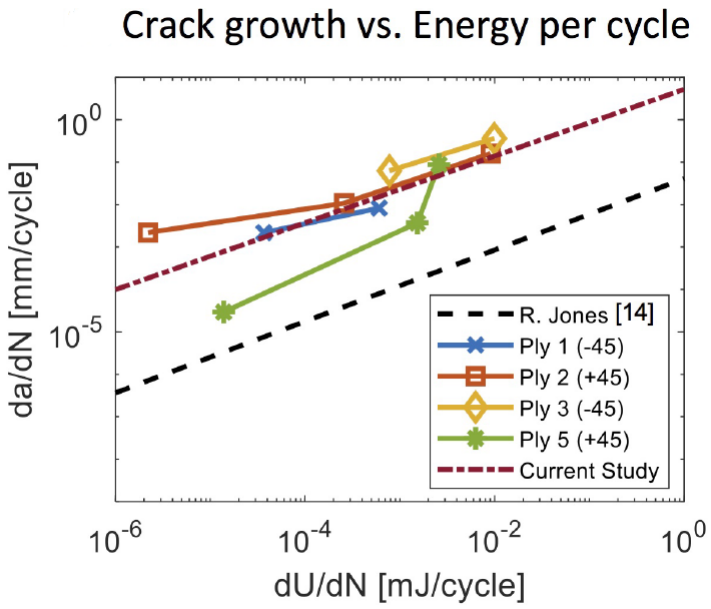

Figure 2.8. Change in energy per cycle for experimentally found cracks in each ply [34].

2.3.3 Impact Damage

Significance

Impact damage is a very common form of operational damage for aircraft. As discussed in the introduction section, the FAA, as part of AC 20-107B [5], has introduced the need to

ensure that aircraft designers show that impact damage possible during the aircraft's service life does not reduce the structural strength of the part below ultimate load capability or grow to such a size through the operational life of the aircraft. To help with this, the FAA included Figure 2.9 and descriptions of each impact damage severity reasonably expected to occur in an aircraft's life and accompanying discussion as to an acceptable qualitative no-growth or slow growth life before repair.

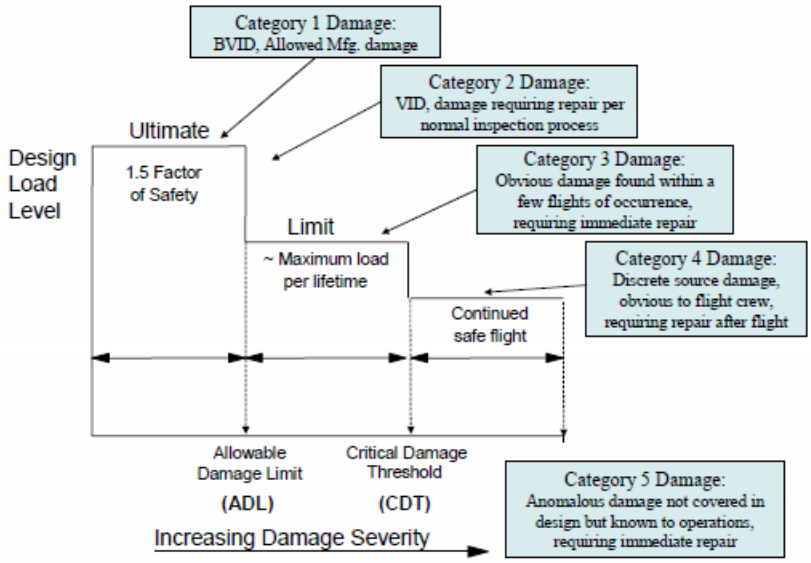

Figure 2.9. FAA impact damage severity classification guide [5]

The work of Feng et al. in [35] shows the significance of BVID on aircraft structure. 50J impacts were introduced to a structure similar to that of a composite stiffened panel found on a fuselage. Whilst damage appeared small from the impact side of the structure, the true size of the damage could be large, as seen in Figure 2.10 where the true damage size was $499mm^2$ as seen by C-scan ultrasonic non-destructive testing. This shows the value of BVID fatigue analysis as required by the FAA in [5].

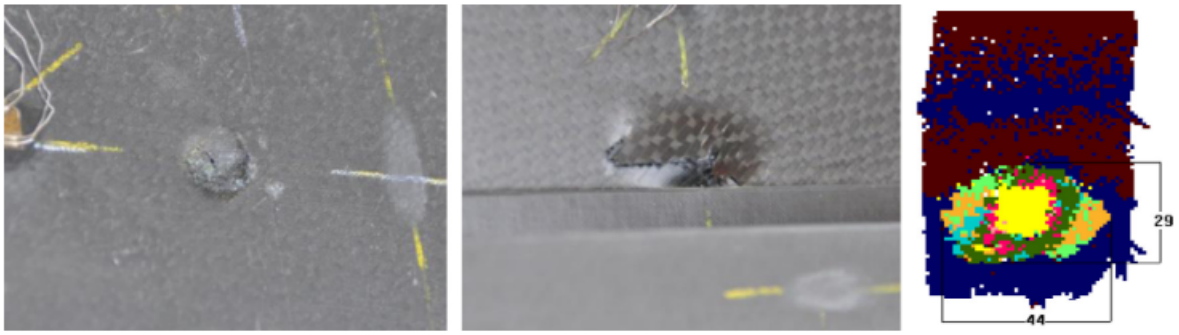

(a) Front face (b) Rear face (c) C-scan image

Figure 2.10. BVID Impact [35]

Damage Mechanism

Impact damage in CFRPs is a complex damage type due to its ability to cause multiple damage types and sites within the composite layup. Damages that can occur include fibre breakages from tension and fibre kinking damage in compression from the large deformations that occur in the structure, as well as shear driven delamination from the stiffness of the material resisting the deformation [36]. This results in an overall "peanut" shaped damage area as seen in Figure 2.11.

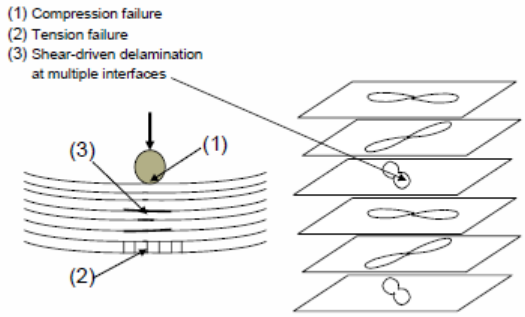

Figure 2.11. Impact damage damage pattern [36]

Damage creation in the composite layup is discussed in Hull et al.'s [37] work. They investigated damage tolerance on composite materials from BVID. Analysis showed how the imparted (impact) energy would arrange itself as damage within the composite layup. In their work they showed that delamination growth was always initiated by large intraply

cracking, regardless of ply layup and orientation. This was due to the imparted transverse shear stress from the impact causing matrix failure in the form of intraply cracks. These cracks were unable to continue propagating transversely when they reached adjacent plys and then were forced to devolve into delaminations at the ply-ply interfaces, as seen in Figure 2.12.

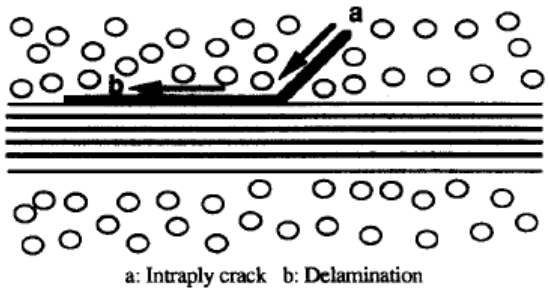

Figure 2.12. Intralaminar crack to delamination evolution [37]

Further, Hull et al. [37] found that the size and shape of the delaminations that were initiated from impact damage was influenced by the ply layup and part geometry near the impact. The delaminations that were created by the impact was the predominate method for energy dissipation and thus the interlaminar shear fracture toughness of the composite had a direct link to damage size. This is seen in Figure 2.13.

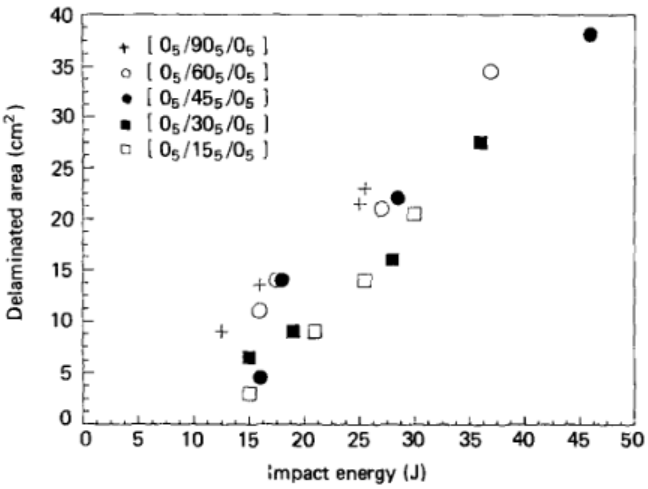

Figure 2.13. Delamination area and impact size [38]

In their analysis of impact sizes, Hull et al. [37] found a linear correlation between impact energy imparted into the composite layup and the area of delamination that occurred. No link was found between the intralaminar crack sizes and impact energy likely meaning that this failure mode likely grew in an unstable fashion.

Impact and Fatigue

The majority of datasets about the growth of impact damage are related to the compression after impact (CAI) case due to its increased critically over tension-tension load cases however the majority of aircraft structure is loaded in tension-tension fatigue. Compression based fatigue is generally more critical due to the impact created delaminations promoting buckling of the composite[36] which can cause sudden failure. Fortunately, tension-tension fatigue is seen to have a much less drastic effects as seen in Han's work [39], where only the CAI samples failed in fatigue loading. The damage did progress in the tension-tension case only when the load applied was above 40% ultimate strength.

A paper by Pascoe et al.[27] succinctly looks at the application of the slow crack growth method to impact damaged fibre reinforced composites in the CAI case and finds that there are a number of issues collectively with the data presented in a range of research. These issues are equally valid for the tension-tension case.

- Damage Characterisation. There is inconsistency in damage characterisation. NDI methods used, including visual, can misinterpret damage growth under fatigue loading due to overlapping damage from a top-down view.
- Fatigue driven delamination growth. The author states there is a shortcoming in 'how' impact damage evolves under fatigue loading based on a large number of studies using DCB and MMB test methods which can over-simplify the damage interactions, multiply interfaces and two dimensional growth.
- Failure. The failure mode that causes failure is often unknown or otherwise dependant on the laminate layup or damage configuration.

2.3.4 Compression Damage

Significance

Compression damage occurs when a composite is loaded in compression beyond its compressive yield point or buckling limit. A review of available composite fatigue lifing data by Molent et al.[12] found compression dominated loading is the most fast growing loading method. This is due to the fibres having very limited compressive ability without buckling occurring.

In tension-tension loading, damage from a prior-compression event can have significant effects on the composite structure due to buckled plys, matrix-fibre adherence issues or fibre kink band creation.

Damage Mechanism

In a study by Correa et al. [40] of tension-compression cyclic loading on a single fibre glass reinforce polymer, the matrix-fibre debond process was examined. It was found that transverse (intralaminar) cracking occurs in composite plys not orientated in the direction of the load and is actually the amalgamation of multiple disbonds of the matrix and fibres. This debonding (and hence intralaminar crack growth) was found to be more severe for a tension-compression cycle than for a tension-tension fatigue cycle. Inter-facial (fibre-matrix) disbonds from a T-T cycle were created between 0 and 70° of the circumference of a fibre but did not grow in subsequent cycles. T-C loading showed debond growth through to 120 degrees. Similar results were found analytically in [41].

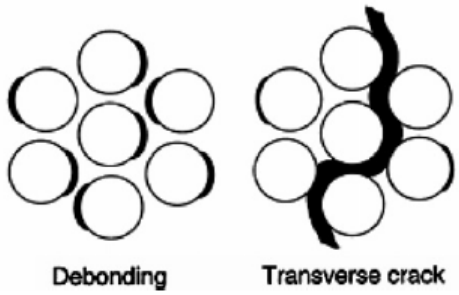

Figure 2.14. Disbond growth into transverse (intralaminar) cracking [40]

Kink banding is a local buckling mechanism of a group of aligned fibres, due to the low compressive strength of a FRP. Kink bands form under compressive stress (σ_c) as per Figure 2.15a, and generate typically with a kink-angle (Φ) and width w due to the aligned fibres negligible bending stiffness. Figure 2.15b shows a microscope picture of a kink band that has occurred, where the number 2 indicates the kink band and 3 indicates fibre-breakage.

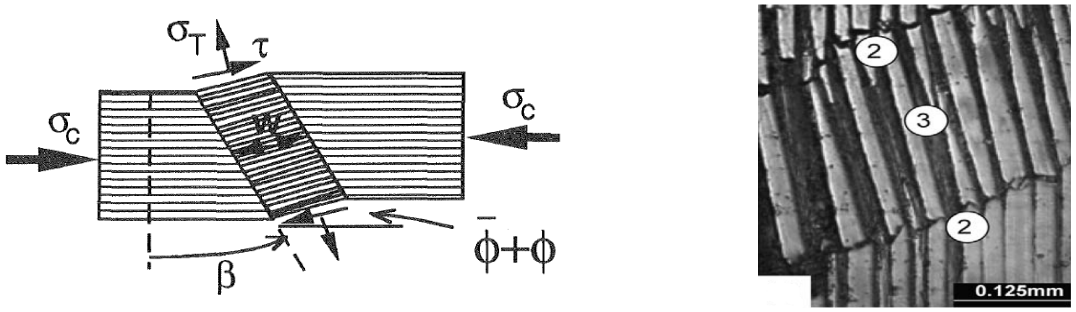

(a) Kink band stresses [42]. (b) Kink band microscopy from [43].

Figure 2.15. Kink band visualisation

Compressive strength of a composite is driven by buckling failure modes, and therefore in its simplest form can be found as a ratio of the elastic shear modulus of the matrix material over the volume fraction of matrix. This method however has been found experimentally to overestimate the strain required to buckle the fibres by a couple of percent. One of the reasons for this over-estimation is that real composite layups have misalignment of fibres which is the reason that the rotation of the kink band equals the angular misalignment of the fibres plus the angular rotation from the shear stress ($\Phi = \phi + \bar{\phi}$)[42]. There are however a large amount of models that aim to predict the onset and size of kink band formations however most seem to be approximations based on buckling and instability analysis with similar mechanics involved in the problem setup.

In study by Kyrxiakides et al.[44] of axially compressed confined CFRP rods, it was seen that under displacement control the load would have a sudden and uncontrolled decrease in force/stress at approximately 1.5% strain, microscopically attributed to the formation of kink planes/bands. One the load drops, further compression will cause the creation of additional kink planes, as seen by the smaller peaks to the right of the major load drop in Figure 2.16. Further investigation found that once failure occurred propagation of further

kink bands could initiate at stress levels much lower than that of the initial failure. This behaviour was described as a form of instability, attributed to a misalignment of fibres within the matrix.

This instability had three phases:

- Initiation phase - System becomes unstable with an associated maximum load reached.
- Localised deformation - Deformation occurs and is then arrested.
- Propagation - The instability grows to a quasi-steady state prorogation at a propagation load lower than the original maximum load.

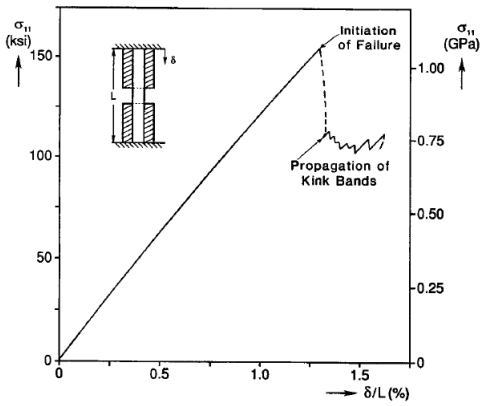

Figure 2.16. Axial stress-end shortening from confined rod experiment [44]

The initiation phase was seen to occur at a force much lower than the compressive strength of a CFRP (AS4/PEEK) by Hsu et al. [45], 70ksi as opposed to its strength of 175ksi.

Experimentally, kink bands have been created in a range of specimen types however most are bespoke. Unidirectional, load aligned (0°) specimens are almost always used however some research has been completed using fibres with a global misalignment [46]. Compact compression (CC) specimens have been used in some literature such as by Pinho et al. [43]. An axially aligned specimen IM7/8442 CFRP (2.17a) was tested in Sataloff et al. [47], which showed some outer ply buckling but the initiation of kink bands in four stages once a larger load drop was achieved.

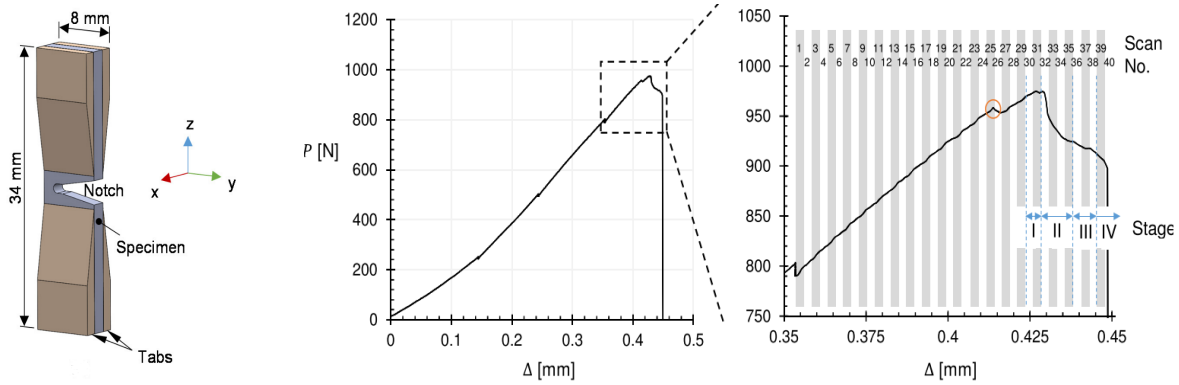

(a) Specimen design [47] (b) Specimen compression loading (c) Kink band stages [47]

Figure 2.17. Axial compression specimen kink band formation

In Pinho et al.'s study of compressive and tensile fracture toughness [43], the energy required for the growth of kink bands was also examined. The study had some success using $[90/0]_{8,s}$ T300/913 CC specimens to form kink bands. This is of interest because a CC specimen is similar to the CT specimens used in this work.

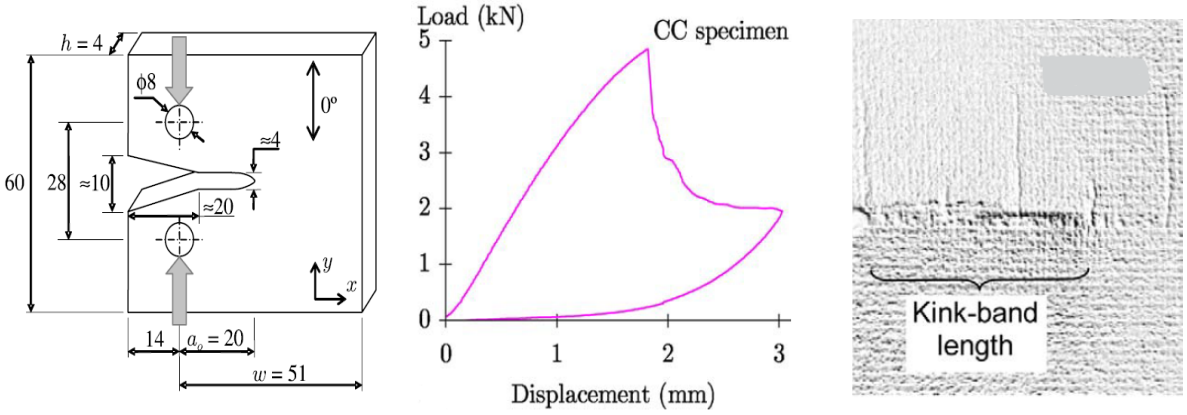

(a) Specimen design (b) Loading of CC specimen (c) Kink Band formation

Figure 2.18. Compact compression specimen kink band formation[43]

Of particular note from this work is that the progression of the kink band was able to be measured in the specimen using a series of subtracted images, where the optically acquired images were subtracted from an image taken five seconds previous. This is seen in Figure 2.18c.

Compression Damage and Fatigue

As discussed earlier, there is a large amount of literature on compression-compression loading being the most significant form of fatigue for composite material[12]. There is also a large amount of information about tension-compression (T-C) loading however there is less information surrounding compression damage and subsequent tension-tension (T-T) loading as will be examined in this study.

A lot of the studies discussed in the Impact Chapter (2.3.3) are applicable to understanding compression damage artefacts with the difference of the damage being in-plane rather than out-of-plane as expected from impact. There is still a large difference to be examined surrounding how a CFRP manages with a large subsection of broken fibres in a small region as would be seen from previous compressive damage. It is possible that in-plane compression (kink) damage is likely to have similar but diminished effect as that expected from Tension-Compression fatigue due to the fact that essentially only a single compression cycle is experienced.

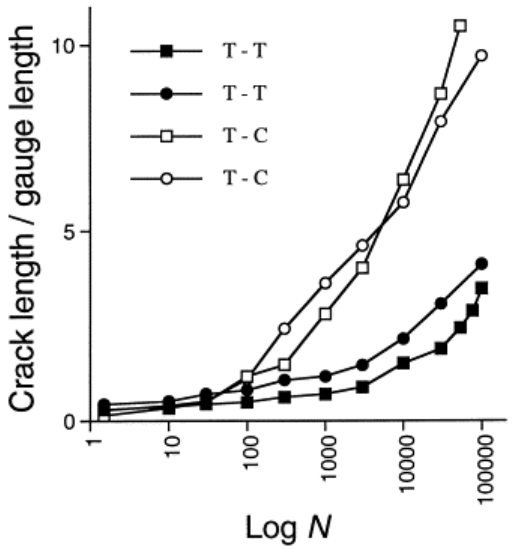

Figure 2.19. Tension-Tension vs Tension-Compression fatigue[48]

In a study of the effects of T-T and T-C fatigue, Gamstedt et al. [48] found significantly higher crack growth rates in the T-C trials. This can be seen in Figure 2.19. Analysis found

this to be from increased matrix debond rates from the fibres, increasing the initiation and density of intralaminar cracks within the composite.

3. SPECIMEN DESIGN

3.1 Materials

The composite materials used in this study were manufactured from a unidirectional IM7/5320-1 (190gsm) carbon fibre/epoxy resin pre-preg by National Institute for Aviation Research at Wichita State University. IM7 is a continuous fibre, high performance aerospace grade carbon fibre made from PAN[49]. 5320-1 is an epoxy resin designed for aerospace primary structure parts which can be used in an out-of-autoclave low temperature cure or vacuum-bag-only manufacturing capacity [50]. The cured composite is approximately 59.9% fibre by volume[50].

A single composite lamina of IM7/5320-1 has the following properties at 75°F:

Table 3.1. Material Properties [50]

Property	**Value [GPa]**
E_{11}	157.2
E_{22}	9.4
G_{12}	5.5

3.2 Manufacture

Using the IM7/5320-1 material system, three composite panels were manufactured with a thickness of 12 plys. Two panels were made with a $[\pm 45_3]_s$ layup (Specimen type 1) and the third panel (Specimen type 2) had a $[\pm 45_2/90_2]_s$ layup. The second layup is the same layup as layup 1 with the middle four plies exchanged with 90° plys (i.e. perpendicular to the loading direction). Both layup types were designed to be both balanced and symmetric as per Chapter 2.1.3. The layup design is shown in Figure 3.1.

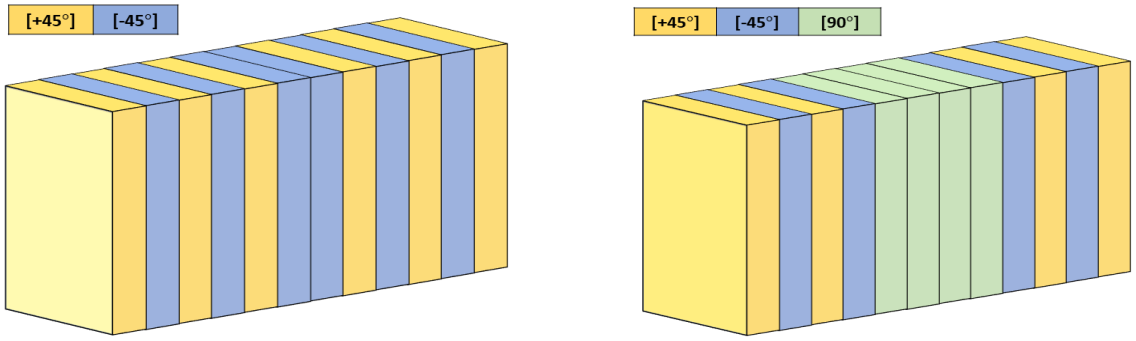

(a) $[\pm 45_3]_s$ (b) $[\pm 45_2/90_2]_s$

Figure 3.1. Composite layup design

The panels were cured as per the manufacturer's process[50], which involves heating the vacuum bagged panels to three temperatures and holding at each temperature for 2 hours. This process can be seen in Figure 3.2.

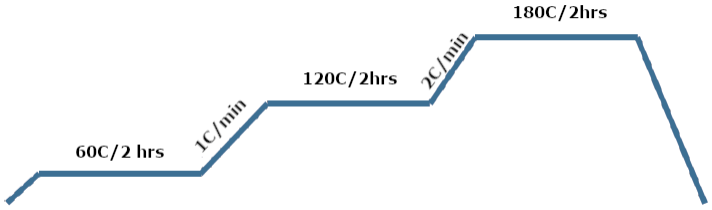

Figure 3.2. Manufacturer's cure cycle [50]

Each panel was then water-jet cut into 12 individual specimens as seen in Figure 3.3, giving a total of 36 specimens.

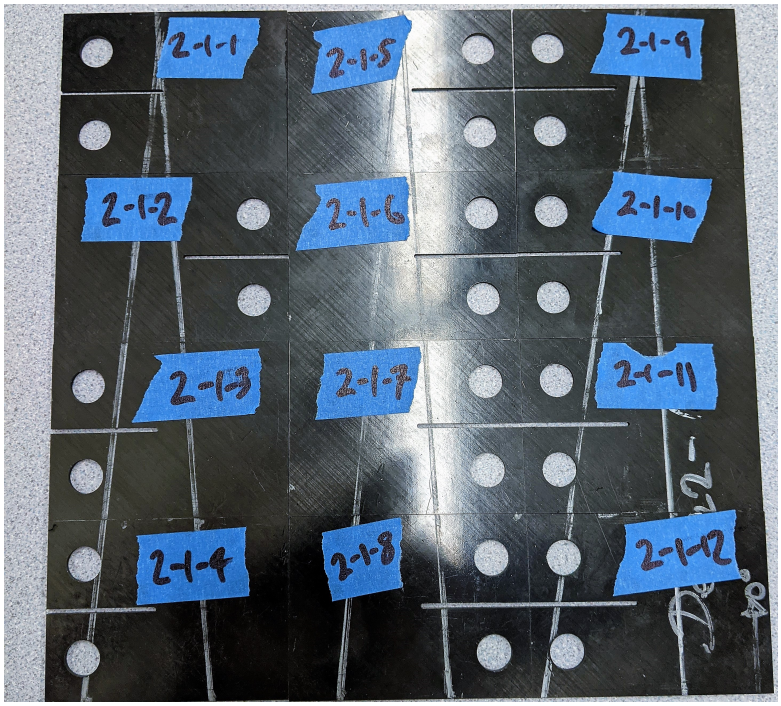

Figure 3.3. Panel-3 post manufacture and water-jet cutting

3.3 Specimen Design

The specimens cut from the manufactured panels were of Compact Tension (CT) design to relate to similar work [24, 31, 34, 43] to enable comparison. Further as discussed in Section 2.2.4, there has been much discussion as to whether the similitude parameters primarily based on the strain energy release rate, G, and its derivatives, typically experimentally determined from delamination growth in DCB tests, will work in more complex stress states [23, 27] that have more than one damage type.

The specimens were designed in order to achieve adherence with technical standard ASTM E1820 [51] where able, and to maximise the quantity of specimens generated from each panel. The final as manufactured design can be seen in Figure 3.4. The layup axis directions are labelled in the top right of the figure.

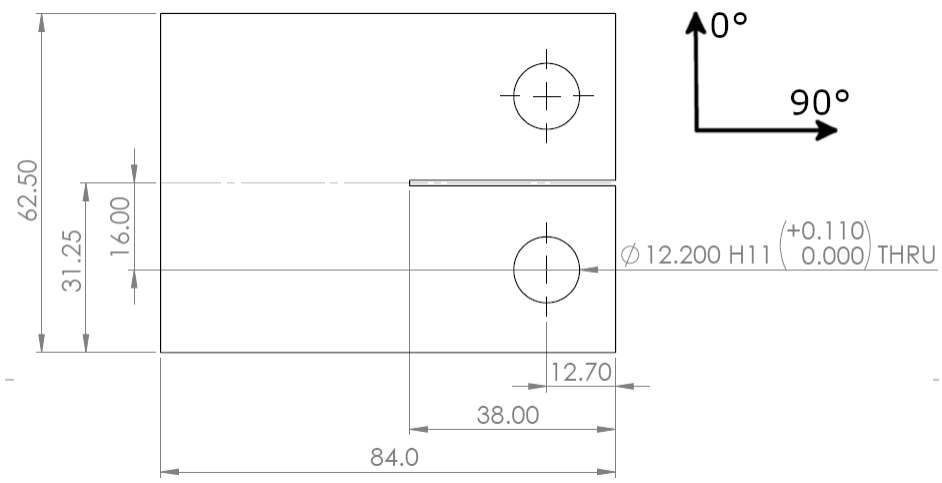

Figure 3.4. Specimen design [mm]

The hole-shaft clearance as seen in the above figure is classified as a H-11 loose-fit (the largest tolerance for hole-shafts) per ISO-286 [52] however the tolerance should be relaxed further or a slightly larger hole size specified in future work to reduce rotational friction of the specimen when tested on clevis grip pins.

The mean specimen dimension as per manufacture is:

Table 3.2. As Manufactured Specimen Dimensions

Dimension	**Mean [mm]**
Height	62.517
Width	84.049
Thickness	2.141

The following nomenclature is used to identify each specimen, where $X = 1 \rightarrow 12$:

Table 3.3. Specimen Nomenclature

Specimen Name	Layup	Panel
1-1-X	$[\pm 45_3]_s$	Panel 1
1-2-X	$[\pm 45_3]_s$	Panel 2
2-1-X	$[\pm 45_2/90_2]_s$	Panel 3

3.4 Notch Design

The notch thickness was not specified in the design drawing supplied to the the manufacturer. Rather it was requested that manufacturer use the minimum water-jet size available. The notch length was 45% of the overall length of the specimen which had proven ability to initiate crack growth as per [24, 31, 34]. The mean notch width as manufactured was 1.608mm, measured with a 5x optical microscope.

As the notch was cut by water-jet it has a rounded notch tip. An image of a sample notch tip (Specimen 1-2-10) can be seen in Figure 3.5.

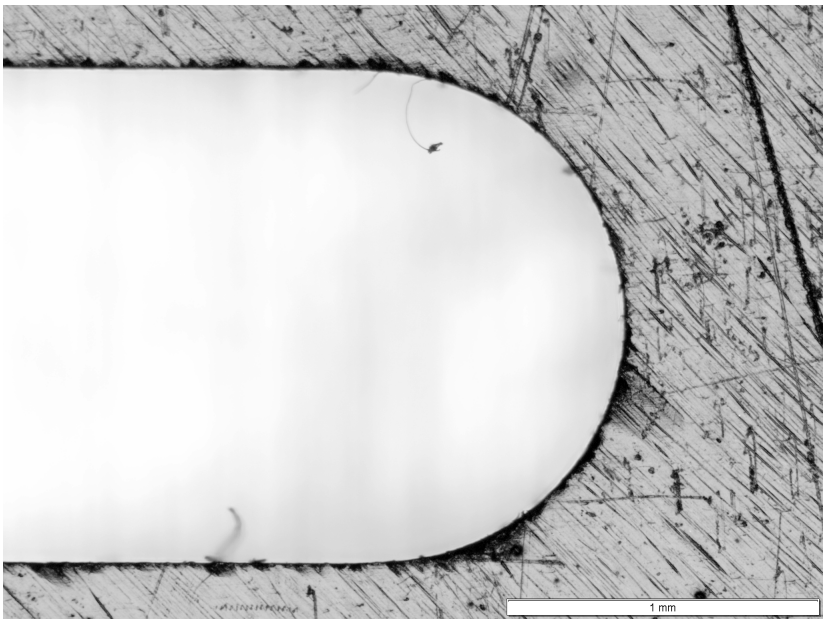

Figure 3.5. Notch design using 5x microscopy

Due to the large notch length to specimen length ratio of 45%, there was no difficulty in initiating crack growth in the specimens. In fact most specimens generated cracks on the order of millimetres within 1000 cycles.

3.5 Manufacturing Defects

Whilst the quality of the specimens manufactured was high overall, a large amount of physical surface damage in the form of surface grazing and scratches was visible in images and under the microscope which made the photographic capture of damage growth harder at times. To manage this, lighting, particularly lighting angle, was of high importance in order to highlight the growing damage and not the surface damage created during manufacture. This damage can be seen in the macro-scale in Figure 3.6a and in the micro-scale in Figure 3.6b and was present on all specimens tested. Note that 3.6a is an inverted image to make defects easier to see.

A large amount of fibre misalignment on the surface plys was also visible when viewed under magnification. The majority of misaligned fibres were within a few degrees of the majority however most outer plys had outlier fibres that were 45-90° misaligned from the global average. The majority of dark lines visible in Figure 3.6a running in the vertical direction are single misaligned fibres. A misaligned 90° fibre is visible in the top right of Figure 3.6b. The misaligned fibres are likely caused by inadvertent human action during the layup process.

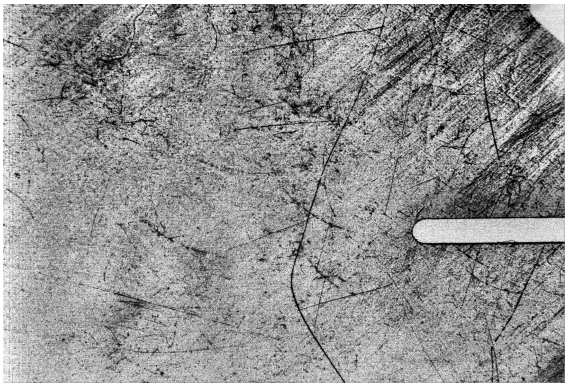

(a) Macro-scale surface Damage

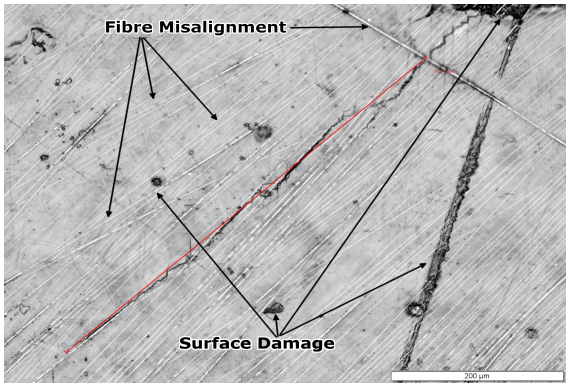

(b) Micro-scale surface damage and fibre misalignment

Figure 3.6. Visible specimen surface defects

4. EXPERIMENTAL SETUP

This section contains information pertinent to the setup, conduct and analysis of the mechanical monotonic and fatigue tests.

4.1 Testing Equipment Configuration

All testing was carried out within the ACME^2 laboratory at Purdue University West Lafayette, located within The Neil Armstrong Hall of Engineering.

Monotonic and fatigue testing was undertaken using an MTS hydraulic test machine paired with a clevis-grip attachment. The full configuration can can be found in Table 4.1.

Table 4.1. Fatigue Test Equipment

Name	Model	Rating (kN)
Load Frame	MTS 632.41B-01	50
Force transducer	MTS 661.20E-03	100
Clevis Grips	MTS 640.20B-01	-
Force Alignment Cell	MTS 609.10	100
Hydraulic Actuator	MTS 244.12	25

4.2 Image Capture and Crack Growth Measurement

This section contains information pertinent to the measurement of crack growth in the CFRP specimens.

4.2.1 Camera Setup and Image Acquisition

An Allied Vision Manta G-201B industrial, ethernet controlled, camera was set up to monitor crack growth. The camera captures a monochrome 2-megapixel image in a number of formats, including the mono12 format which was the highest definition image available and captures 12 bits per pixel[53]. The camera was used with a 5x magnification lens and was mounted to the load frame, adjacent to the specimen and MTS load frame. The camera uses the GigE Vision standard to transmit and receive data, and was able to be controlled

with a variety of software applications including MATLAB. Figure 4.1 shows the camera setup.

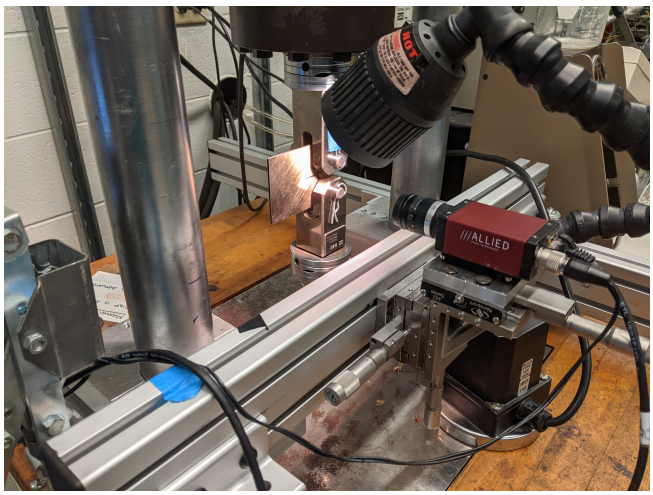

Figure 4.1. Camera setup

The 'Vimba' software that is provided by the camera OEM was determined to be not suitable for this application as it does not allow for automatic image acquisition nor does it save captured images easily. The application was also quite unreliable with the data stream being lost or frozen often.

For this reason, the camera was controlled using the MATLAB Image Acquisition toolbox and the associated "Image Acquisition Toolbox Support Package for GigE Vision Hardware" MATLAB Add-on package using details from the OEM [54], MATLAB user guides and information available online. This was initially also quite unreliable due to the same data stream loss and frozen image issues, however after a significant amount of troubleshooting a reliable camera initialisation script was written. The following components were found to be required to have a reliable camera acquisition setup:

- Network Card Settings - It is critical to verify the settings of the installed network card the camera is attached to in accordance with the instructions found in the Manta Technical Manual [55]. Reliable results will not be achieved without this step.

- Packet Size and Delay - Related to Network card settings but is required to be specified in the MATLAB script. A packet size of 9000 and a Packet Delay of 2290 was used after troubleshooting.
- Exposure Time - A small exposure time should be used to increase the frame-rate, reduce lag and stop blurry/frozen images forming over time. A brighter image can be achieved with lighting to mitigate.
- Clearing data - After each photo, the camera stream should be stopped and the data flushed from its memory to stop the data stream corrupting over time.

4.2.2 Image Processing and Crack Measurement

A custom Graphics User Interface (GUI) was written in MATLAB to show the previously captured images and compute the length of the lead crack based on basic trigonometry. The script scans a folder for images, correctly orders them and performs a series of image corrections and enhancements to better allow crack identification. The image shown in Figure 4.2 shows the GUI. The images were typically displayed in inverted colour to enable higher contrast of the cracks growing in the specimen versus the normal CFRP surface. This worked very well and even small changes in crack size can be seen.

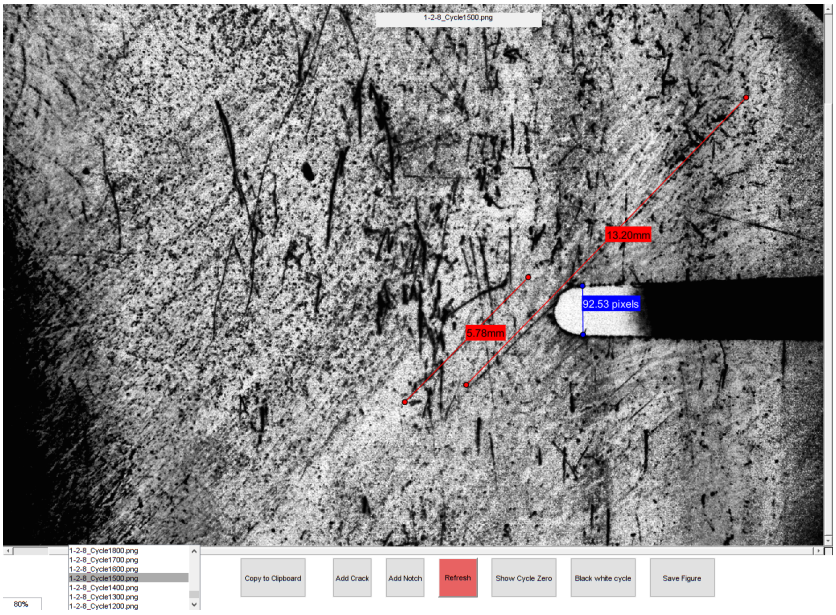

Figure 4.2. Custom MATLAB GUI

Damage was able to be measured off images by selecting the 'Add Crack' button allowing for a [red] line to be drawn over the damage. Using trigonometry, the length of the line is calculated in pixels. The calculated pixel length is transformed into a millimetre distance value by adding an additional line across the width of the notch, which has a known mean value from previous microscopy.

The error associated with crack measurements is 4 pixels per side of the damage, multiplied by the mean notch width in millimetres (1.608mm), divided by average notch width in pixels (80). The associated error in each measured length is therefore 0.16mm. Multiple microscopy events validate this crack length error.

As multiple cracks grew in the composite outer-ply (a minimum of two for each specimen), the lead crack was chosen by finding the longest crack at failure, and using the images captured to review the cracks growth from initiation.

4.3 Specimen Out-of-Plane Deflection

Prior to any testing, alignment of the specimens was carried out in accordance with ASTM Standard [56, 57]. Regardless, after multiple trial monotonic and fatigue tests it

became apparent that the CT specimens of both layup orientations were susceptible to out-of-plane deflection/bending under the higher applied loads due to being relatively thin. Numerous actions were taken to try prevent this from occurring including multiple MTS re-alignments using the force alignment cell, however the deflection could only be reduced and not eliminated all-together. Other work in the area has seen similar issues using CFRP CT specimens [58].

In mitigation, an aluminium backing plate that was pushed up against the back face of the specimen to stop the deflection of the specimen under load, see Figure 4.3.

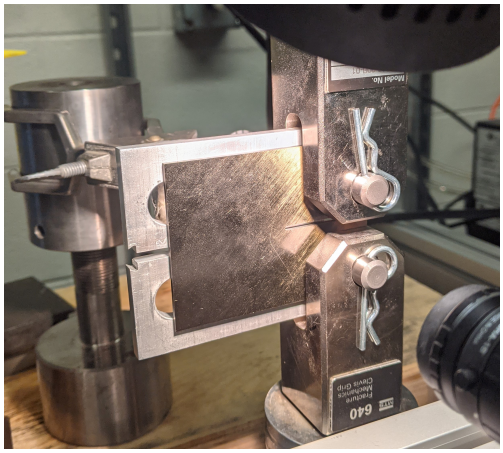

Figure 4.3. Setup to reduce out-of-plane bending

This worked well but created a different data set due to the increased strength of specimens loaded in this configuration as opposed to those without, by as much as 1300N in ultimate strength. The difference in material behaviour with out-of-plane deflection limited are shown in monotonic test results for both cases, seen in Figure 4.4. Whilst the behavioural differences in both cases is large, it was considered a requirement to limit out-of-plane deflection in order to achieve more consistent fatigue compliance results and ensure clear crack growth images. In all further chapters, all data is for the deflection limited case.

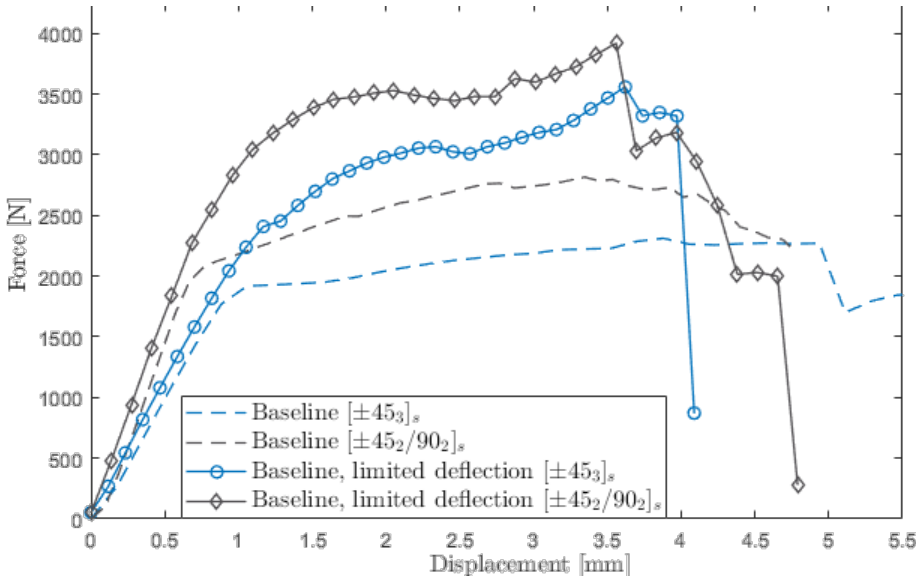

Figure 4.4. Monotonic tension test results for the original and limited out-of-plane deflection cases

The resultant ultimate and yield loads for each layup and deflection configuration have been outputted in Table 4.2. Monotonic testing setup and discussion is found in Chapter 7.

Table 4.2. Baseline Monotonic Tension Results

Specimen Type	Ultimate Load [N]	Yield Load [N]
$[\pm 45_3]_s$	2330	1886
$[\pm 45_3]_s$ Bending Limited	3612	2429
$[\pm 45_2/90_2]_s$	2834	2074
$[\pm 45_2/90_2]_s$ Bending Limited	3960	3027

5. IMPACT DAMAGE SPECIMENS

5.1 Design

Impact damage is very common in aerospace composite structure due to inadvertent maintenance actions, or runway debris [35, 37]. The of damage tolerance of impact damage in CFRP materials is therefore of interest.

To create this damage in a consistent manner on the CT specimens, a Vikers Micro-Hardness tester/micro-indenter was used to apply a $50kg \cdot f$ point load to the outer plys at a distance of 5mm from the notch on both faces of the $[\pm 45_3]_s$ and $[\pm 45_2/90_2]_s$ CT specimens. This load was applied and sustained for 10 seconds in each case. The impact specimen design can be seen in Figure 5.1. The force applied to the specimens was determined through test as seen in the next sub-section.

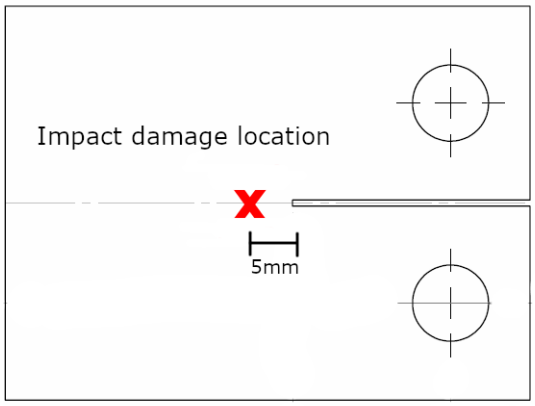

Figure 5.1. Impact specimen design

The indent site was chosen as 5mm from the notch tip in order to be within the highest stress region and to hopefully interact with the lead crack which typically evolved from the notch tip in the plus or minus 45° direction.

5.2 Process Overview

In order to determine the appropriate force to use on the micro-indenter a test was performed on a spare section of laminate of the same type. Four different loads of 10, 20,

30 and 50 $kg \cdot f$ were applied at intervals across the test piece. The resultant damage from each was then assessed under microscope from the surface (Section 5.3) and by a sub-surface cutaway (Section 5.4). At the surface, each had a distinctive indent pattern from the micro-indenter in the form of a cross-shape as seen in Figure 5.2.

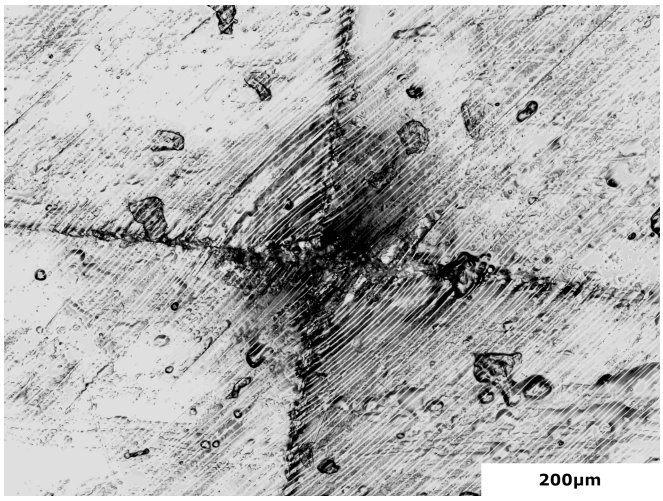

Figure 5.2. $50kg \cdot f$ quasi-static indent (see dimensions in Table 5.1)

5.3 Surface Damage

The surface damage was able to be quantified under 10x and 20x microscope for the lateral dimensions and vertical dimensions respectively (using a z-stack microscopy image). The damage on the surface was averaged to get a mean diameter. These visible surface dimensions are quantified in Table 5.1. A review of Figure 5.2 shows consistent surface

Table 5.1. Indent Surface Damage Size

Indent Force $[kg \cdot f]$	**Diameter** $[\mu m]$	**Depth of damage [% ply thickness]**
50	1041	26.5
30	816	21.2
20	685	18.6
10	481	10.6

fibre breakage events across the entire length of the cross-shape profile created by the micro-indenter. Fibres between the ridges of the indenter appear unaffected. There is also a

gradual decrease in laminate cross-section along each indent ridge line, coalescing in the centre where a large divert in the matrix is present. This damage profile is similar across all indent loadings examined with the difference being the relative severity which increases with increasing loads as expected.

5.4 Sub-Surface Damage

To further examine the damage a cross-section of the laminate was cut and cast into epoxy resin allowing for polishing of the laminate cross-section up to the damage location to reveal the actual sub-surface damage that had accrued within the layup. As all four indent damages were put on the same cross section of laminate and therefore the process of incrementally polishing and reviewing under optical microscope was required. Unfortunately only three of the four cross sections were found using this process (10, 30, 50 $kg \cdot f$). The cross sections of the damages are examined below in Table 5.2. The examination of each

Table 5.2. Indent Sub-Surface Damage Size

Indent Force [kg · f]	**Delamination length [μm]**	**Depth of damage [μm], [% ply thickness]**
50	602.1	178.4 [100]
30	548.2	177.1 [99.1]
10	0	109.2 [61.2]

set of impact damage showed relatively consistent damage events; with a large cross-section of fibre breakage in the immediate vicinity of the centre of the indent (shown by the void or black area underneath the impact area), a region of intralaminar cracking at the base of the fibre breakages and, for the larger impacts, a region of delamination devolving from the intralaminar crack at the ply 1 and 2 boundary.

Images of the sub-surface damage are shown in Figures 5.3, 5.4 and 5.5. Each image is the the approximate centre cross-section of the indent as determined by the cross-sectional diameter of the impact area in comparison to that determined from the surface.

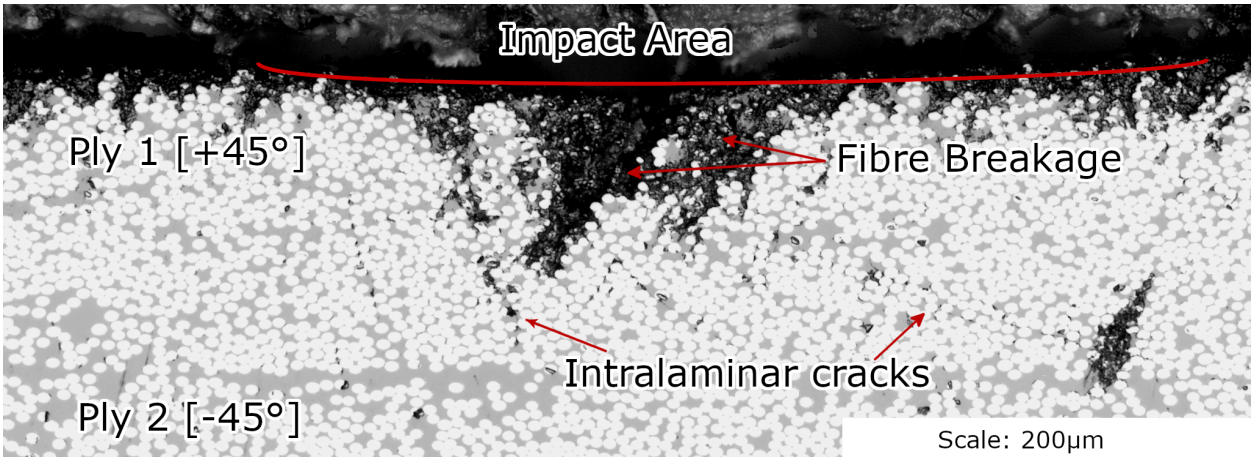

Figure 5.3. $10kg \cdot f$ indent sub-surface damage [20x stitched]

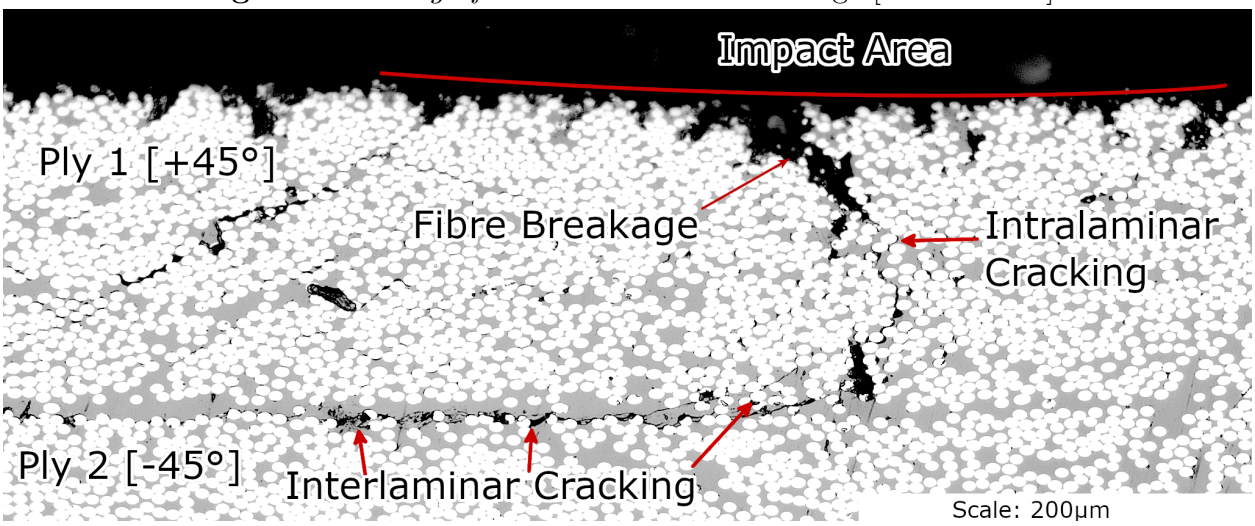

Figure 5.4. $30kg \cdot f$ indent sub-surface damage [20x stitched]

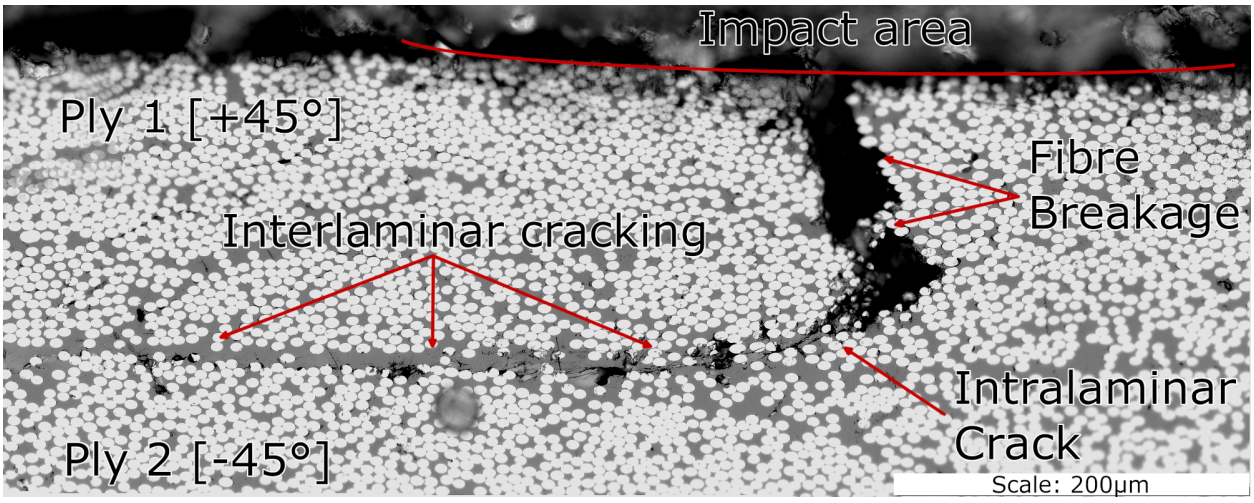

Figure 5.5. $50kg \cdot f$ indent sub-surface damage [20x stitched]

Further, it was seen that the delaminations found underneath the impact area had sharp crack tips as seen in Figure 5.6. The image is taken at 50x magnification under an optical microscope at the extreme end of the delamination in Figure 5.4. The image shows interlaminar crack is travelling as a series of disbonds along fibre circumferences as expected from shear/compression based failure modes [59, 41] as discussed earlier.

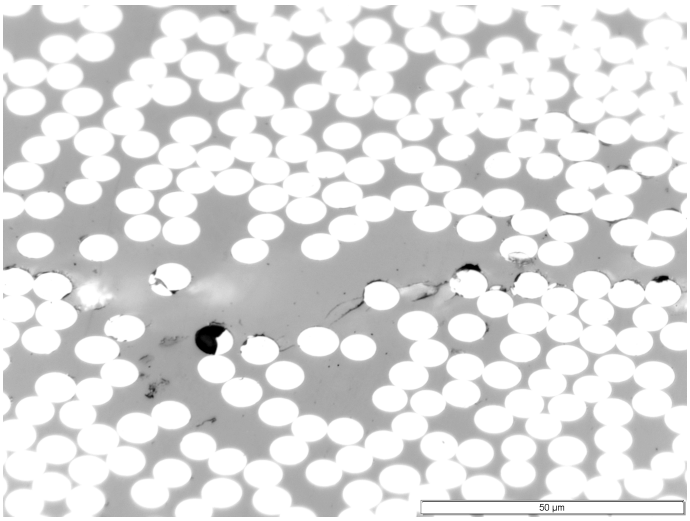

Figure 5.6. Interlaminar delamination sharp crack tip

5.5 Comparison to Impact Damage

The damage imparted from the Vikers Micro-Hardness tester/micro-indenter showed significant correlation to that expected from a true-impact on a carbon fibre composite layup as seen in other studies. Impact damage has been shown to generally have fibre-breakages, matrix compression damage and shear driven delaminations [36, 37, 27]. The same damage events are seen in Figures 5.5, 5.4 and 5.3, with a large section of fibres breakages in the centre of the indent location. The section fibre breakage is the result of the shear loads applied directly to the ply which has almost no stiffness in the out-of-plane direction as it is perpendicular to the fibre layup direction. The shear load therefore causes failure of the localised band of fibres which progresses to intralaminar matrix failure towards the bottom of the ply where the transmitted energy is lower. This intralaminar matrix cracking evolves into a interlaminar delamination at the ply-ply interface as seen in Figure 5.7a. This is

exactly as expected from Section 2.3.3 where it was seen in literature that interlaminar delaminations present after impact were always formed from intralaminar matrix cracking at the ply boundary due to the reduced energy cost of travelling unimpeded through the matrix ply interface as opposed to continually propagating through a fibre-matrix layup [37].

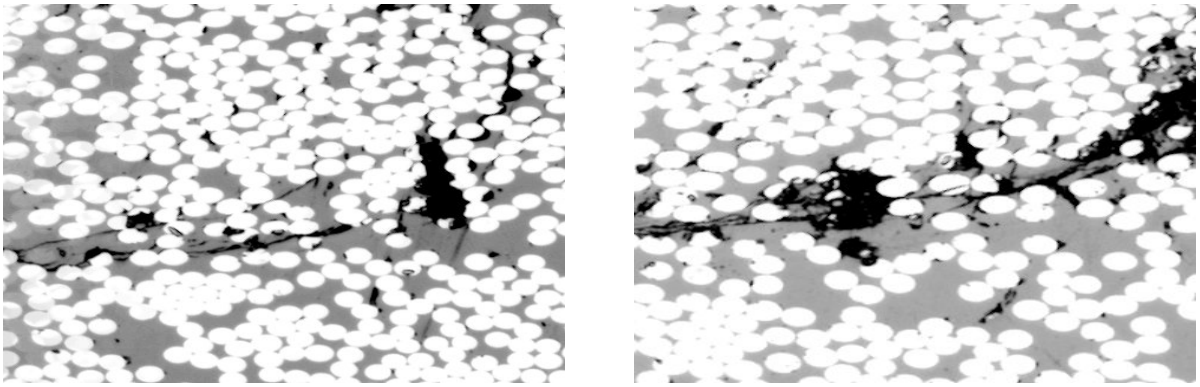

(a) $30kg \cdot f$ (b) $50kg \cdot f$

Figure 5.7. Evolution of a intralaminar crack into an interlaminar delamination

Studies such as [37, 60, 61] have also shown that delamination size from impact has a linear relationship with imparted energy. Other studies [62] show that delamination area was exponential up until certain peak value at which time increased energy imparted from impact showed no increase in size. Figure 5.8 shows the surface and sub-surface delamination sizes in graphical form. It can be seen that the surface damage forms a largely linear relationship between imparted energy and size.

Sub-surface delamination size is harder to assess as there is only two non-zero damage lengths available, however a linear relationship passing through the origin seems incorrect. Work by Cartié et. al [61] showed a linear relationship of delamination area after a region of no delamination growth at smaller impact energies, which may align better with the data from this study.

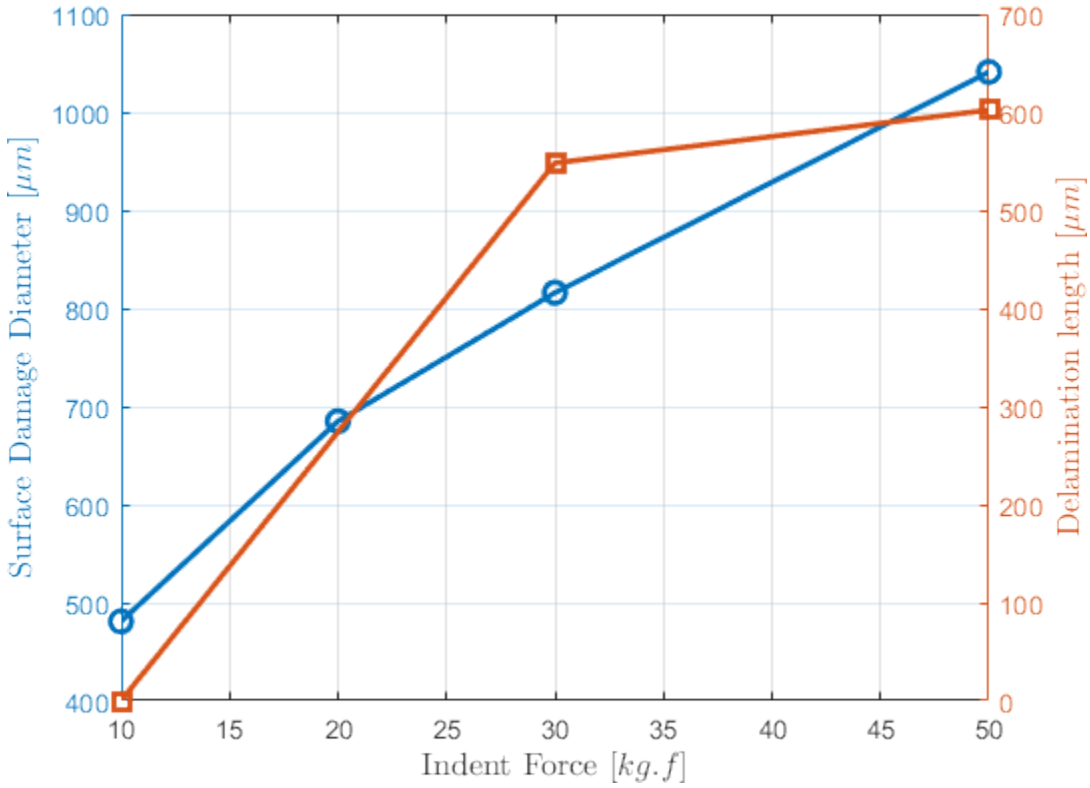

Figure 5.8. Impact damage size comparison

6. COMPRESSION DAMAGE SPECIMEN

6.1 Design

Fatigue compression loading of CFRP composite laminates is typically very significant due to the reduced stiffness when the aligned fibres are not in tension. Continuous compression-compression fatigue loading or tension-compression loading provide multiple opportunities to use this inherent weakness to initiate and progress damage within the layup. However damage produced from just a single, unexpected compression cycle may cause damage that alters the tension-tension fatigue properties of the layup. This chapter will look at this scenario.

Initial aims within this work were to initiate kink-bands within the composite (Section 2.3.4) however it became apparent early on that this would be difficult to achieve in non-axially aligned fibres. Almost all research into kink band formation has been achieved in fibres aligned with the loading direction [42, 40, 45, 46, 63].

Instead the aim was create compression damage of any form, but notionally buckling, through a single compression load.

6.2 Process Overview

Each sample to undergo damage via compression was monotonically loaded in compression under displacement control at a rate of $0.05mm/min$. The test continued until compression damage was visible on both of the outer plys. This typically occurred at what appears to be the compressive proportional limit in the form of outer ply buckling, however as will be shown in Section 6.4, significant subsurface damage was also present. Data was recorded by the MTS Test Suite at 512 Hz.

Figure 6.1 shows the results of four of the monotonic compression tests. Similar to the monotonic tension test, the $[\pm 45_3]_s$ layup had a more compliant response to loading than that of the $[\pm 45_2/90_2]_s$ layup. Both layups were only subjected to completely elastic deformation, and returned to its original size and shape on unloading.

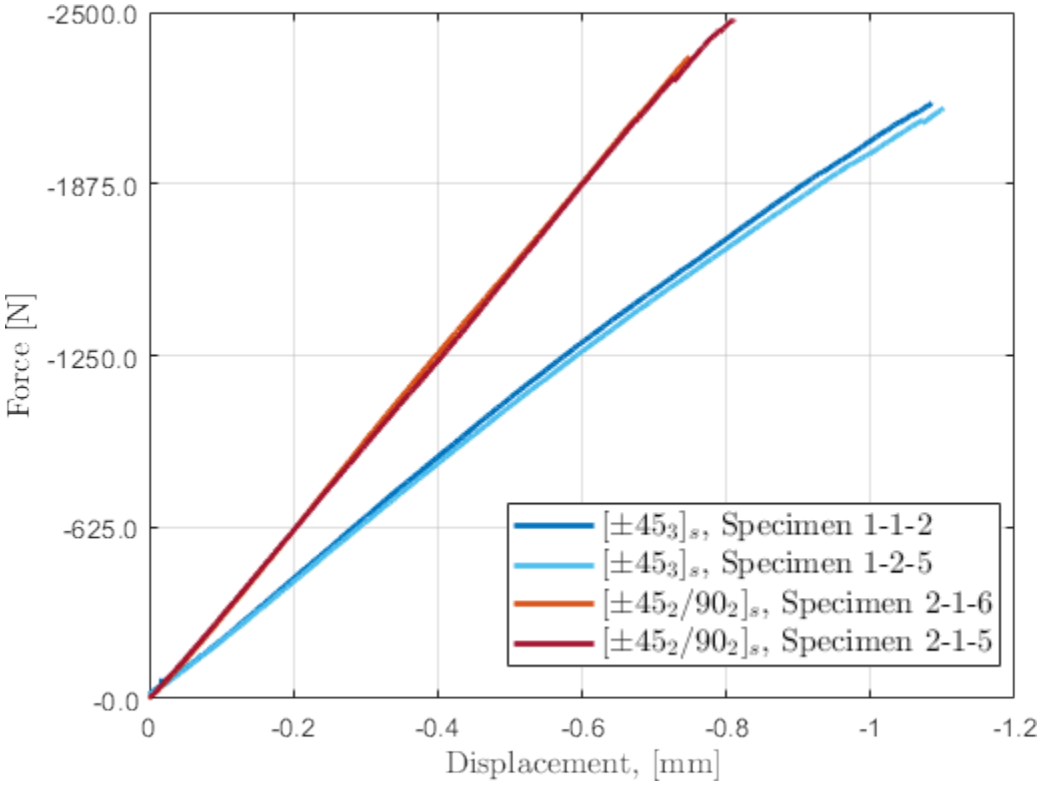

Figure 6.1. Compression monotonic tests

Figure 6.3 shows a close-up of the end of each test, that is a close up view of the end of Figure 6.1. Visible load drops, representing the creation of damage, were seen on each specimen. Many other studies, as discussed in Section 2.3.4, show a large load drop after initiation of damage followed by growth of kink bands. These studies are typically use specimens with unidirectional, load aligned fibres under uni-axial compression loading. The CT specimens used in this work have a much more complex fibre orientation and loading condition. As such the decision was made to not continue with loading after damage was visibly observed. Though as will be seen in Section 6.4 sub-surface kink band formation did occur.

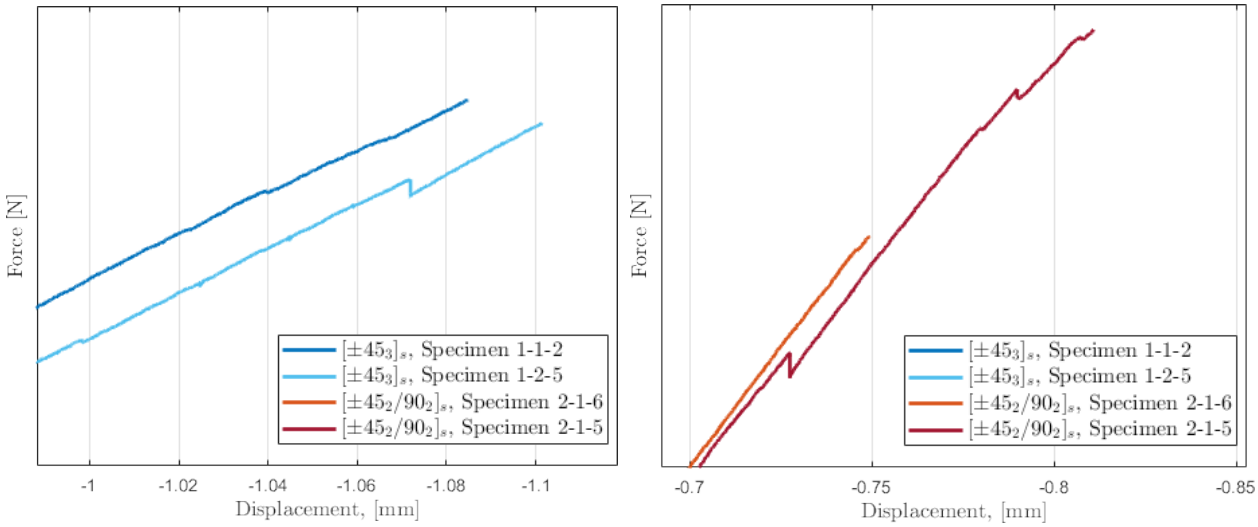

(a) $[\pm 45_3]_s$ (b) $[\pm 45_2/90_2]_s$

Figure 6.2. Compression monotonic test - close up of Figure 6.1

6.3 Surface Damage

Figure 6.3 shows the damage seen on the surface of each layup type after compression loading and before fatigue loading. The damage shown in the figure is consistent with damage seen in all other compression damage specimens created. Both of the images show surface damage in the form of outer ply buckling in the out-of-plane direction, with a series of intralaminar cracks leading to and from the buckles.

The buckling was approximately $500\mu m$ in all cases, but it occurred in either two smaller areas of buckling (Figure 6.3a), or one large buckle (Figure 6.3b) with the same relative frequency.

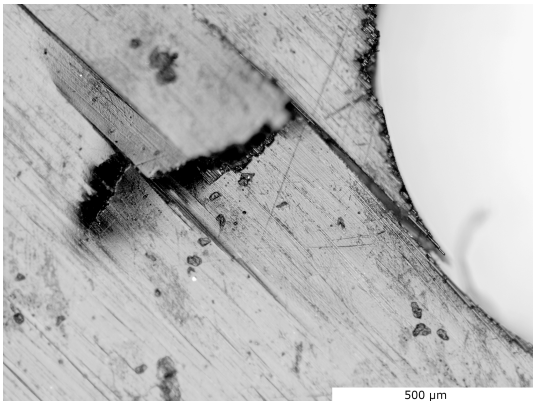

(a) $[\pm 45_3]_s$

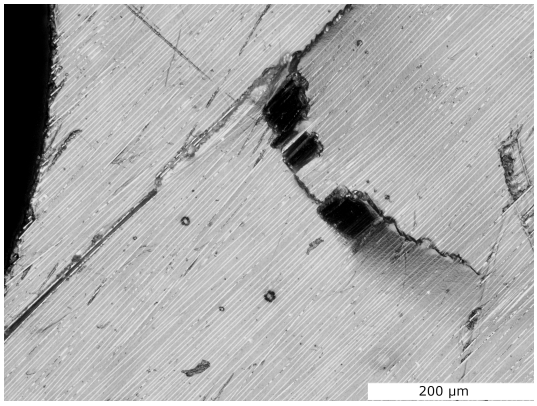

(b) $[\pm 45_2/90_2]_s$

Figure 6.3. Compression damage close up

The area underneath the buckle shows fibres aligned with fibres visible on the surface, which means the full outer-ply did not buckle, only a proportion of it did.

6.4 Sub-Surface Damage

The laminate was sectioned at a 45° angle at Section-A as per Figure 6.4 in order to assess the damage created from the compressive single load. Note however that the sectioning occurred after fatigue loading which makes the linking of compression loading to damage slightly harder however damage can be correlated based on whether it is seen in undamaged, fatigue loaded, specimens.

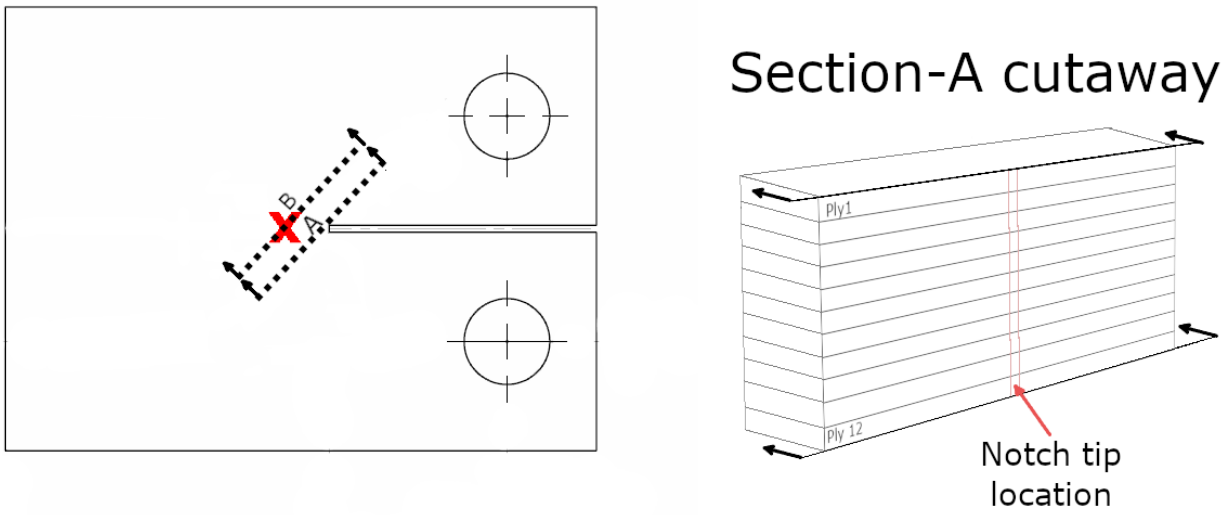

Figure 6.4. Specimen section and microscopy locations

All fatigue loaded compression damaged specimens were examined in the above manner however only two examples are examined in depth in this section (one of each layup type). The damage in these figures are representative of the damage seen in all examined layups of their layup configuration. Figure 6.5 shows the damage seen in Specimen 1-1-2, a $[\pm 45_3]_s$ laminate, after compression loading and 972.5 thousand cycles of fatigue loading at R=0.5.Figure 6.6 shows the damage seen in Specimen 2-1-6, a $[\pm 45_2/90_2]_s$ laminate, after compression loading and 954 thousand cycles of fatigue loading at R=0.5.

There is some discussion to be had with respect to the nomenclature of kink bands. In Section 2.3.4 it was inferred that there was a difference between buckling and kink bands however this is not necessarily the case. Kink band as used in this chapter refers to localised micro-buckling of fibres within a layup. Whether this micro-buckling occurs in-plane[44, 45, 46, 43, 47] or out-of-plane[64, 65, 66, 32, 67] is unimportant.

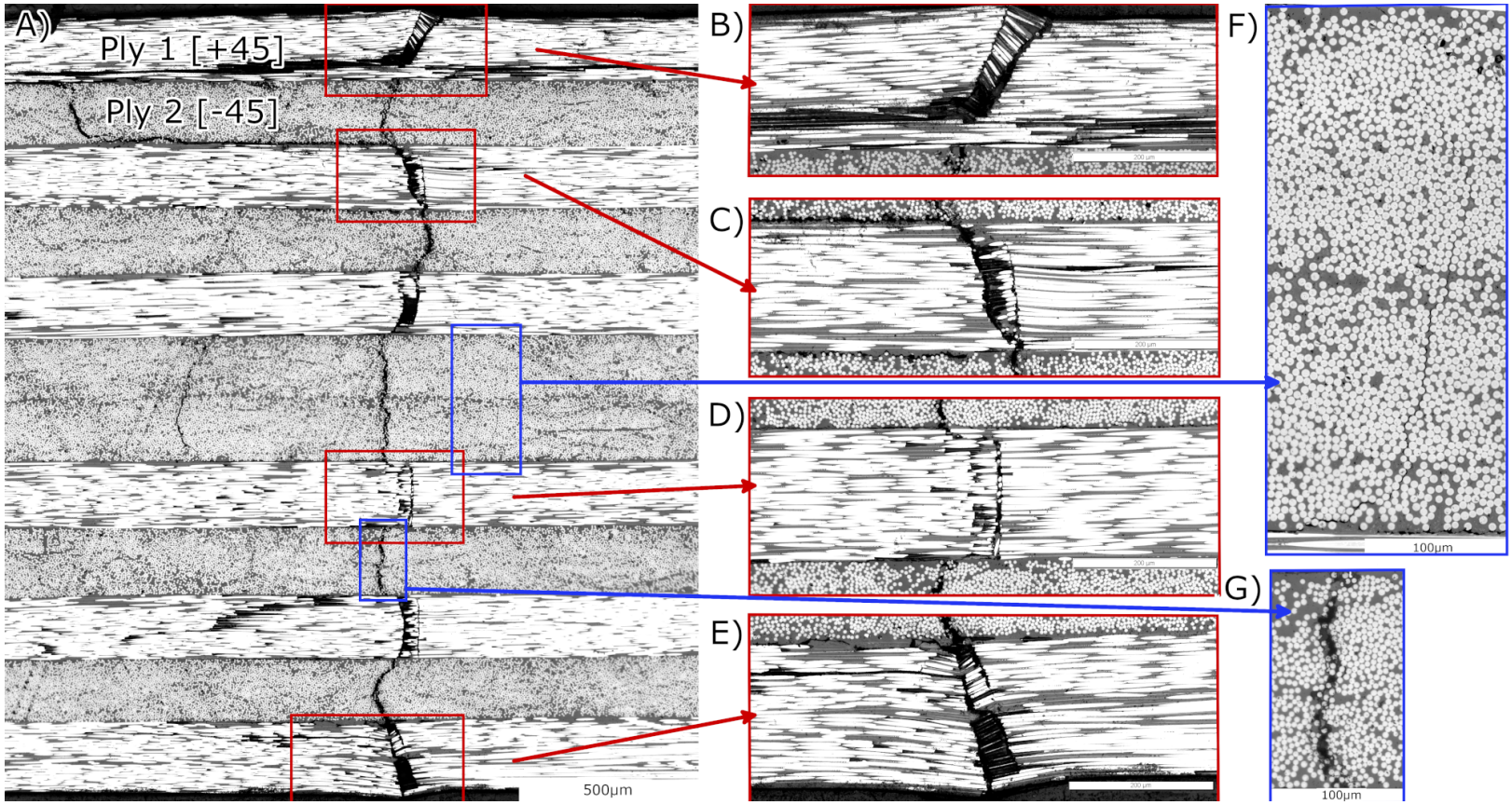

Figure 6.5. Compression damage in a $[\pm 45_3]_s$ Layup - Specimen 1-1-2. A) Image of the full thickness of the layup at Section-A (Figure 9.1). Taken after fatigue loading for 972.5 thousand cycles. B) Close-up of Ply 1 partial ply thickness kink-band formation, leading into a intralaminar crack. C) Close-up of Ply 3 kink band and/or significant fibre-fracture. D) Close-up of intralaminar crack in Ply 7 leading to full thickness fibre-fracture in Ply 8. E) Close-up of kink-band formation in Ply 12. F) Intralaminar crack growth in Plys 6 and 7, leading to delamination in Ply 7-8 interface. G) Significant width intralaminar cracking in Ply 9, representative of the significant cracking seen in all $[-45°]$ plys.

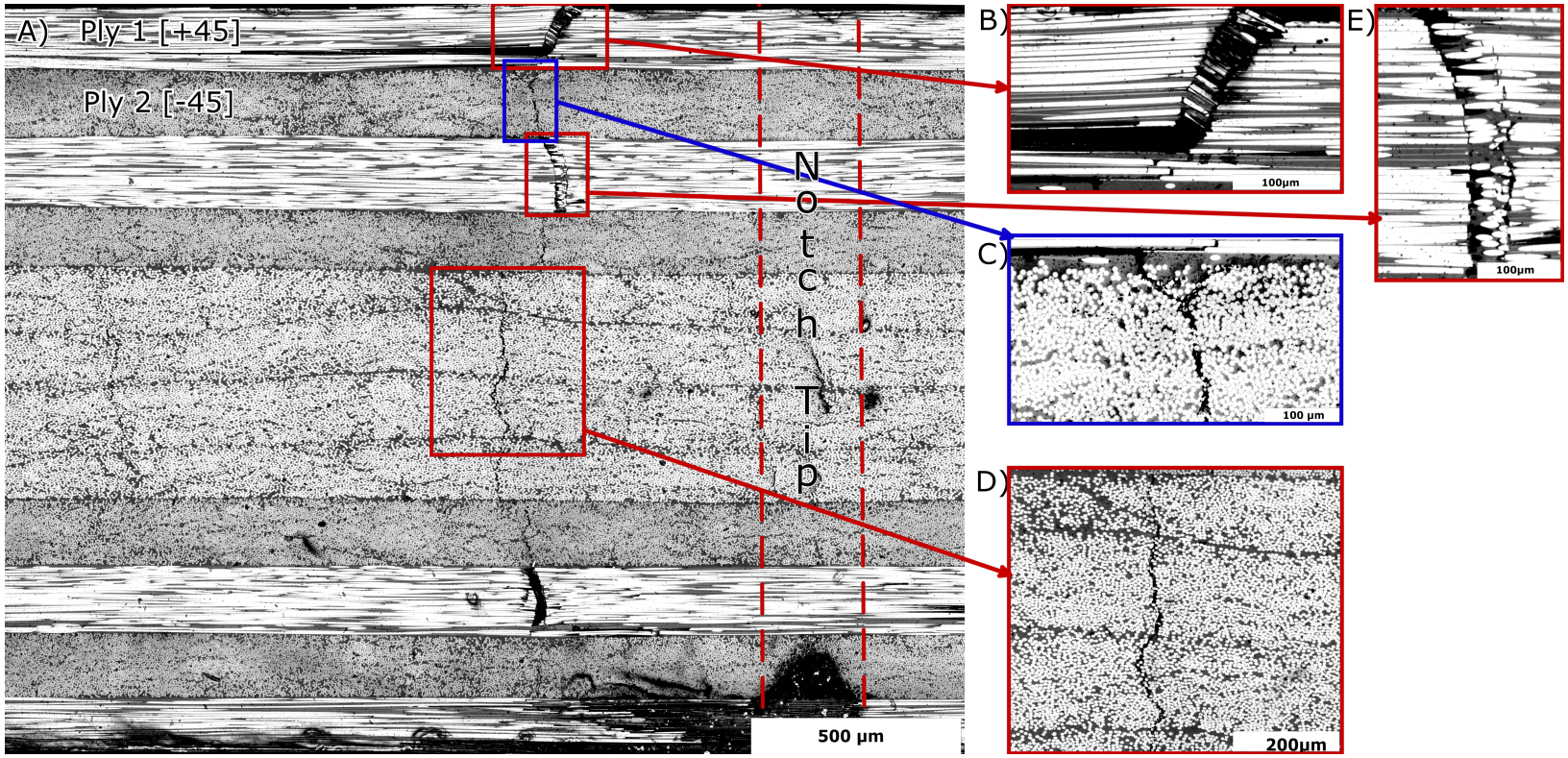

Figure 6.6. Compression damage of a $[\pm 45_2/90_2]_s$ Layup - Specimen 2-1-6. A) Image of the full thickness of the layup at Section-A (Figure 9.1). Taken after fatigue loading for 954 thousand cycles. B) Close-up of a partial ply thickness kink band formation, leading to a intralaminar crack. C) Close up image of two the bifurcation of a single intralaminar crack into two distinct intralaminar cracks at the boundary of Ply 1 and 2. D) Curvature seen in the central 90° plys (Ply 5-8) after compression loading. E) Close-up of Ply 3 with significant fibre-fracture.

Figure 6.5 and 6.6 were taken from cut and polished specimens after a single compression loading event and approximately 1 million cycles. Whilst all damage seen in the figures cannot therefore solely be attributed to compression loading, there is damage seen within the layup that is unique to the compression damage specimens examined which allows this with a fair degree of confidence.

For Specimen 1-1-2, Figure 6.5 A) shows the full cross-section of the $[\pm 45_3]_s$ layup. It can be seen that there is a single line of damage across the thickness of the specimen. In the outer plys (ply-1 and ply-12) kink-bands have formed for either partial or full thickness of the ply, as seen in sub-figure B) and E). Sub-Figure B) and E) clearly show a region of kinked fibres. They are severed in two places and are now collectively at an angle to the applied loading. The relevant kink angles are listed in Table 6.1. In ply-1, a kink band has formed approximately 75% of the way through the ply, devolving into intralaminar crack parallel to the fibre direction. This intralaminar crack evolves into a delamination on the underside of the ply, which is linked to ply-3 (sub-figure C) by a intralaminar crack through ply-2 which connects to a delamination on the ply 2-3 interface that leads back to the line of damage that was originally stated. At the centre of ply-3 there is a line of fibre breakage in two locations. Fibre breakage is seen in all -45° plys (sub-figure B,C,D,E). It can also be seen that ply-3 (C) has a split/intra-laminar crack leading from the fibre breakage and parallel to the ply direction (left to right in the figure).

In Specimen 2-1-6, Figure 6.6 A) shows the full cross-section of a representative $[\pm 45_2/90_2]_s$ laminate after compression loading and approximately a million cycles. It can be seen that the line of continuous damage seen in the $[\pm 45_3]_s$ specimen is not quite as pronounced. The figure also shows that a kink band is only seen in ply-1 and not ply-12, though this is just at the current cross section as buckling was visually seen on both faces of all compression specimens after loading. This is due to the fact that the current cross-section is just before the end of the notch as evidenced by the dark patch of acrylic from specimen mounting in the lower right of the image. A different cross-section slightly further into the laminate would have shown the kink bands on both outer plys. The kink band seen in sub-figure B) is similar to that from the $[\pm 45_2/90_2]_s$ laminate in that a clear line of severed

fibres is visible at an angle to the rest. This kink-band leads into a splitting of the ply or intralaminar crack leading to the left.

Fibre breakage events are again seen in all -45° plys (B,E), whilst intralaminar cracks are seen in the +45° and 90° plys. In C), ply-2 shows the coalescence of two intralaminar cracks into a single crack. Sub-figure D) is of much interest. It shows that the centre 90° plys in the high stress region (as evidenced by the damage line through all plys) have significant waviness. Ply-5 in particular has been compressed significantly to approximately two-thirds of its original thickness. Ply-6 appears expanded to fill the region ply-5 is no longer filling. Ply 7 and 8 who are symmetrical to ply 5 and 6 are wavy to a lessor degree. The waviness of Ply 5 and 6 are in the same direction as the kink-band in ply-1. The 90° plys have fibres perpendicular to the loading direction by definition and thus the only stiffness comes from the matrix which appears to have deformed significantly.

Table 6.1. Kink Band Angles

Specimen Layup	**Specimen**	**Ply Number**	**Kink Band Angle [°]**
$[\pm 45_3]_s$	1-1-2	1	18.32
		12	13.80
$[\pm 45_3]_s$	1-1-12	1	7.39
		3	20.29
		12	19.27
$[\pm 45_3]_s$	1-2-5	12	10.34
$[\pm 45_2/90_2]_s$	2-1-6	12	14.39

6.5 Damage Discussion

Overall, consistent compression damage was reliably created in each specimen with little difference between each specimen of a particular layup type, with the exception of the ply compression seen in Figure 6.6 D) which was only seen in the individual sample.

As should be expected, there was also consistency between the load levels in which damage initiated in each specimen as seen by the load drops seen in the monotonic force-

displacement curves (Figure 6.2). The typical value to initiate damage was approximately -2100N for the $[\pm 45_3]_s$ specimens and -2500N for $[\pm 45_2/90_2]_s$ specimens. This point likely aligns with the matrix yield stress [46] however this cannot be verified because a destructive compressive test was not performed.

On both surfaces of each specimen, localised buckling was seen around the notch tip. Minor differences in the shape and size of this localised buckling occurred between specimens, with the amount of intralaminar cracks visible running from the buckling varying. In most cases, two cracks ran on the surface parallel to the +45° ply but as many as five formed as seen in Figure 6.3a. This is most likely from minor differences in the outer ply layup.

Inspection of the buckling at the notch appeared to be full-ply thickness from the outside but on examination of the cross-section, the damage was typically 70-80% of the ply thickness and resembled kink-band formations. Table 6.1 shows that all kink band angles ranged between 7-21°, which aligns well with that from literature which saw the angles were typically 10-35°[42].

Kyrxiakides et al. [44] in their study saw damage initiation at 1.5% compressive strain, followed by a significant load drop. Continued displacement at this lower load enabled growth in the length of kink band formations. In this case, kink band formation appears to have occurred at the compressive proportional limit (or close to) however no significant load drop was seen. Figure 6.1 shows the monotonic force-displacement curve. Small load drops occurred at the end of these curves at which time buckling was visibly seen to occur. The test was allowed to run for a small period of time after the load drops however no further load drops were seen. This is likely due to the damage tolerance of a multi-directional layup, whereas most studies on kink bands look at uni-directional ply layups [44, 45, 46, 43, 47, 64, 65, 66, 32, 67].

It has been shown in literature that fibre inter-facial disbonds that occur in compression can extend to much larger angles than those that occur under tension. Correa et al. [40] found that at a micro-mechanical level, inter-facial disbonds (debonds around the fibre circumference) were up to 60-70° of the fibre circumference under tension-tension fatigue loading, and up to 120° in tension-compression. Analysis of intralaminar crack growth in

Figures 6.5 F) and 6.6 D) shows many debond angles much larger than 60-70° present within the matrix.

The matrix serves to transmit load between adjacent fibres, and a larger fibre interfacial disbond will therefore mean higher stress concentrations are present in the remaining bonded matrix. This compression damage will likely affect damage progression though the composite.

7. MONOTONIC TENSION TESTING

7.1 Test Setup

Monotonic testing was carried out to understand the macro-mechanical performance of both layups in three damaged configurations, and to quantify material behavior so that the fatigue testing could be undertaken.

The monotonic testing was carried out in displacement control at 0.05mm per minute until failure. Failure was defined as a force drop below 50 percent of the seen ultimate load or until significant distortion of the specimen had occurred and the data was no longer representative of the material's performance. Force and displacement was recorded by MTS Test Suite at 204.8Hz and outputted as a text file for analysis in MATLAB.

Prior to testing, alignment of each specimen was carried out in accordance with ASTM Standards[56, 57].

7.2 Monotonic Tension Results

In total monotonic tension tests were carried out on a total of six specimens, representing a Baseline, Impact Damaged and Compression Damaged specimen for each layup configuration. Graphic results are shown in Figure 7.1, and the relevant material properties are listed in Table 7.1. Both specimen types have the same notional thickness.

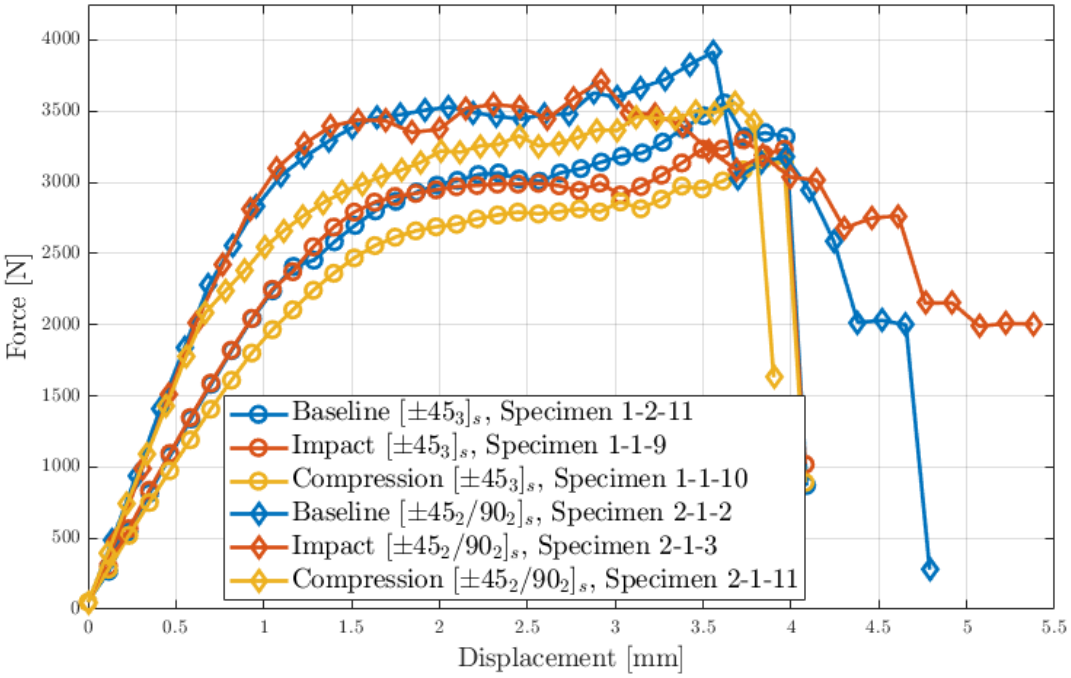

Figure 7.1. Monotonic tension force-displacement test results

As a broad overview of the results, all specimens of the $[\pm 45_2/90_2]_s$ layup exceeded the strengths of the $[\pm 45_3]_s$ layup type. In both layups all damaged specimens had decreased ultimate strengths compared to the Baseline. The Baseline and Impact damaged specimens had approximately the same elastic compliance whilst the compression damaged had a higher level of compliance.

Table 7.1. Monotonic Tests For Each Specimen Type

Specimen Layup	**Specimen Type**	**Ultimate Load [N], [% of baseline specimen]**	**Yield Load [N], [% of baseline specimen]**
$[\pm 45_3]_s$	Baseline, 1-2-11	3612	2429
$[\pm 45_3]_s$	Impact, 1-1-9	3305 [91.5]	2357 [97.0]
$[\pm 45_3]_s$	Compression, 1-1-10	3177 [88.0]	1993 [82.0]
$[\pm 45_2/90_2]_s$	Baseline, 2-1-2	3960	3027
$[\pm 45_2/90_2]_s$	Impact, 2-1-3	3723 [94.0]	3141 [103.7]
$[\pm 45_2/90_2]_s$	Compression, 2-1-11	3582 [90.5]	2198 [72.6]

7.3 Crack Lengths

The length of the lead crack in each specimen was monitored and measured by the camera and image processing setup discussed in Section 4.2. The crack growth curves are seen in Figure 7.2.

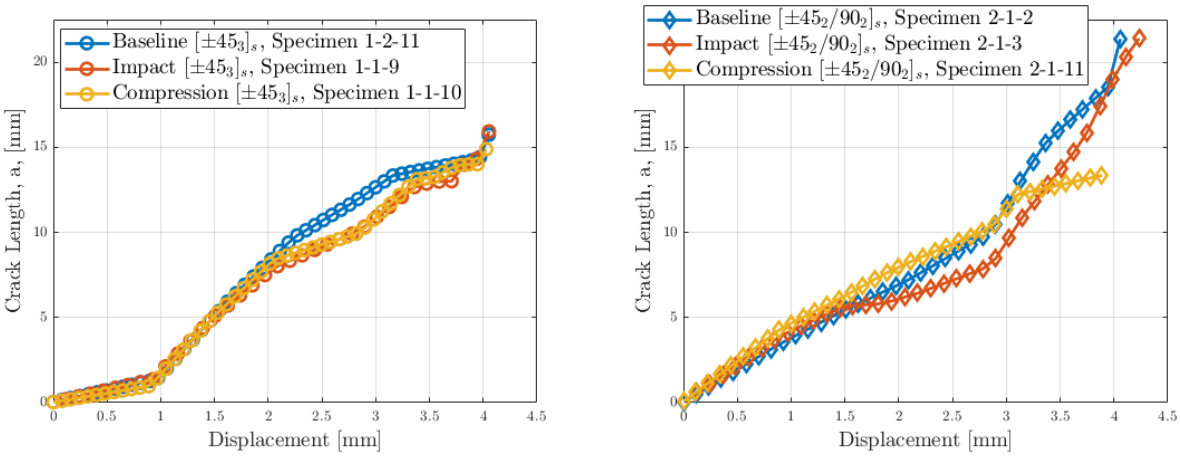

(a) $[\pm 45_3]_s$ (b) $[\pm 45_2/90_2]_s$

Figure 7.2. Monotonic crack growth

Consistent crack growth was seen from the outset of displacement for each case. In the $[\pm 45_3]_s$ layups, all specimens had slow but very consistent crack growth up until 1mm displacement, roughly equating to the reaching the elastic limit. After this point the crack growth rate greatly increased in all specimens, with the Baseline specimen having an approximately constant crack growth rate up until failure. The two damaged specimens both deviated from this constant crack growth rate and showed a reduction in crack growth rate, before having a rapid increase in crack growth rate shortly before failure. All specimens failed at near identical crack growth lengths, at near identical displacements.

The $[\pm 45_2/90_2]_s$ specimens similarly showed near constant crack growth rates until a displacement approximately equal to the proportional limit of the material was reached. After this point the Baseline and Compression specimens maintained the same crack growth rate until it failed, whilst the Impact specimen had a reduced lead crack growth after this point before failing at approximately 3mm displacement.

The crack length increase at ultimate load was in most cases quite small but represented a step jump in size.

7.4 Compliance

The outputted data collected from the MTS Test Suite was inputted into MATLAB for analysis. Compliance was calculated through the Compliance Calibration (CC) method, which uses the simple equation $C = \delta/P$ where δ is the experimental displacement and P is the experimentally measured force [68]. Force and displacement are measured at the load line (centre of the pinholes where the load is applied).

The calculated C data was plotted against the optically measured crack length, which was linearly interpolated in order to have an equivalent number of data points as the measured C. This data can be seen in Figure 7.3.

Data reduction was performed using a least squares fit and the derived compliance expression for the composite CT specimens [24, 69] as per Equation 7.1, where A_1, A_2, A_3 are fitting parameters, a is the crack length as measured from the load line (crack length as measured from the notch +25.3mm) and w is the distance from the notchtip to the end of the specimen. This reduction was found by Slepetz et al.[69] as the three terms used to find compliance represent the compliance contributions of shear stress, bending stresses and net section stress respectively.

$$C(a) = A_1(a/w) + A_2(a/w)^3 + A_3\left(\frac{2 + a/w}{(1 - a/w)^2}\right) \tag{7.1}$$

The derivative of the fitted curve, dC/da, was used in calculating the strain energy release rate of the material. The fitted curve was taken for each individual specimen.

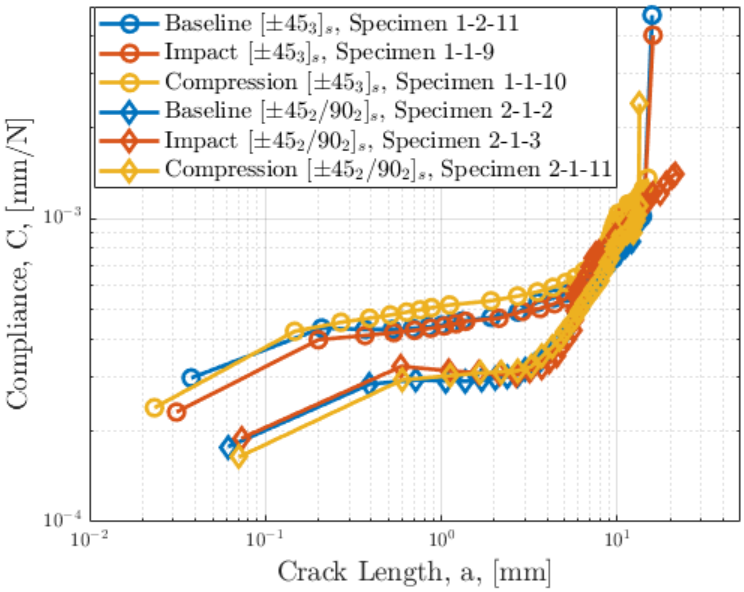

Figure 7.3. Compliance curve fitting

It can be seen that all specimens measured had nearly no increase in compliance until a moderate level of cracking occurred, equating to roughly 4mm for the $[\pm 45_3]_s$ specimen and 2mm for the $[\pm 45_2/90_2]_s$ specimen. Before this point, there was very close alignment in the compliance of both layup types in both the damaged and baseline configurations.

Once these crack length thresholds were reached, significant increases in compliance were seen, and both the $[\pm 45_3]_s$ and $[\pm 45_2/90_2]_s$ specimens converged to the same approximate compliance change rate.

7.5 Critical Strain Energy Release Rate

The strain energy release rate (SERR) of the six specimens under monotonic tension loading was calculated using Equation 2.1. The resultant plot for SERR is seen in Figure 7.4. The value of G_{IC} reported in Table 7.2 refers to the value of G_I at the the maximum load value as per ASTM D6671 [70].

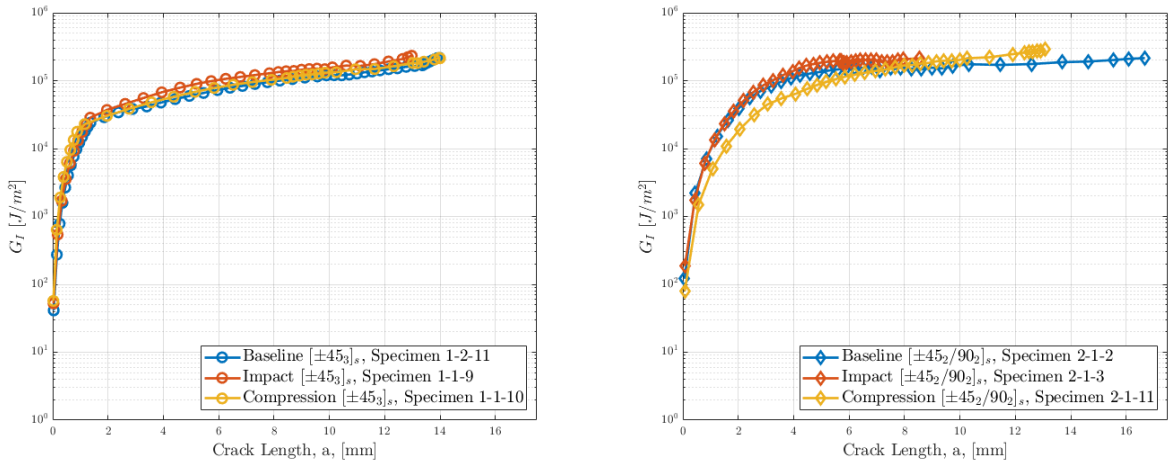

(a) $[\pm 45_3]_s$ (b) $[\pm 45_2/90_2]_s$

Figure 7.4. Monotonic strain energy release rate

The SERR for the $[\pm 45_3]_s$ specimens were near identical in each case which was an interesting result noting that both the Baseline and damaged specimens had different crack growth curves and ultimate loads. The strain energy release rate increased quickly from a minimum of approximately 40 J/m^2 increasingly rapidly by three orders of magnitude during the sudden onset of immediate crack growth. From this point, the strain energy release rate increased rapidly until failure occurred at approximately 0.22 MJ/m^2 for the Baseline and Compression samples, and at a slightly higher value of 0.246 MJ/m^2 for the Impact sample. The variation is likely well within what could be considered normal scatter and thus all three specimens would have the same critical SERR in this case. This equates to all $[\pm 45_3]_s$ specimens having an approximately equivalent fracture toughness, where fracture toughness (K_I) can be calculated from Equation 7.2[71]. E' is the experimentally measured value of Young's Modulus.

$$G_I = \frac{K_I^2}{E'} \tag{7.2}$$

In the $[\pm 45_2/90_2]_s$ layup samples a similar trend was seen. The strain energy release rate of both the Baseline and damaged specimens increased quickly from an initial value of approximately 100 J/m^2 to three orders of magnitude higher for the Baseline and Impact

samples, and two orders of magnitude by the Compression damaged sample, during the crack growth seen just after time zero. Following this, the strain energy release rate in each specimen increased until the critical strain energy release rate was achieved. This occurred at a mean value of $0.215 MJ/m^2$ for the Baseline and Impact specimens, and at a much higher value of $0.288 MJ/m^2$ for the Compression damaged specimen.

Table 7.2. Monotonic Strain Energy Release Rates

Specimen Layup	**Specimen Type**	**G_{IC} Critical Strain Energy Release Rate [MJ/m^2]**
$[\pm 45_3]_s$	Baseline, 1-2-11	0.219
$[\pm 45_3]_s$	Impact, 1-1-9	0.246
$[\pm 45_3]_s$	Compression, 1-1-10	0.222
$[\pm 45_2/90_2]_s$	Baseline, 2-1-2	0.218
$[\pm 45_2/90_2]_s$	Impact, 2-1-3	0.213
$[\pm 45_2/90_2]_s$	Compression, 2-1-11	0.288

7.6 Quasi-static Strain Energy Release Rate

As described in Section 2.2.4, there is some debate about the use of G and its derivatives as a similitude parameter due to its non-physical based methodology. An alternative is offered in the form of G^* which is the average SERR per cycle. This can be calculated in a monotonic test by treating it as a low cycle fatigue test and using the area method as per Amaral et. al [26]. For monotonic tests, particularly within DCB specimens, it is common to use the area method to understand the actual energy exerted per unit extension of crack area. The area method can be used to calculate the parameter G^* as per Equation 2.8.

The method requires finding force drops from within the force-displacement curve and calculating the area under each drop. Amaral et al.[26] use a similar process but determine the area under each load drop from the load-displacement line deviations to the origin. This area-integral is discretised five times into increasingly finer meshes in their study with each being plotted separately, allowing for a linear, least-squares, line of best fit to be plotted,

representing the value dU. The crack growth rate, da, was calculated by the displacement of each load drop. It should be noted that the discretisation is for analysis only and the energy released per crack length increase does not change.

The inverse of the slope of the line of best fit $\frac{1}{da/dU}$ is the value G^* which represents the average quasi-static strain energy release rate (Equation 2.8).

Figure 7.5 shows monotonic tension data from this study for Specimen 1-1-10. In Figure 7.5a, load drops have been identified by a script that detected deviations from the moving-average by a certain tolerance. The identified points have been highlighted in both figures. Figure 7.5b shows a close up view of the detected load drops.

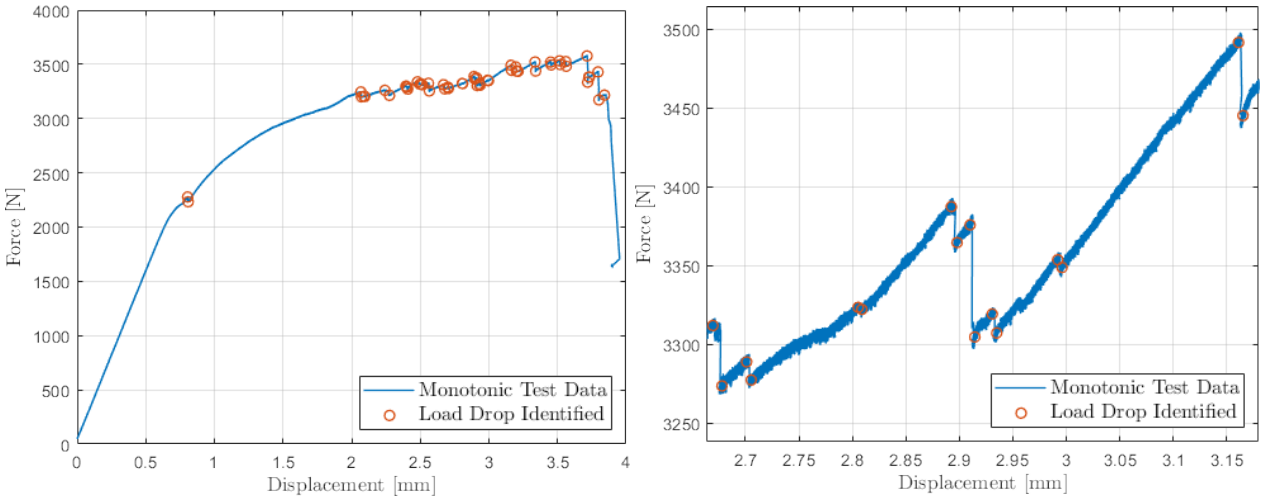

(a) Sample identified load drops

(b) Close up

Figure 7.5. Load drop identification

As above, the area under each load drop was found and discretised ten times with decreasing grid size. This occurred for each six specimens; one baseline and two damaged specimens for each of the layups. The resultant discretised areas dU, and the crack growth rate da, and their respective lines of best fit are plotted in Figure 7.6. The line of best fit in each case exceeded a $R^2 = 0.98$. The values of G^* have been outputted into to Table 7.3.

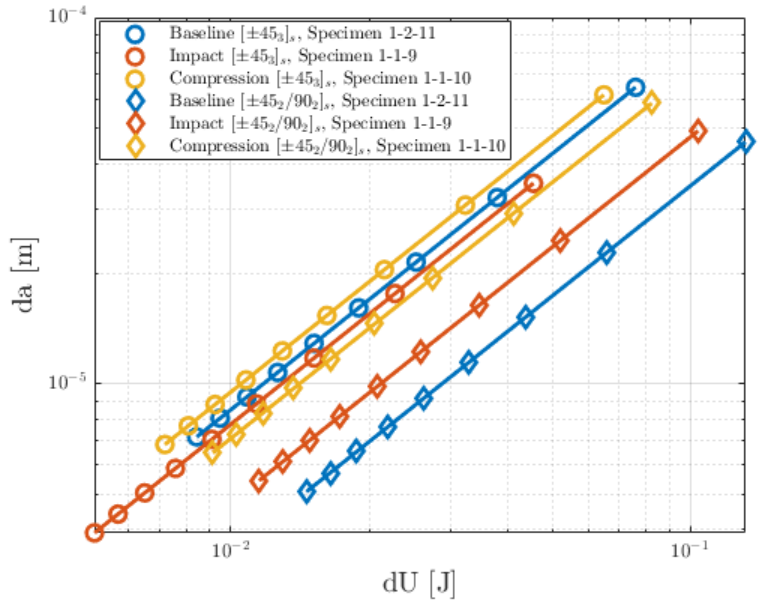

Figure 7.6. Monotonic change in energy vs crack growth rate

Each specimen produced a unique slope dU/da and hence a unique G^*. It was seen that the $[\pm 45_3]_s$ specimens had very similar lines of best fit, all banded within a tight tolerance. The average G^* for this layup was 0.548 MJ/m^2 which is only slightly lower than the Baseline specimen result. The $[\pm 45_2/90_2]_s$ layup has more spread data across the three tests however the lines of best fit are still parallel in the log-log plot. The mean value of the three $[\pm 45_2/90_2]_s$ specimens was 0.997 MJ/m^2.

Table 7.3. Monotonic Average Strain Energy Release Rates

Specimen Layup	**Specimen Type**	$\mathbf{G^*_{quasi-static}}$ **[MJ/m²]**
$[\pm 45_3]_s$	Baseline, 1-2-11	0.550
$[\pm 45_3]_s$	Impact, 1-1-9	0.602
$[\pm 45_3]_s$	Compression, 1-1-10	0.492
$[\pm 45_2/90_2]_s$	Baseline, 2-1-2	1.343
$[\pm 45_2/90_2]_s$	Impact, 2-1-3	0.988
$[\pm 45_2/90_2]_s$	Compression, 2-1-11	0.658

7.7 Stress Intensity Factor

Stress Intensity Factor (K_I) was also analysed after the monotonic tensile testing as per ASTM [57] through the measurement of the non-dimensional crack length extension and the specimen type correction factor as per Equation 7.3 [72].

$$K_I = \frac{P}{B}\sqrt{\frac{\pi}{W}}\left[16.7\alpha^{1/2} - 104.7\alpha^{3/2} + 369.9\alpha^{5/2} - 573.8\alpha^{7/2} + 360.5\alpha^{9/2}\right] \tag{7.3}$$

Where $\alpha = a/W$, a is the crack length, W is the specimen length, and B is the specimen thickness.

Figure 7.7 shows the results of the stress intensity factor for both the $[\pm 45_3]_s$ and $[\pm 45_2/90_2]_s$ specimens under monotonic loading.

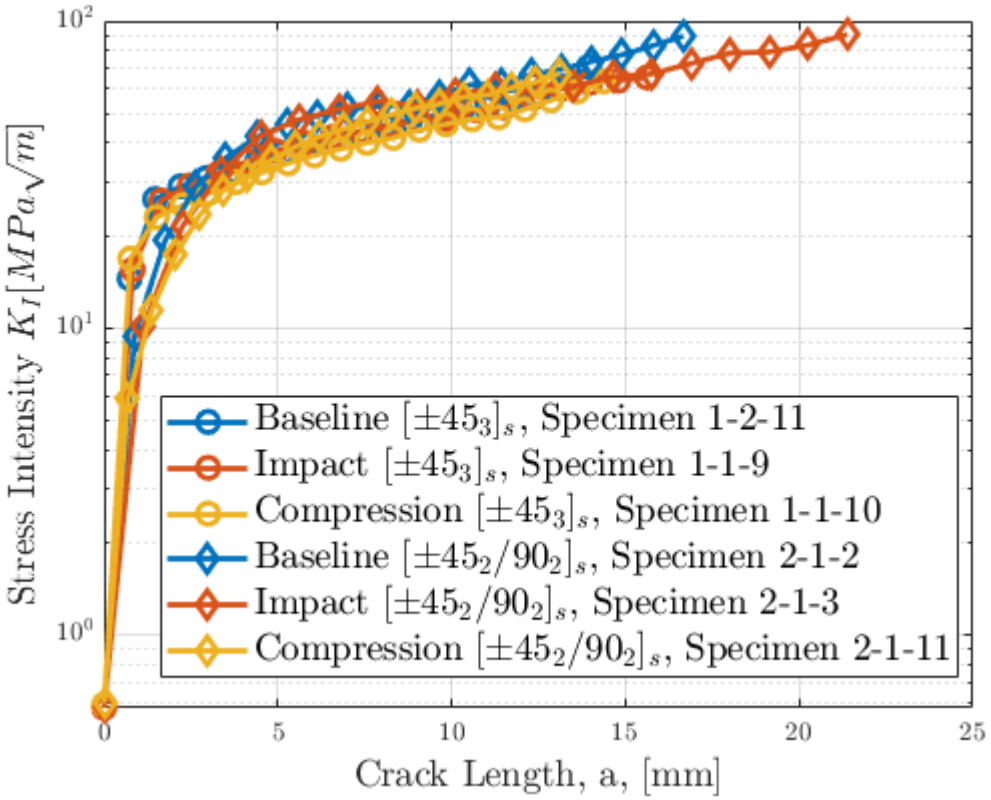

Figure 7.7. Monotonic stress intensity factor

The figure shows consistent increase in K_{IC} with increasing crack length for all specimens. Consistency can be seen between all specimens of the same layup type with little variation. Results are similar to those predicted by Equation 7.2 which uses measured compliance and crack growth, rather than just the crack lengths as seen in Equation 7.3.

Both layup types see rapid linear growth in K_{IC} before a reduced growth rate is seen at a crack length of 1mm for the $[\pm 45_3]_s$ layup and 3mm for the $[\pm 45_2/90_2]_s$ layup.

The peak K_{IC} value for each specimen is listed in Table 7.4.

Table 7.4. Monotonic K_{IC}

Specimen Layup	**Specimen Type**	**K_{IC} [MPa$\sqrt{m}$]**
$[\pm 45_3]_s$	Baseline, 1-2-11	70.97
$[\pm 45_3]_s$	Impact, 1-1-9	65.49
$[\pm 45_3]_s$	Compression, 1-1-10	63.55
$[\pm 45_2/90_2]_s$	Baseline, 2-1-2	89.37
$[\pm 45_2/90_2]_s$	Impact, 2-1-3	90.38
$[\pm 45_2/90_2]_s$	Compression, 2-1-11	67.56

The mean value for the $[\pm 45_3]_s$ layup was 66.67 $MPa\sqrt{m}$ and 82.43 $MPa\sqrt{m}$ for the $[\pm 45_2/90_2]_s$ layup.

8. FATIGUE TESTING

This chapter will discuss the setup, conduct and results of the fatigue testing undertaken as part of this research.

8.1 Test Setup

This section will describe how certain fatigue loading parameters were decided upon, as well as the final fatigue testing characteristics.

8.1.1 Load Level

Fatigue tests were conducted using the MTS and camera acquisition setup discussed in Chapter 4. The tests were under force control with maximum and minimum loads determined with reference to the monotonic tension tests. In total eighteen successful fatigue tests were conducted.

The initial loading aim was to use a load of $P_{max} = 0.8 \cdot F_{yield}$ as per Ortiz-Morales et al. and Hahan et al. [31, 34], however the crack growth rate was deemed too small to lead to failed in a reasonable time frame.

The initial aim was to test the CT specimens to failure however significant difficulty was had in achieving this aim with the specimens showing significant damage tolerance under low and medium loading, and sudden fatigue crack growth and brittle failure under high loads. High loads (above $P = 70\%F_{ULT}$) typically had life's less than 10000 cycles, however due to the issues discussed in Chapter 4, the out-of-plane bending made compliance and crack length measurements difficult.

Specimen 1-2-7 was used to determine acceptable load levels and frequency for stable and reliable crack growth with the hope of achieving failure. The specimen was tested under incrementally increasing load until failure occurred.

The load vs cycle diagram can be seen in Figure 8.1. Final failure occurred at $P = 0.825 \cdot F_{ULT}$ after 15.7 million cycles (8 weeks of testing) which showed the significant fatigue resistance of the specimen.

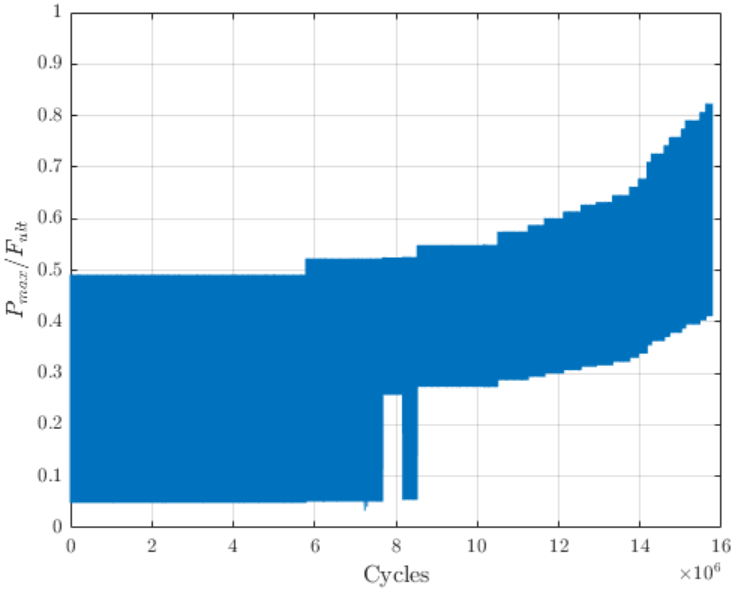

Figure 8.1. Fatigue loading determination testing

Whilst the specimen cycled 150k times at the maximum load, running a new specimen at this load level caused near instant failure. This may be due to relaxation effects discussed in Stinchcomb et al. [9] where fatigue loaded specimens actually had a higher monotonic strength after a number of cycles due to fibre-breakage relaxation effects within the laminate.

With the range of fatigue cycles to failure ranging from near instant to 15.7m cycles, it was chosen to complete testing at a number of constant load levels for a determined amount of cycles in order to get a broad understanding of the material behaviour. One million cycles at $F_{ULT} = 42\%, 50\%, 60\%$ were chosen due to the reliable results seen at these load levels.

8.1.2 Frequency

A frequency of 5Hz was used for each test which allowed for shorter tests duration. Before starting testing on each layup type, the MTS Station Manager Tuning tool was used to adjust the PID (proportional-integral-derivative) controls to ensure that peak loads were accurately achieved at each load level. The error in peak loads was 1-3N in each case (~0.2%).

8.1.3 R-ratio

Testing was carried out at an R-ratio of 0.5 with the exception of three early tests which were carried out at R=0.1 ($[\pm 45_3]_s$ Specimens 1-1-11, 1-1-3 and 1-1-12).

8.1.4 Data Capture

Data was captured by the MTS Test Suite at a minimum of 102Hz however later tests were carried out at 512Hz. The data was captured for 10 seconds every 2 minutes to limit the data size, noting tests were typically three days in duration. This reduced data output file size from 1-2GBs to 100-200MBs.

The raw data text file outputted from the MTS Test Suite was inputted into MATLAB for analysis.

8.1.5 Alignment

Prior to each test, alignment of each specimen was carried out in accordance with ASTM Standards[56, 57]. As per Section 4.3, minor out-of-plane bending was present in most tests, though it was more significant in the 'High' load tests. As per Figure 4.3 an aluminium plate was used to minimise deflection of the specimen under load. Under high loads, the backing plate was stabilised with weights to stop it deflecting under the force applied to it from the deflecting specimen.

8.2 Fatigue Test Overview

Table 8.1 lists the fatigue tests run during the course of this study.

Table 8.1. Fatigue Tests

Specimen Layup	**Load Level [$\mathbf{P_{max}/F_{ULT}}$]**	P_{max} **[N]**	**R-ratio**	**Specimen Type**	**Specimen Number**
$[\pm 45_3]_s$	Test case - Inc. up to 82.5%		0.1, 0.5	Baseline	1-2-7
$[\pm 45_3]_s$	Low [42%]	1509	0.1	Baseline	1-1-11
$[\pm 45_3]_s$	Low [42%]	1509	0.1	Impact	1-1-3
$[\pm 45_3]_s$	Low [42%]	1509	0.1	Compression	1-1-12
$[\pm 45_3]_s$	Low [42%]	1509	0.5	Baseline	1-2-2
$[\pm 45_3]_s$	Low [42%]	1509	0.5	Impact	1-2-3
$[\pm 45_3]_s$	Medium [50%]	1806	0.5	Baseline	1-1-8
$[\pm 45_3]_s$	Medium [50%]	1806	0.5	Impact	1-2-6
$[\pm 45_3]_s$	Medium [50%]	1806	0.5	Compression	1-2-5
$[\pm 45_3]_s$	High [60%]	2167	0.5	Baseline	1-2-4
$[\pm 45_3]_s$	High [60%]	2167	0.5	Impact	1-1-6
$[\pm 45_3]_s$	High [60%]	2167	0.5	Compression	1-1-2
$[\pm 45_2/90_2]_s$	Low [42%]	1663	0.5	Baseline	2-1-1
$[\pm 45_2/90_2]_s$	Low [42%]	1663	0.5	Impact	2-1-7
$[\pm 45_2/90_2]_s$	Low [42%]	1663	0.5	Compression	2-1-6
$[\pm 45_2/90_2]_s$	High [60%]	2376	0.5	Baseline	2-1-4
$[\pm 45_2/90_2]_s$	High [60%]	2376	0.5	Impact	2-1-8
$[\pm 45_2/90_2]_s$	High [60%]	2376	0.5	Compression	2-1-5

8.3 Crack Length

The length of the lead crack in each specimen was monitored and measured by the camera and image processing setup discussed in Section 4.2. The crack growth curves are seen in Figure 8.2. Molent et al. [73] has previously shown that the lead crack framework is applicable to aerospace composite material, and it appeared to work well in this study.

A minimum of two cracks grew in each case, in the ±45 direction from the notch. These cracks (or any additional) were allowed to grow throughout the ~1 million cycles, at which point the lead crack was determined as the largest crack present at test end. This crack was then measured at intervals throughout the test using the images that were saved every 2.5k cycles.

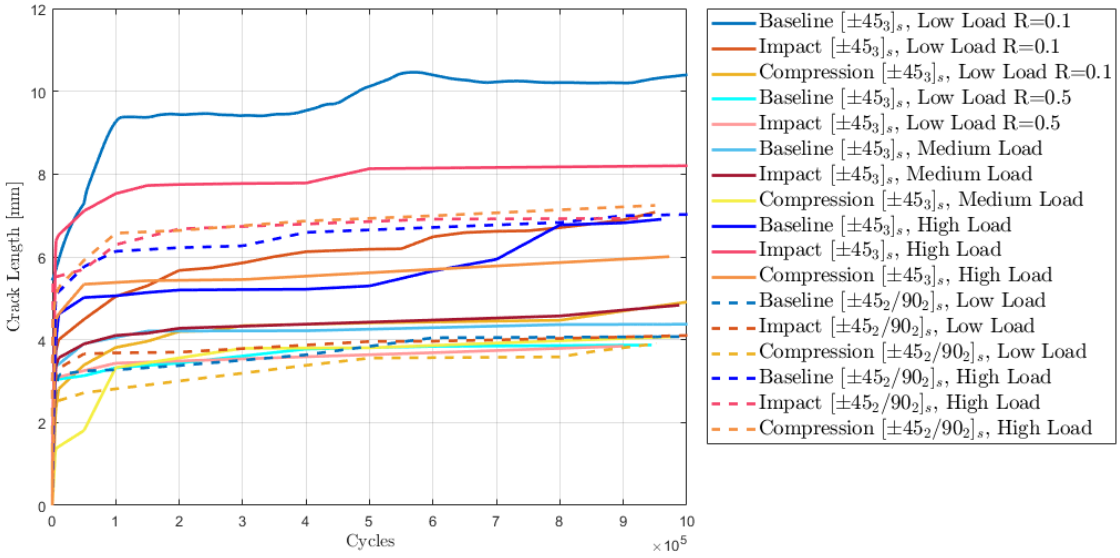

Figure 8.2. Lead crack lengths

Limiting the tests to approximately 1 million cycles had the impact of not being able to see the lead crack grow to failure of the specimen. The lead crack always had three commonalities, cracks initiated during the first cycles (1-50 cycles), initial unstable growth to a large size of 3-9mm (5-10 thousand cycles), followed by constant growth until the test was stopped.

There was some divergence in the length of the initial unstable crack growth, that showed little correlation to the stress applied.

8.4 Crack Growth Rate

The crack growth rate was determined using the secant method as described in ASTM E647 [57]. The secant method is a point to point, forward-difference method to calculate the

derivative of a curve. More complex methods for calculating are also available, such as the incremental polynomial method, however some research [74] has shown that the polynomial method may mask actual changes in da/dN. For this reason and the added complexity it was not used.

From Figure 8.2 it can be seen that due to the limited resolution of the camera setup, crack lengths changes were only able to be detected in sufficient clarity every 50-200 thousand cycles, creating a very staggered, stepped, da/dN plot (noting the derivative of straight line is a constant) which is not necessarily representative of the actual crack growth rate, and more representative of the limited data points available. A line of best fit through these constant crack growth rates was used, alongside the mean da/dN at each step was instead plotted, and is considered more representative of the actual crack growth rate.

In future work, the calculation of crack length from the specimen's compliance as per ASTM E647 [57] may be a good alternative. This was attempted however unintuitive results were attained initially.

8.5 Compliance

Compliance was calculated from the Compliance Calibration (CC) method using the data collected from the MTS Test Suite after it was inputted into MATLAB. This method uses which uses the equation $C = \delta/P$ where δ is the experimental displacement and P was the maximum force set in each cycle. Displacement was determined from the MTS cross-head displacement which is less accurate than if displacement gauges or precision optical/voltage measurement equipment was used.

Initial attempts at calculating C found the peak value of the specimen's load line displacement (findpeaks MATLAB function) at each and every cycle however the output result had too much scatter for analysis. Segmenting the displacement data into 50 equally spaced subsets and finding the mean displacement of each cycle within this data subset worked significantly better and allowed for the trend to be observed.

The calculated C data was plotted against the optically measured crack length in each case, and a least-squares power law curve fit was calculated. The compliance curve for

Specimen 1-1-3 is shown in Figure 8.3. The compliance equation (Equation 7.1) for CT specimens [24, 69] as used in the monotonic testing did not work well with the calculated fatigue compliance results, whereas a power law fit was able to get accurate results.

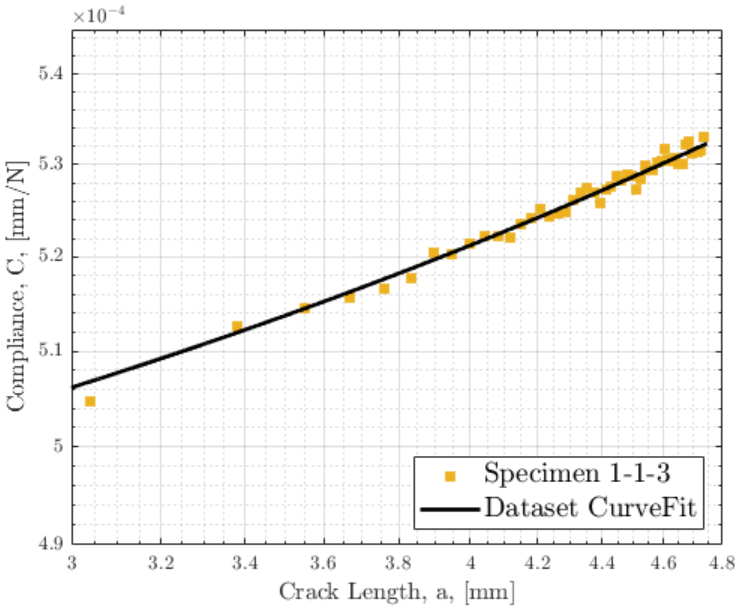

Figure 8.3. Fatigue compliance curve fit (Specimen 1-1-3)

The derivative of the fitted curve, dC/da, was used in calculating the strain energy release rate of the material.

8.6 Strain Energy Release Rate, G

The strain energy release rate (SERR) of each specimen was calculated from Equation 2.1 in two forms, the maximum strain energy release rate G_{max}, and the strain energy release rate range $\Delta\sqrt{G}$, where $\Delta\sqrt{G} = \sqrt{G_{max}} - \sqrt{G_{min}}$.

The next sections will describe the results for G_{max}, and $\Delta\sqrt{G}$.

8.6.1 G_{max}

The output maximum SERR is shown in Figure 8.4 and 8.5 for the $[\pm 45_3]_s$ and $[\pm 45_2/90_2]_s$ specimens respectively. They are shown along side the baseline critical SERR as found from the monotonic tests.

Significant crack growth rates were seen in both the $[\pm 45_3]_s$ and $[\pm 45_2/90_2]_s$ layups with SERRs well below the monotonic critical strain energy release rate. This can be used to infer that the analysis of fatigue crack growth in CFRPs is extremely important and cannot be ignored, as the energy required to achieve growth is greatly reduced than just from monotonic loading.

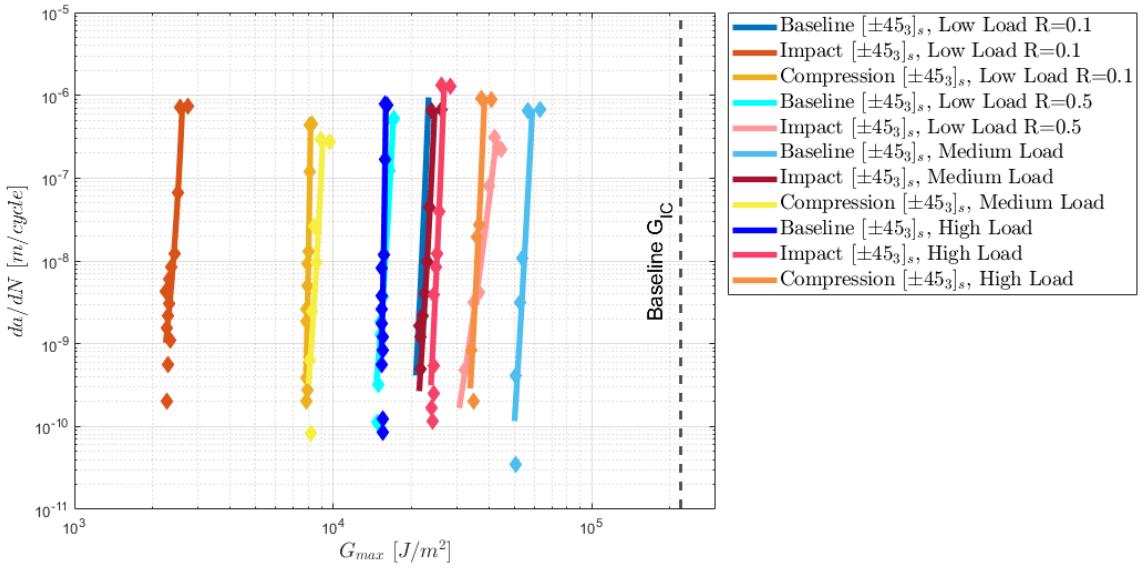

Figure 8.4. G_{max} results for the $[\pm 45_3]_s$ specimens

The $[\pm 45_3]_s$ specimens had a threshold G_{max} of between $2 \cdot 10^3$ and $5 \cdot 10^4$ J/m^2, correlating to a crack growth rate of approximately 10^{-10} m/cycle. The $[\pm 45_2/90_2]_s$ layup had a higher threshold G_{max} of between $1.6 \cdot 10^3$and $5 \cdot 10^3$ J/m^2 for a crack growth rate of approximately 10^{-10} m/cycle. Therefore 133-1000% more energy is required in $[\pm 45_3]_s$ specimen for the same crack growth rate compared to the $[\pm 45_2/90_2]_s$ layup. There is however much greater scatter in the $[\pm 45_3]_s$ specimen as it has over a full order of magnitude of scatter, compared to the $[\pm 45_2/90_2]_s$ which has a scatter of only ~2.

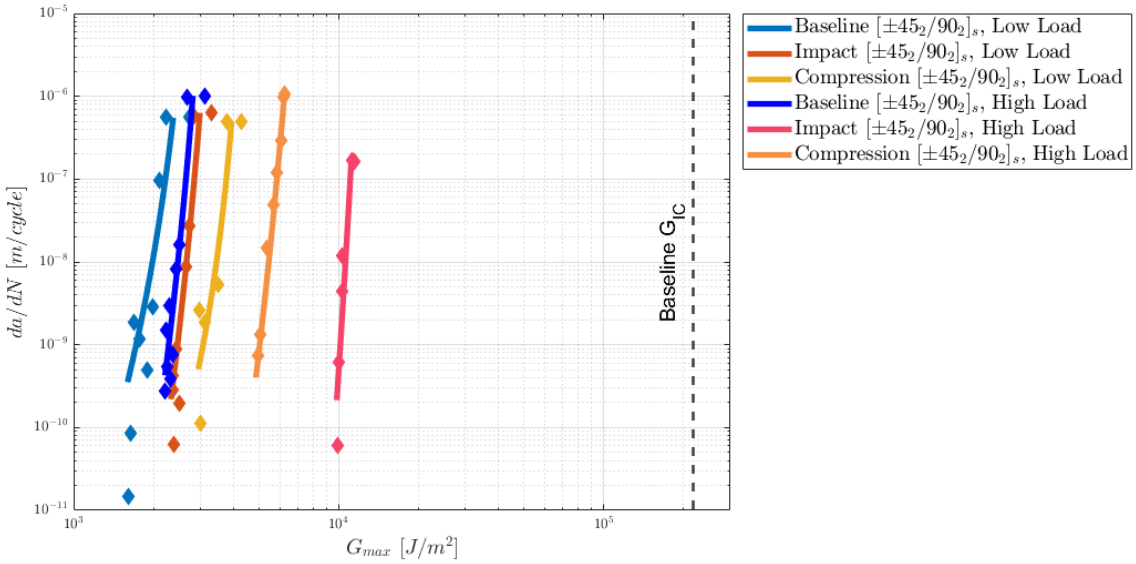

Figure 8.5. G_{max} results for the $[\pm 45_2/90_2]_s$ specimens

On average it could be said that Baseline specimens (blue shaded lines) tend to be more damage tolerant than the damaged specimens (red and yellow lines) for the $[\pm 45_3]_s$ specimen, however this is not the case for the $[\pm 45_2/90_2]_s$ specimen type which shows the Baseline specimens were actually the least damage tolerant, and the Impact specimen the most. It was shown previously that the process of indenting a specimen (Section 5) initiates sub-surface delaminations between Ply 1 and 2, and 11 and 12 before fatigue loading. It was also seen that there is significant fibre buckling, as well as a large amount of intralaminar cracks formed in Compression damage specimens (Chapter 6. Intuitively you would therefore expect all damaged specimens to be more critical and less damage tolerant.

8.6.2 $\Delta\sqrt{G}$

The output SERR range is shown in Figure 8.6 and 8.7 for the $[\pm 45_3]_s$ and $[\pm 45_2/90_2]_s$ specimens respectively. The SERR range is often put forward as a similitude parameter for composite materials due to its mathematical connection to the metallic similitude parameter ΔK [14].

Similar to G_{max}, the $[\pm 45_3]_s$ layup has significantly more scatter across the range of specimens than the $[\pm 45_2/90_2]_s$ layup. The threshold SERR range for the $[\pm 45_3]_s$ layup is between 41 and 130 $\sqrt{J/m^2}$, and 20 and 35 $\sqrt{J/m^2}$ for the $[\pm 45_2/90_2]_s$ layup. The $[\pm 45_2/90_2]_s$ layup is therefore less damage tolerant than the $[\pm 45_3]_s$ layup using the $\Delta\sqrt{G}$ metric, requiring approximately 2-3.7 times less energy to have a crack growth rate of approximately 10^{-10} m/cycle. This is an interesting result since the $[\pm 45_2/90_2]_s$ specimens have generally better monotonic properties.

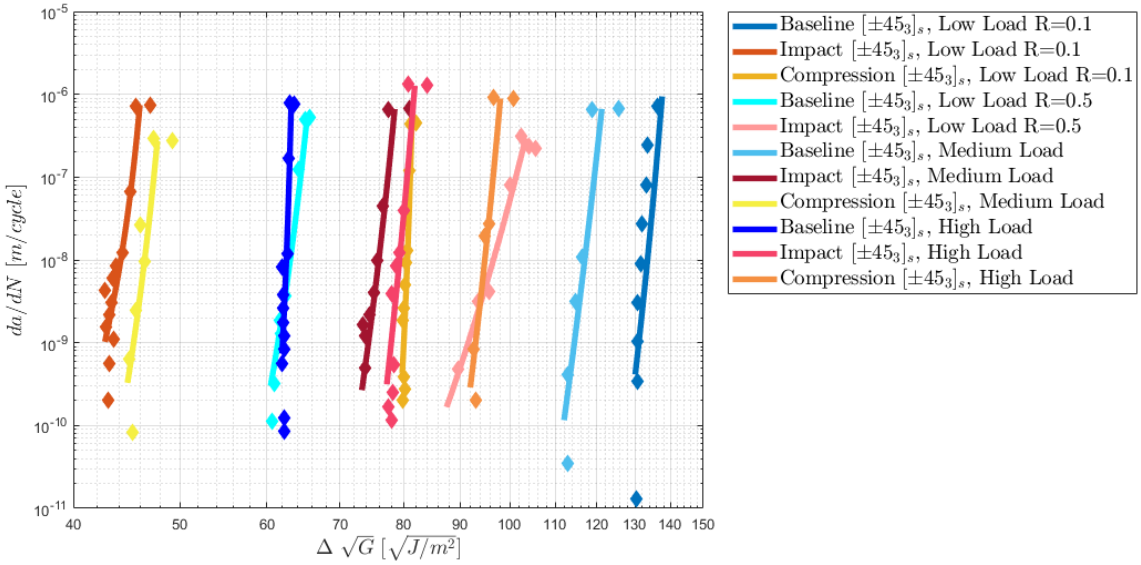

Figure 8.6. $\Delta\sqrt{G}$ results for the $[\pm 45_3]_s$ specimens

Using $\Delta\sqrt{G}$, the same trend to G_{max} was seen in that for the $[\pm 45_3]_s$ layup the Baseline specimens tended on average to be more damage tolerant and the pre-damaged specimens less, though some Baseline samples were less damage tolerant than their damaged counterparts which were run at the same load level. This is seen more in Figure 8.8. In the case of the $[\pm 45_2/90_2]_s$ layup, the Baseline specimens actually performed worse, having the least damage tolerant performance, whilst the Impact damage samples had the best.

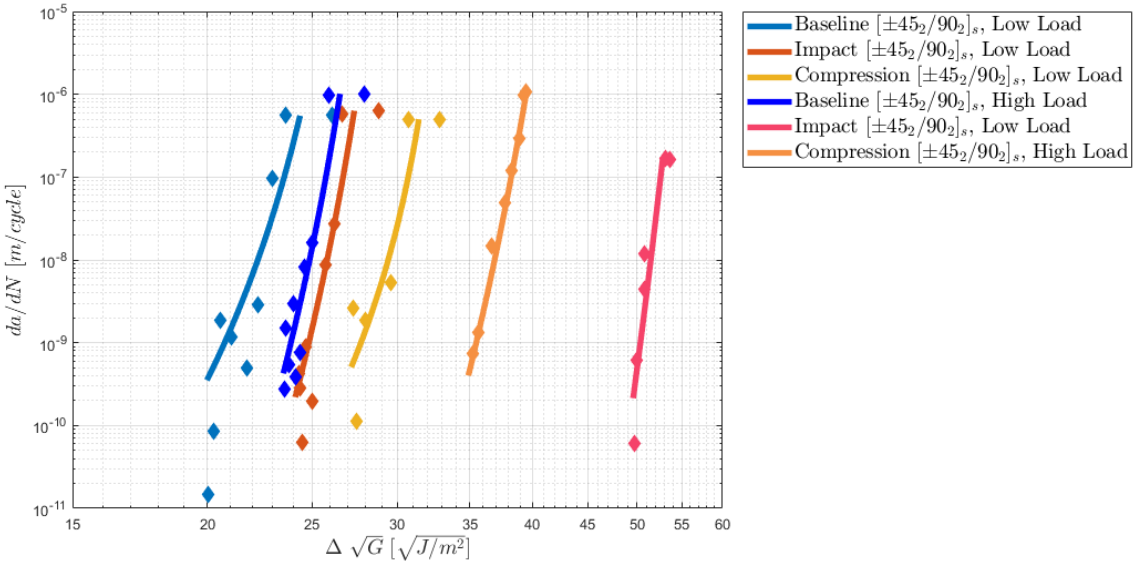

Figure 8.7. $\Delta\sqrt{G}$ results for the $[\pm45_2/90_2]_s$ specimens

Figure 8.8 a)-d) shows the $\Delta\sqrt{G}$ results for each individual load level and R-ratio. Against expectations, sub-figures b) and d) show the opposite trend to what should be expected for a similitude parameter, showing the pre-damaged specimen requiring more energy to grow at the same crack growth rate than the Baseline. In Chapter 9 the analysis of each specimen is undertaken to see if their is a micro-structural reason for this to occur.

Sub-figure a) shows that the Baseline specimen requires 130 $\sqrt{J/m^2}$ to propagate at 10^{-10} m/cycle, compared to just 41.5 $\sqrt{J/m^2}$ for the Impact damaged specimen, roughly a 3:1 energy level difference for the same crack growth rate. At the same maximum load in sub-figure b) but a higher mean stress (R=0.5), the opposite is seen, with the Baseline requiring 60 $\sqrt{J/m^2}$ to propagate at 10^{-10} m/cycle, compared to 85 $\sqrt{J/m^2}$ for the Impact damaged specimen. The difference between the two specimens is much smaller in the second case which could mean that the difference is just scatter however this would require further testing and analysis with multiple specimens of the same type.

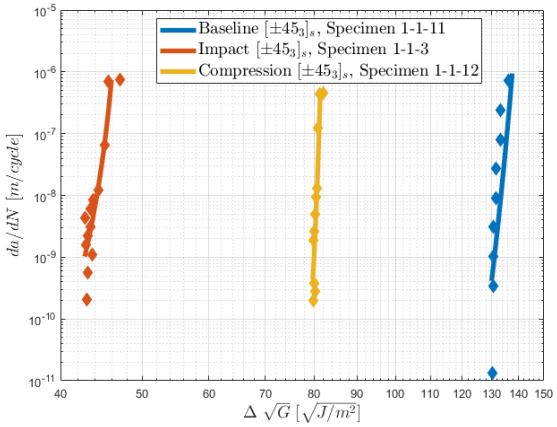

(a) $P_{max} = 42\% \cdot F_{ULT}$, R=0.1

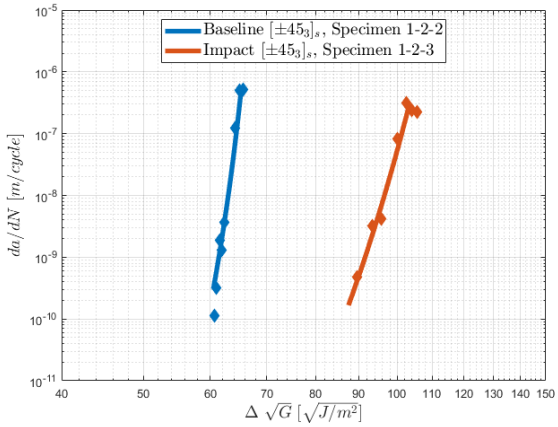

(b) $P_{max} = 42\% \cdot F_{ULT}$, R=0.5

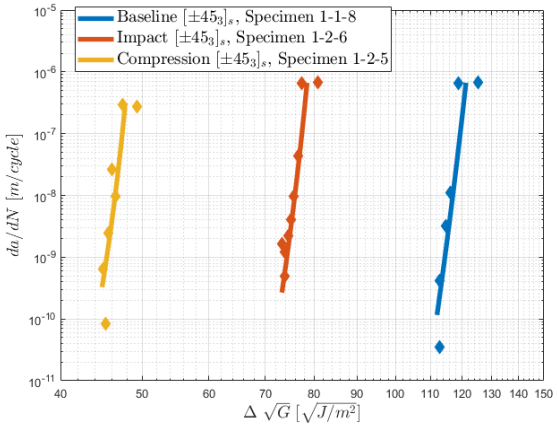

(c) $P_{max} = 50\% \cdot F_{ULT}$

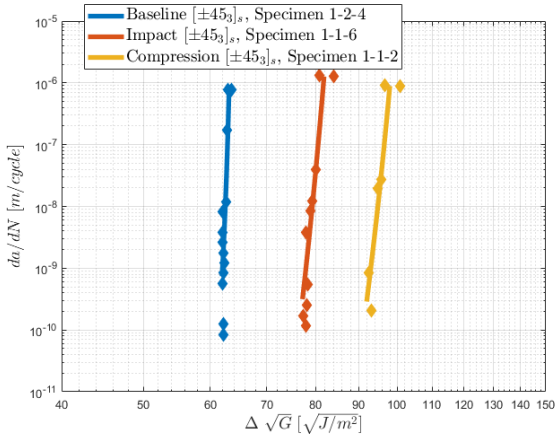

(d) $P_{max} = 60\% \cdot F_{ULT}$

Figure 8.8. $[\pm 45_3]_s$ $\Delta\sqrt{G}$ - detailed view of specific mean stresses

At individual load levels in the $[\pm 45_2/90_2]_s$ layup a trend is visible. The Baseline Specimen performs worse than the pre-damaged specimens, but the magnitude of differences in each specimen is small. Similar to Figures 8.8 b) and d), this trend is the opposite to what would be intuitively expected as you would expect the damaged specimen to have a lower damage tolerance. Figure 8.9 a) shows that the Baseline specimen requires 20 $\sqrt{J/m^2}$ to propagate at 10^{-10} m/cycle, compared to just 28 $\sqrt{J/m^2}$ for the Compression specimen. Figure 8.9 b) shows that the Baseline specimen requires 24 $\sqrt{J/m^2}$ to propagate at 10^{-10} m/cycle, compared to just 35 $\sqrt{J/m^2}$ for the Compression specimen. Both of these examples are

largely non-physical noting the extend of the pre-existing damage created in the Compression samples.

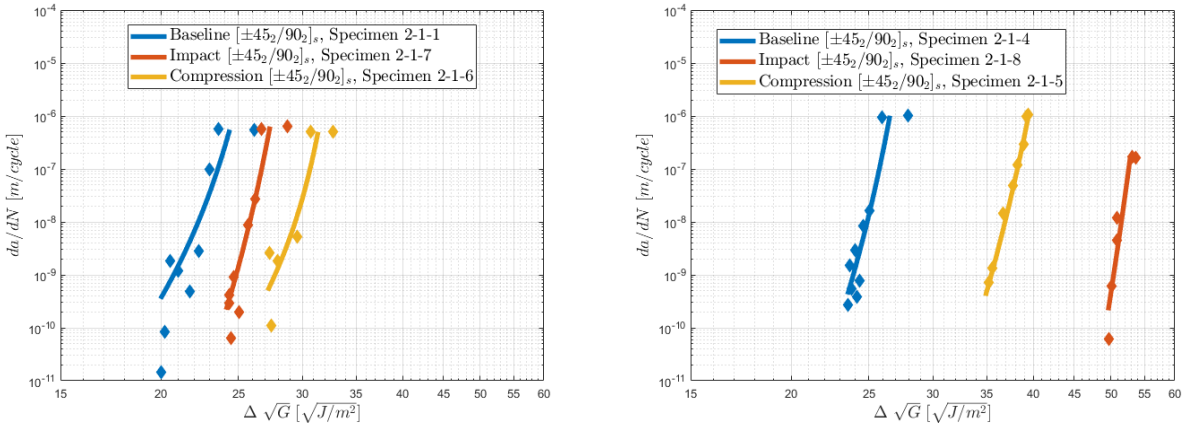

(a) $P_{max} = 42\% \cdot F_{ULT}$ (b) $P_{max} = 60\% \cdot F_{ULT}$

Figure 8.9. $[\pm 45_2/90_2]_s$ $\Delta\sqrt{G}$ - detailed view of specific mean stresses

8.6.3 Modified Hartman-Schijve Equation Similitude Parameter, $\Delta\kappa$

The similitude parameter $\Delta\kappa$ was plotted for both layup types. $\Delta\kappa$ is defined in Equation 2.2 from Jones et al.[18].

The process of developing the plot involved the using the scaling parameters A and $\Delta\sqrt{G_{thr}}$ until the modified Hartman-Schijve function best fits the experimental dataset for the entire range of crack growth[14, 75, 18, 76].

A simple code was written that varied the values of A incrementally until the mean value of $\Delta\sqrt{G}$ of each data set aligned. $\Delta\sqrt{G_{thr}}$ was also varied to try and perfect the alignment of the curves. The output graphs are seen in Figures 8.10 and 8.11, with the values of A and $\Delta\sqrt{G_{thr}}$ displayed in Table 8.2 and 8.3, for the $[\pm 45_3]_s$ and $[\pm 45_2/90_2]_s$ layups $[\pm 45_3]_s$ respectively. The initial values set within the script were $A = 1.33 \cdot G_{max}$, and $\Delta\sqrt{G_{thr}}$ at $\sqrt{0.5 \cdot \Delta G_{th}}$, where G_{th} is the value of $\Delta\sqrt{G}$ for a delamination growth rate of 10^{-10} m/cycle[15], which seemed to work well.

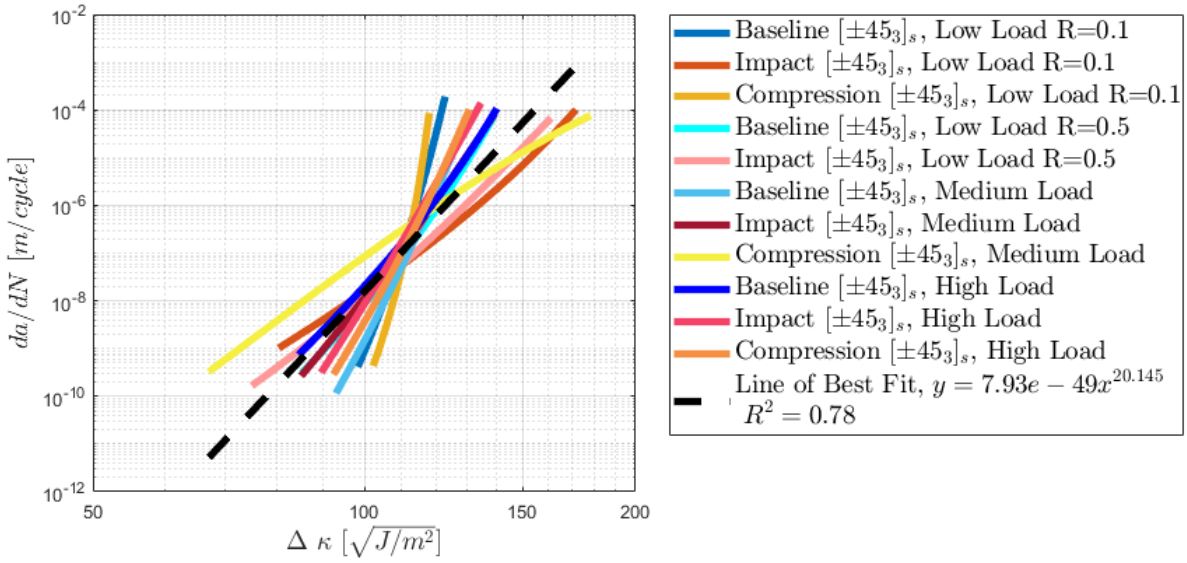

Figure 8.10. $[\pm 45_3]_s$ $\Delta\kappa$ results

As can be seen in the above figure, there is still some scatter between the curves, causing a lower coefficient of determination than desired for a similitude parameter. This is likely due to the large amount of difference seen in the original $\Delta\sqrt{G}$ data between each curve. The final values of constants D and n for the $\Delta\kappa$ similitude parameter was found to be $7.94e-49$ and 20.15 respectively.

The constant values listed in Table 8.2 show little direct correlation to either similarly damaged/un-damaged specimens or the load level they were tested at, though only one test was carried out at each condition (load and damage type) which makes determining sources of error harder.

Table 8.2. $[\pm 45_3]_s$ $\Delta\kappa$ Fitting Constants

Specimen Layup	**Load Level** $[\mathbf{P_{max}/F_{ULT}}]$	**Specimen Type**	**Specimen**	**A** $[\mathbf{kJ/m^2}]$	$\mathbf{\Delta\sqrt{G_{thr}}}$ $[\sqrt{\mathbf{J/m^2}}]$
$[\pm 45_3]_s$	Low [42%]	Baseline	1-1-11	65.8	65.0
$[\pm 45_3]_s$	Low [42%]	Impact	1-1-3	2.9	28.4
$[\pm 45_3]_s$	Low [42%]	Compression	1-1-12	10.9	39.9
$[\pm 45_3]_s$	Low [42%]	Baseline	1-2-2	38.4	38.8
$[\pm 45_3]_s$	Low [42%]	Impact	1-2-3	92.8	46.7
$[\pm 45_3]_s$	Medium [50%]	Baseline	1-1-8	123.3	56.0
$[\pm 45_3]_s$	Medium [50%]	Impact	1-2-6	32.4	36.6
$[\pm 45_3]_s$	Medium [50%]	Compression	1-2-5	10.2	22.4
$[\pm 45_3]_s$	High [60%]	Baseline	1-2-4	6.9	19.6
$[\pm 45_3]_s$	High [60%]	Impact	1-1-6	36.0	38.6
$[\pm 45_3]_s$	High [60%]	Compression	1-1-2	59.8	46.0

In the $[\pm 45_2/90_2]_s$ case, visual alignment of the data was better, with the exception of the high load impact specimen. The coefficient of determination was slightly better than for the alternate layup type, allowing a reasonable understanding of the value of the $\Delta\kappa$ similitude parameter, with the final constant values determined to be $D = 5.06\text{e} - 31$ and $n = 15.7$.

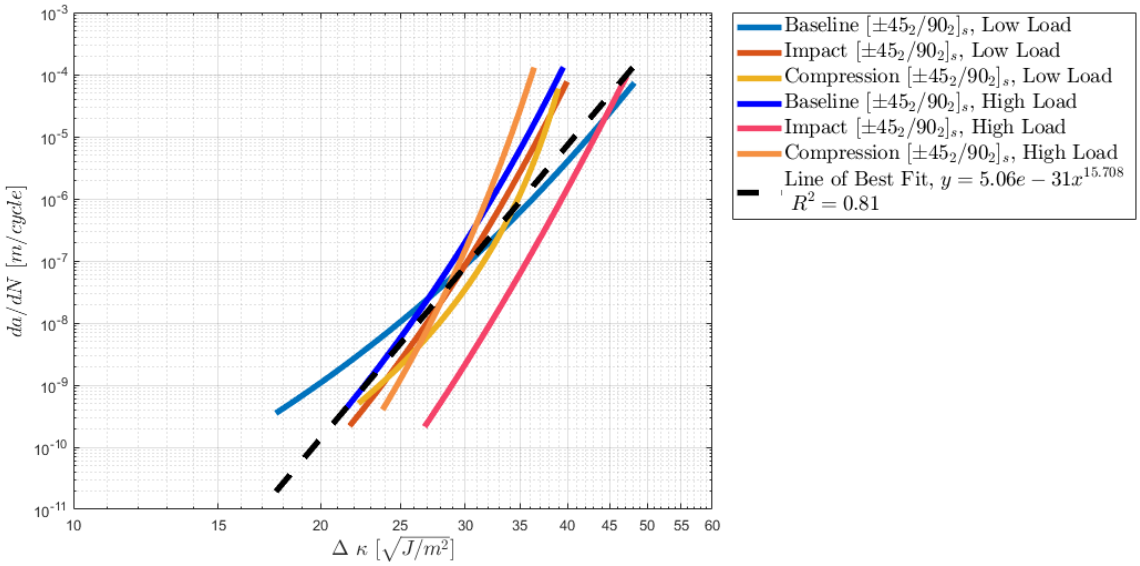

Figure 8.11. $[\pm 45_2/90_2]_s$ $\Delta\kappa$ results

The constant values A and $\sqrt{G_{thr}}$ are listed in Table 8.3. Similar to the $[\pm 45_3]_s$ specimens, little correlation was seen between the constants and similarly damaged/un-damaged specimens or the load level they were tested at. As before, determining sources of error are hard because only one sample was tested at each condition.

Table 8.3. $[\pm 45_2/90_2]_s$ $\Delta\kappa$ Fitting Constants

Specimen Layup	**Load Level** $[\mathbf{P_{max}/F_{ULT}}]$	**Specimen Type**	**Specimen**	**A** $[\mathbf{kJ/m^2}]$	$\mathbf{\Delta\sqrt{G_{thr}}}$ $[\sqrt{\mathbf{J/m^2}}]$
$[\pm 45_2/90_2]_s$	Low [42%]	Baseline	2-1-1	3.4	10.0
$[\pm 45_2/90_2]_s$	Low [42%]	Impact	2-1-7	4.9	12.1
$[\pm 45_2/90_2]_s$	Low [42%]	Compression	2-1-6	7.5	13.6
$[\pm 45_2/90_2]_s$	High [60%]	Baseline	2-1-4	4.5	11.8
$[\pm 45_2/90_2]_s$	High [60%]	Impact	2-1-8	18.2	0.1
$[\pm 45_2/90_2]_s$	High [60%]	Compression	2-1-5	22.7	17.4

8.7 Potential Stored Energy, U

The strain potential stored energy (U) can be calculated using the Griffith energy balance. The parameter, U, is defined in Equation 2.6 and the energy released per cycle, U_{cycle}, is defined in Equation 2.7. Plotting dU/dN or dU_{cycle}/dN provides another possible way to define the energy release rate required for a given crack growth rate. Further, the use of U_{cycle} has also been suggested as a similitude parameter[77, 15, 78]. The average SERR (G^*) can be calculated from Equation 2.8, which is the inverse gradient of the change in U_{cycle} per cycle and crack growth rate plot.

Figure 8.12 and 8.13 show the resultant graphs for each specimen type. Very good alignment of data is seen for both layup types. The potential energy per cycle was fit with a power law curve fit, hence the perfectly straight lines in each case. This was required due to chatter in the calculated U, making its derivative unhelpful. Very high coefficients of determination were found in each case.

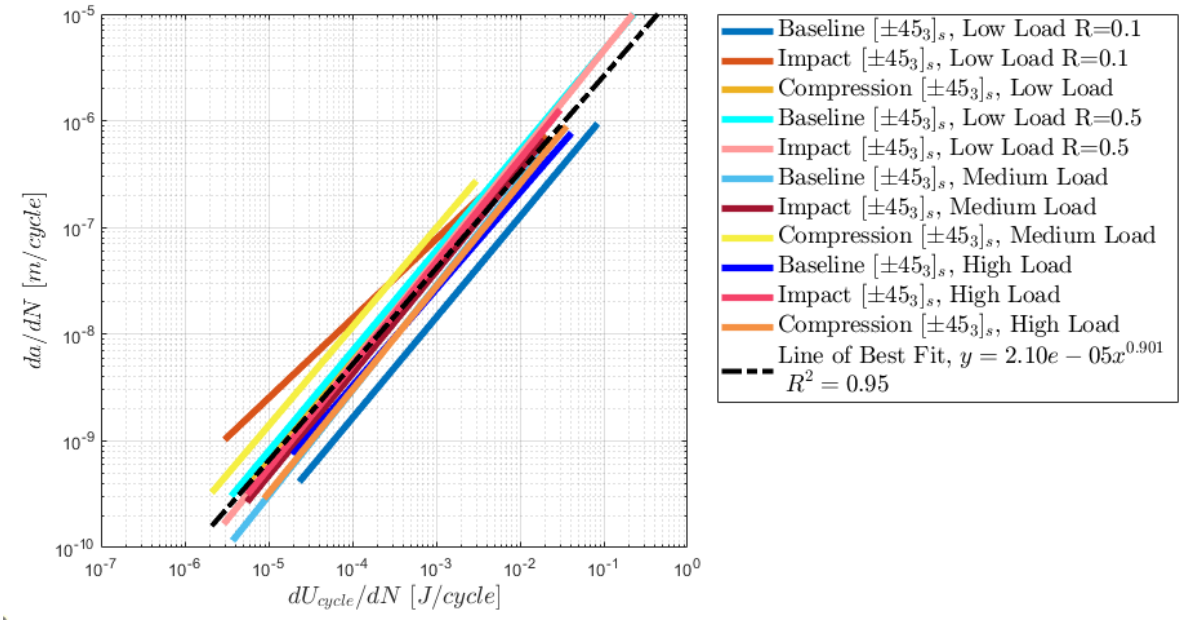

Figure 8.12. $[\pm 45_3]_s$ dU_{cycle}/dN results

Figure 8.12 shows that the resultant line of best fit has a R^2 value of 0.95 across all eleven $[\pm 45_3]_s$ test specimens, which shows that generally all specimens conflate to a single line.

The trend in general shows that a small change in energy relates to a small crack growth rate, and a large change in energy is required for a large crack growth rate.

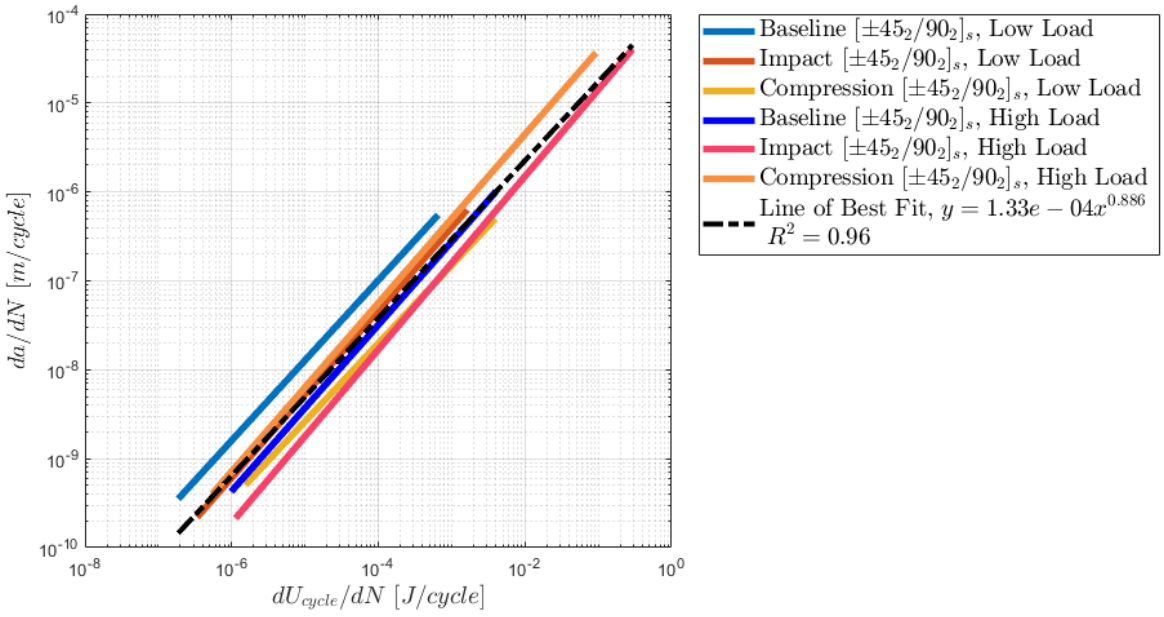

Figure 8.13. $[\pm 45_2/90_2]_s$ dU_{cycle}/dN results

A similar convergence of data points is seen for the $[\pm 45_2/90_2]_s$ layup, where the line of best fit has similarly been calculated with a high coefficient of determination of 0.96. The resultant line of best fit shows a higher crack growth rate for the same applied energy than the $[\pm 45_3]_s$ layup by approximately one order of magnitude, which is consistent with the G SERR method.

Line of best fits were also calculated for individual damage types, being the baseline, impact and compression damaged samples, i.e. the mean line of best fit across all specimens of a damage type. These are shown in Figure 8.14a and 8.14b for each layup. Sub-figure a) shows that for a low applied energy (taken to be $dU_{cycle}/dN = 10^{-4}$), the Impact specimen will grow 4x faster, whilst the Compression sample grows 10x faster. This is a significant change in crack growth rate, however it aligns to what would be intuitively expected from a pre-damaged specimen.

The same relationship is however not seen in the $[\pm 45_2/90_2]_s$ layup, which shows a decrease in crack growth rate in the damaged specimens. This is not as expected but it does align well with the SERR data seen in Figure 8.9.

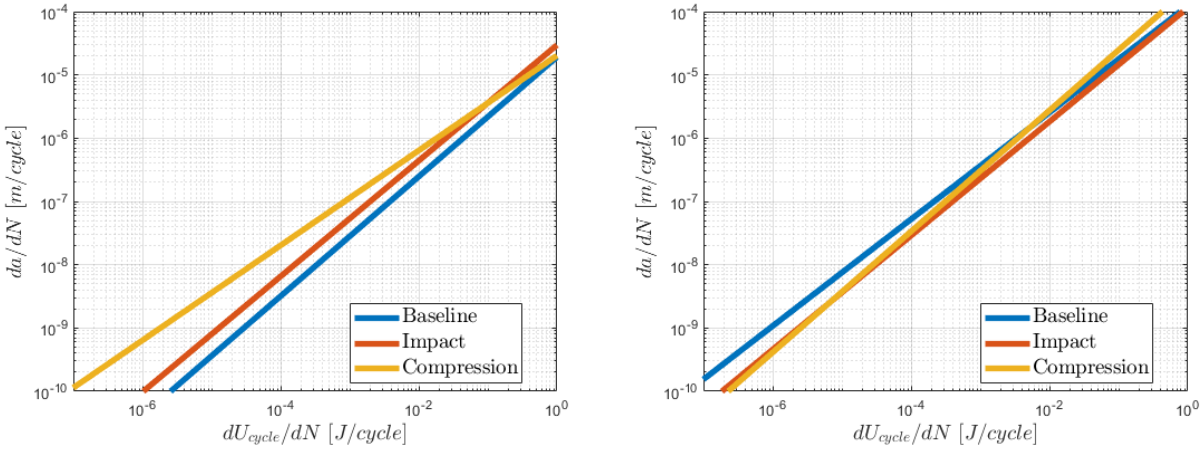

(a) $[\pm 45_3]_s$ (b) $[\pm 45_2/90_2]_s$

Figure 8.14. Change in U_{cycle} per cycle vs crack growth rate for different specimen types

Table 8.4 shows the resultant average strain energy release rate per cycle, G^*, for the fatigue tests as defined by Equation 2.8. G^* is the inverse gradient of the change in potential stored energy per cycle and the crack growth rate line of best fit.

Table 8.4. Fatigue Average Strain Energy Release Rates

Specimen Layup	**Specimen Type**	$\mathbf{G^*_{fatigue}}$ **[MJ/m²]**
$[\pm 45_3]_s$	Baseline	24.327
$[\pm 45_3]_s$	Impact	15.780
$[\pm 45_3]_s$	Compression	23.123
$[\pm 45_2/90_2]_s$	Baseline	3.768
$[\pm 45_2/90_2]_s$	Impact	4.049
$[\pm 45_2/90_2]_s$	Compression	2.085

The $[\pm 45_3]_s$ specimens have a significantly increased average SERR (G^*) as compared to the alternate specimen layup (by ~3-5 times). This is consistent with the extra energy

required to propagate cracks in the other forms of the SERR (G_{max}, $\Delta\sqrt{G}$) in the $[\pm 45_3]_s$ specimen over the $[\pm 45_2/90_2]_s$ specimen.

In the $[\pm 45_3]_s$ layup the Baseline requires the most energy for fatigue crack, followed closely by the Compression samples. There is a significant reduction in energy required for the Impact specimen. The $[\pm 45_2/90_2]_s$ layup has an alternate trend, with the Baseline and Impact specimens having very similar energy requirements, and the Compression sample requiring about two times less for fatigue crack growth.

9. MICROSCOPY

This chapter will review the results of microscopy that occurred on the cross-sections of fatigue specimens after testing. The process of attaining such images will also be briefly discussed.

9.1 Process

The specimens that were analysed through microscopy were sectioned in two manners, either at the lead crack which generally aligned with the notch tip (Section-A) or at the impact site in order to look for delamination growth (Section-B). Refer to Figure 3.4.

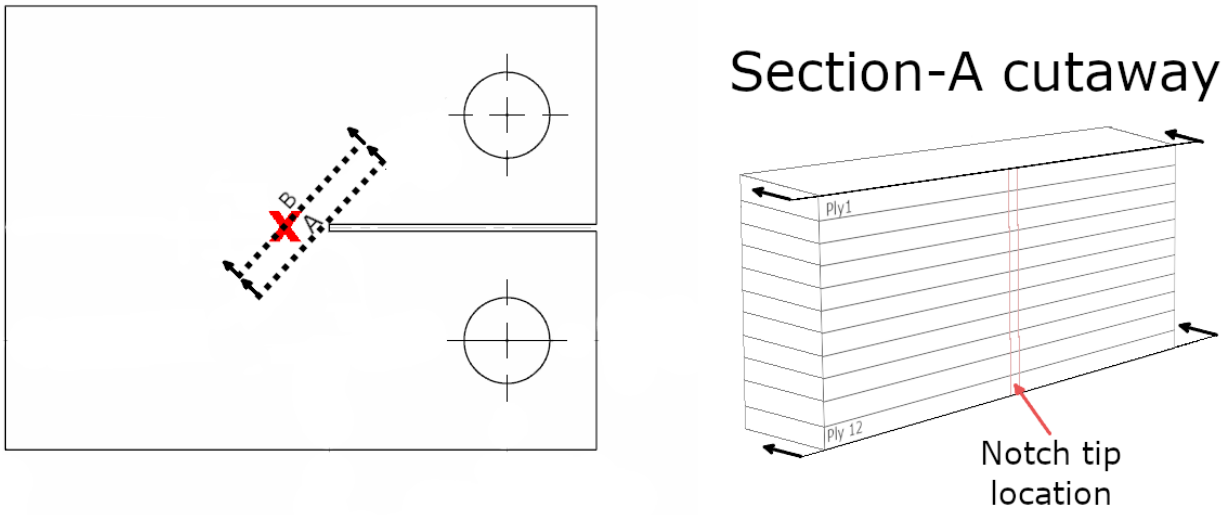

Figure 9.1. Specimen section and microscopy locations

The following is an overview of the process used to polish the specimens and attain the images found in this chapter (and Chapter 5, 6). Overall the process was relatively easy to achieve an excellent polish and high quality microscopy images. Conversely, polishing to an exact cross-section without a notch tip reference point was very difficult and time consuming (impact specimens).

The following process was used:

1. Draw approximate cut lines on the tested specimen with a paint-pen. The cut parallel to the lead crack should be at least 5mm away from the lead crack to ensure no damage from cutting occurs to the face of interest.

2. Cut specimens along cut lines using dremel with cutting disk installed.

3. Mount specimen in epoxy or acrylic cylindrical specimen holders per the manufacturers instructions.

4. Using the grinding/polishing machine (Beuhler PlanarMet 300) follow the steps in Table 9.1.

Table 9.1. Polishing Procedure

Polishing material	**Grit**	**Force**	**Time**	**Comment**
Water	180	Hand-held	As required	Remove material until within 2mm of object of interest
Water	400	5N	As required	(Optional) Until within 1mm
Water	800	2-3N	As required (<3min)	Until within 0.5mm
Water	1200	1-2N	As required (5-10min)	Until within 20-100μm
Clean - Use ultrasonic cleaner (in beaker with 1:1 ratio of distilled water/Isopropyl)				
5μm alumina w/ distilled water	Napad	1N	2-5mins	Be aware very little material will be removed. Repeat 1200 grit and cleaning step as required
Clean - Use ultrasonic cleaner (in beaker with 1:1 ratio of distilled water/Isopropyl)				
0.05μm alumina w/ distilled water	Napad	1N	2-5mins	Final step
Clean - Use ultrasonic cleaner (in beaker with 1:1 ratio of distilled water/Isopropyl)				

9.1.1 Specimens

In total twelve specimens were examined by sectioning and microscopy. The Baseline and Compression samples were examined at the notch tip, adjusted slightly to attain the location of the lead crack within an error bound of $\pm 50\mu m$. Impact specimens were examined at the

at the cross-section of the impact site to the best of the author's ability, though this proved very difficult. Table 9.2 lists the specimens that underwent microscopy of the layup.

Table 9.2. Specimens Sectioned For Microscopy

Specimen Layup	Specimen Type	Specimen	Cross-section location
$[\pm 45_3]_s$	Baseline	1-1-11	A
$[\pm 45_3]_s$	Baseline	1-1-8	A
$[\pm 45_3]_s$	Baseline	1-2-4	A
$[\pm 45_3]_s$	Baseline	1-2-7	A
$[\pm 45_3]_s$	Impact	1-1-3	B
$[\pm 45_3]_s$	Impact	1-2-6	B
$[\pm 45_3]_s$	Impact	1-1-6	B
$[\pm 45_3]_s$	Compression	1-1-12	A
$[\pm 45_3]_s$	Compression	1-2-5	A
$[\pm 45_3]_s$	Compression	1-1-2	A
$[\pm 45_2/90_2]_s$	Baseline	2-1-1	A
$[\pm 45_2/90_2]_s$	Impact	2-1-7	B
$[\pm 45_2/90_2]_s$	Compression	2-1-6	A

9.2 Baseline Specimens

Four $[\pm 45_3]_s$ baseline specimens were examined under microscope after being sectioned as per Section-A of Figure 9.1 using 20x stitched images. A single $[\pm 45_2/90_2]_s$ specimen was also examined at the same cross-section.

The polishing occurred at a $+45°$ angle as per the cross-section specified in Figure 6.4. As the lead crack was located at the tip of the notch for Baseline specimens, the notch tip was used as a gauge for locating the lead crack which is otherwise not possible from the cross-section of the material. In each of the Baseline specimens the approximate section of the lead crack was achieved however it must be noted that the cross-section location is not perfect. The cross-sections are likely accurate within $50\mu m$ of the notch tip location, 5-10 degrees of perpendicular to the lead crack, and 5-10 degrees of parallel to the lead crack. This means the microscopy images as showed in this section, or those used for quantitative damage analysis later on, are only accurate for the cross section they are at.

Figure 9.3 shows a microscopy image of the lead crack of Specimen 1-2-7, the only specimen to reach failure - occurring after 15.7 million cycles. The crack was 10.6mm before fracture and 16mm in the image (after failure). The image was made from stitched 20x microscopy images. The crack can be seen to grow in a relatively straight line from the end of the notch tip, parallel to the fibre direction in the outer ply. This is consistent with the lead cracks seen in every specimen. The figure also shows a crack growing from the notch tip in the -45° (opposite) direction.

The lead crack as visible from the surface was seen to favour growth parallel to fibres, however at intervals it would jump across or go under fibres but remaining generally aligned to the bulk of the surface fibres. The crack often crossed fibres before or after discontinuities in the surface breaking fibres from things such as unaligned fibres or surface defects.

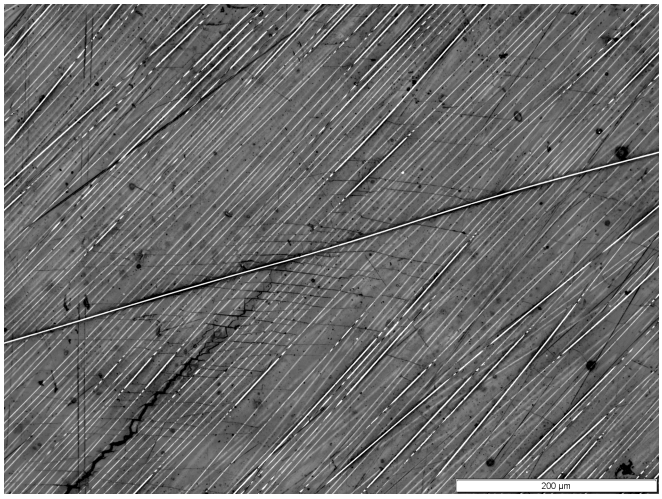

Figure 9.2. Specimen 1-2-7 crack tip

Figure 9.2 shows the crack tip of the lead crack on Specimen 1-2-7, seen emanating from the the lower right side of the image. The image was taken during the log-linear crack growth regime at approximately 12 million cycles. The crack is seen to be growing in a jagged manner. This jagged crack growth was typical of crack growth after the initial unstable growth seen in Figure 8.2. Matrix cracking is seen perpendicular to the loading direction, both adjacent to the crack tip and in front of it, implying the crack tip area was highly stressed.

Figure 9.4 shows a stitched 20x microscopy image of the lead crack on Specimen 1-1-11, a $[\pm 45_3]_s$ layup. The lead crack in the image is growing left to right in the image. Multiple damage types including fibre-pull out, intralaminar cracks, delamination and fibre breakage have been found and highlighted for easier identification.

First of note is that a number of what are postulated to be intralaminar crack faces are visible, identified in the light blue colour boxes. These areas are identified by looking for darker regions within the +45° plys (ply 1 and 3 for example), as the fibres have been fractured and are missing after polishing. The darkness is the matrix material in these plys. These damaged areas are postulated to be intralaminar cracks running parallel to these 45° fibres as their existence was only seen at cross-sections aligning to the lead crack, and we would expect the intralaminar crack to have to move through the matrix and across fibres at intervals where it is energetically required to do so, such as across the numerous misaligned fibres within the ply as can be seen in any of the +45° plys in the figure. The figure therefore shows that the lead crack (seen from the surface in ply 1) had coincident intralaminar cracks in plys 3,5 and 10.

A large quantity of intralaminar matrix cracks are also visible in the -45°plys. These cracks are therefore growing perpendicular to the lead crack, which depending on their length could mean the area of damage within the specimen is quite large. These intralaminar cracks were seen in every ply of this specimen in a large quantity. The density of intralaminar cracks was seen to decrease as distance from the notch increased. This is to be expected as the notch is the highest stressed area in the specimen.

Figure 9.3. Specimen 1-2-7 lead crack

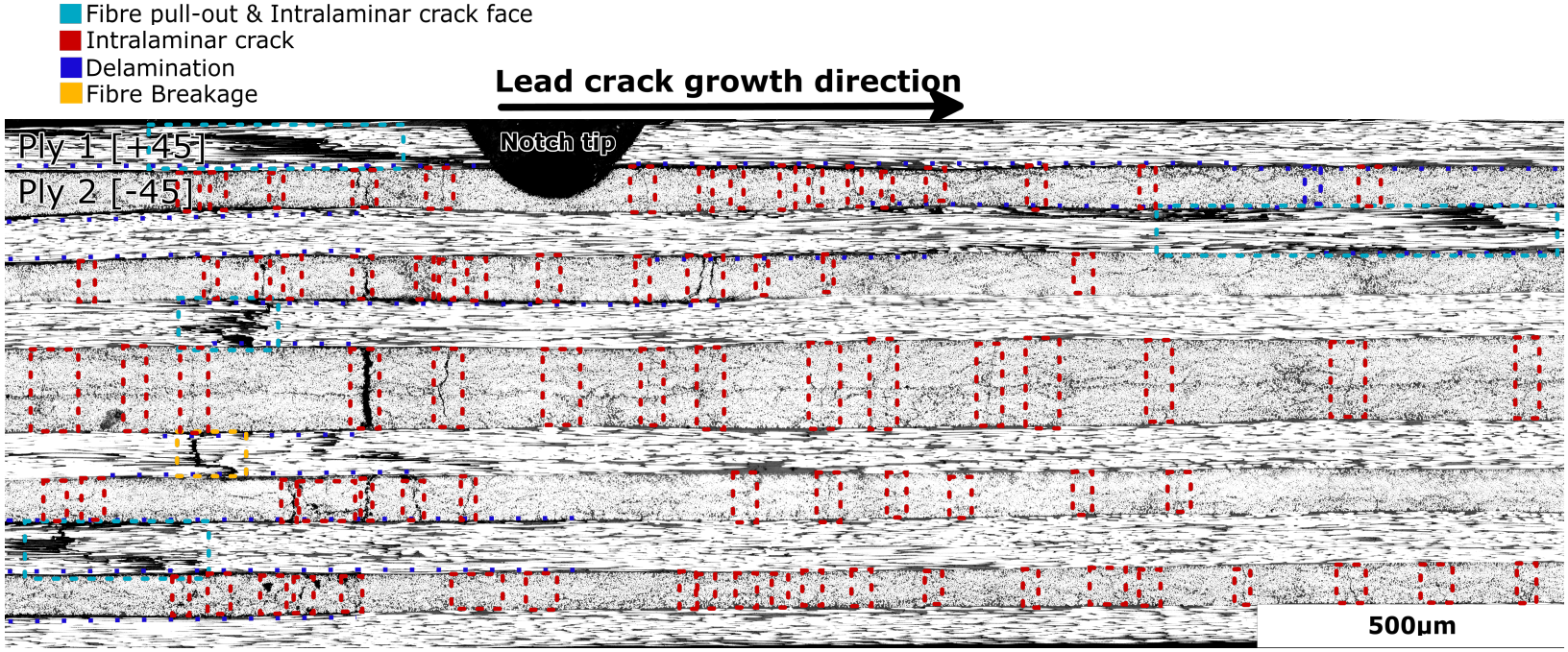

Figure 9.4. $[\pm 45_3]_s$ - Specimen 1-1-11 cross-section microscopy

Delaminations were found by looking for dark areas between plys, or in some cases following the ends of intralaminar cracks as they evolved into delaminations at ply boundaries. In the first scenario, the delamination had caused localised debonding of adjacent plys. In the second case, the damage could be more aptly described as interlaminar cracking, rather than debonding. Figure 9.4 shows that delaminations were following the lead crack, leading to delamination between ply 1-2, 2-3 and 3-4.

Fibre breakage was seen to the left of the notch tip in ply 8, where a ply can be seen to be completely fractured.

Figure 9.5 shows a stitched 20x microscopy image of the lead crack of Specimen 2-1-1 which is a $[\pm 45_2/90_2]_s$ layup. The lead crack in this cases was running right to left in the image. Significantly less overall damage was seen along the lead crack in the $[\pm 45_2/90_2]_s$ layups than the $[\pm 45_3]_s$.

Directly adjacent to the notch in ply-1, fibre-pull out and an intralaminar crack face is visible, highlighted by the light blue box. The box highlights the dark matrix visible after fibres have pulled out of the material after the lead crack has passed through them. No other parallel crack faces are seen in deeper plys.

Intralaminar cracks passing through the lead crack cross-section are seen in both the -45° and 90° plys. The intralaminar cracks in the -45° plys stop at the ply boundaries but in some cases evolve into small delaminations or interlaminar cracks. The intralaminar cracks in the 90° plys pass through the entire stack of four 90° plys, as was seen in every instance of intralaminar cracks growing through the centre -45° plys in the $[\pm 45_3]_s$ material. The centre 90° ply cracks terminate in all cases at the ply interface with the neighbouring -45° plys.

Delaminations are also seen to be following the growth of the lead crack in the outer plys, between ply 1-2 and 11-12. No fibre breakage events were seen.

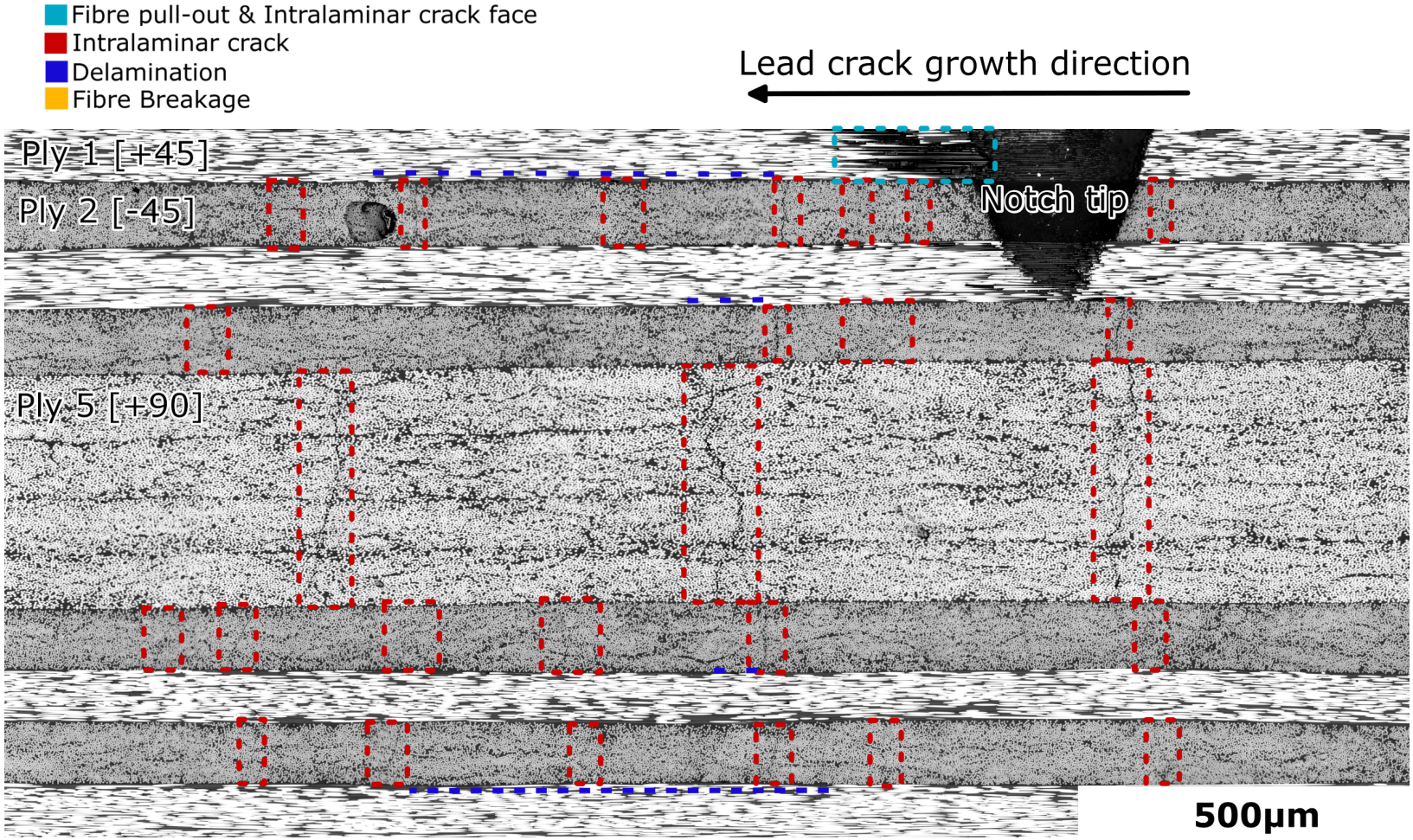

Figure 9.5. $[\pm 45_2/90_2]_s$ - Specimen 2-1-1 cross-section microscopy

9.3 Impact Fatigue Specimens

Four impact specimens were examined by sectioning the specimen at a distance of 5-10mm from Section-B, as per Figure 6.4, and polishing up to the impact site. This took a long time as polishing as the impact site was visible after it was mounted in epoxy. Blue tape was applied to just before the impact area at the surface, in order allow some understanding of the distance to the impact site. In all cases multiple polishing attempts was required.

Figure 9.6 shows intralaminar cracking growing on the surface of Specimen 1-1-6 away from the impact location. This intralaminar surface crack growth was seen in every Impact test, both for fatigue and monotonic tension. In each case, the cracks grew from the approximate centre of the impact in one or two directions, parallel to the ply fibre direction. The cracks that grew from the impact zone were never found to be the lead crack, the lead crack continued to be the crack that grew from the notch tip in the ±45 direction.

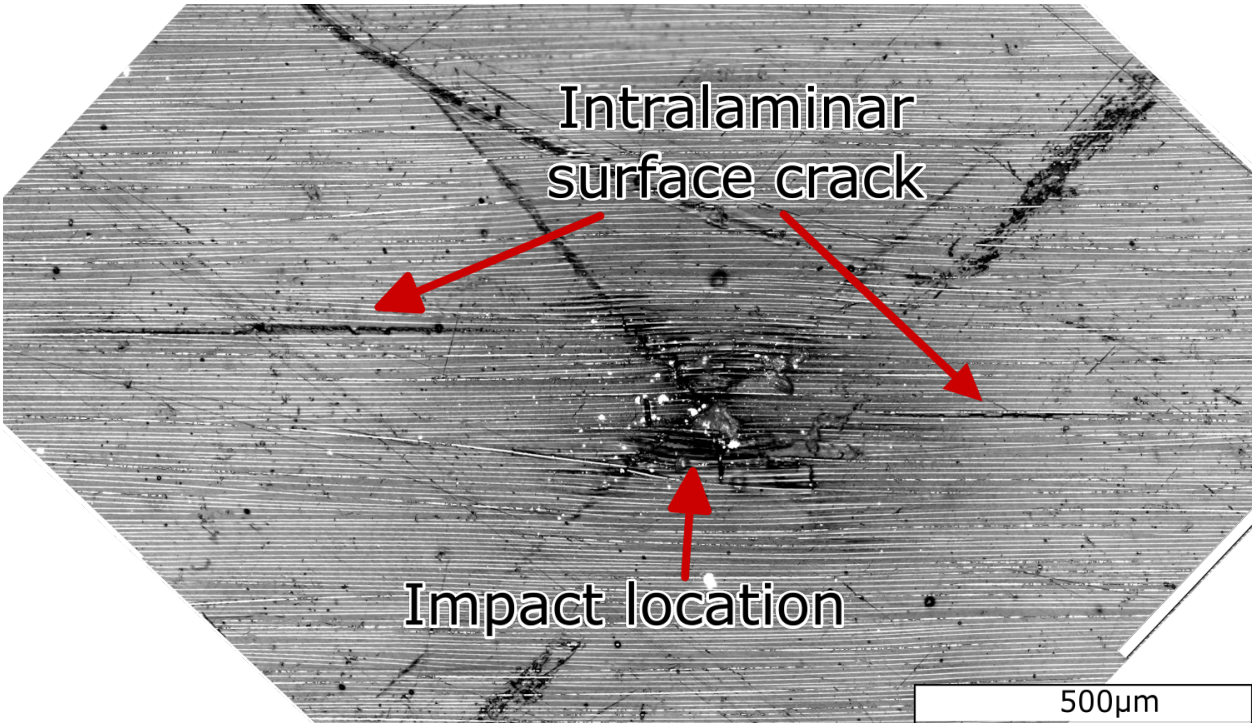

Figure 9.6. Fatigue crack growth from Impact site - Specimen 1-1-6

The sectioning of the impact specimens always required polishing through the lead crack site and therefore this information was lost. The analysis of sub-surface damage at the

impact site was difficult, and the exact centre of the impact location was much harder to find. Of the cross-sections done, only one of four was seen to have a delamination between ply 1-2. Based on the consistency of occurrence of delaminations from the initial tests (Chapter 5) this was more a factor of not being at the right cross-section that the delamination not being present.

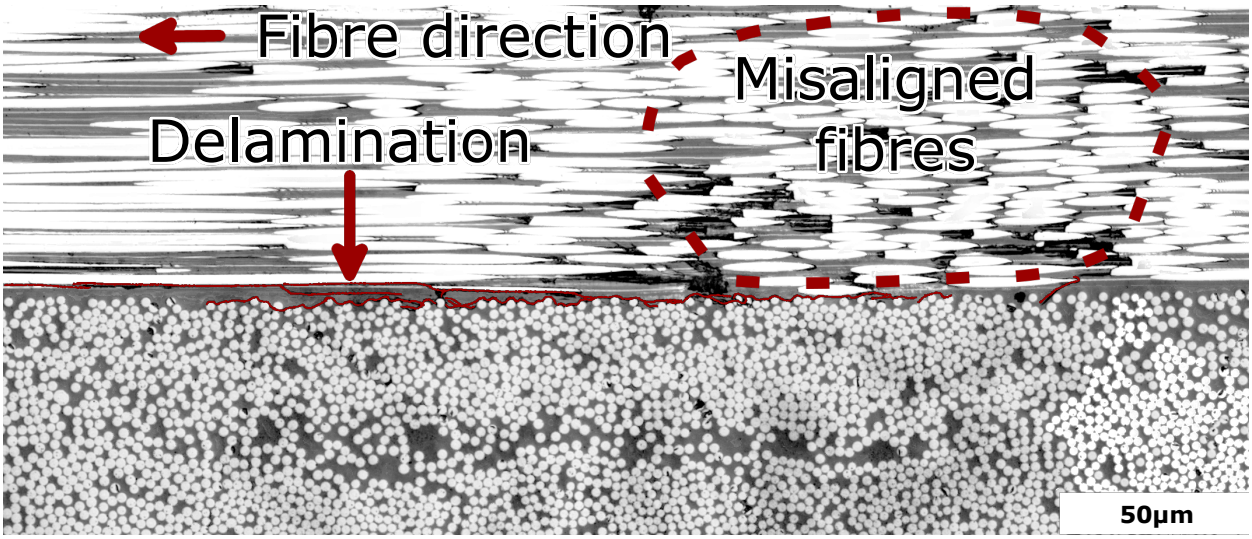

Figure 9.7. Delamination under impact damage - Specimen 1-1-6

The delamination was found on Specimen 1-1-6 (Figure 9.7), a high-load $[\pm 45_3]_s$ specimen. It was approximately $600\mu m$ in length at the cross-section it was found which shows the delamination had not grown significantly since the delamination was initiated quasi-statically by micro-indenter. The fibre pattern seen in the top ply of Figure 9.7 shows either bulk misalignment of fibres or that the fibres have shifted direction under indenter loading. The cross-section is not considered to be at the centre of the impact based on the lack of fibre breakages or matrix damage seen.

Figure 9.8 was a microscopy image taken at the cross-section of the indent. Analysis of the image showed no delamination at the outer plys, however it did show that a significant intralaminar crack was growing through all the 90° plys. This intralaminar crack is assumed to have initiated and grown from the notch tip as it is the most high stressed area, and Figure 9.5 verifies that a number of intralaminar cracks are present at the notch location. This is an interesting discovery as the intralaminar middle-ply crack must have grown at

least 5mm from the notch, making it longer than lead crack that was seen growing on the outer plys.

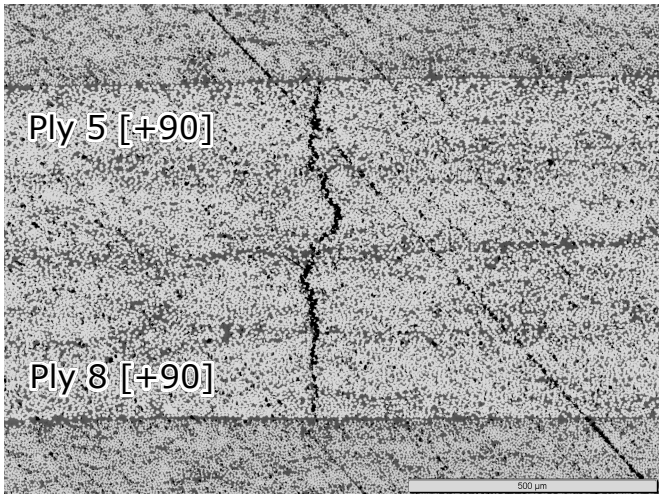

Figure 9.8. Intralaminar crack on ply 5-8 under Impact location - Specimen 2-1-7

9.4 Compression Fatigue Specimens

Compression specimens were seen to have the lead crack grow from the far edge of the compression damage/ply buckling in all cases, i.e. the far side of the buckling damage from the notch tip. This is seen in Figure 9.9 which shows the surface view of the lead crack on the lower part of the image, growing from right to left. Once propagated, the cracks grew in the same way as the Baseline and Impact specimens as seen form the surface.

Figure 9.9. Lead crack emanating from buckled ply - Specimen 1-1-2

Sub-surface damage can be seen in Figures 6.5 and 6.6 from Chapter 6 and these figures are not repeated here, noting the images were taken after approximately one million cycles each.

Figure 6.5 showed how the kink band formation in ply-1 lead to interlaminar separation/crack growth, which connected to delamination at ply 1-2 boundary. This delamination is adjacent to a number of other delaminations in the middle plys growing in the lead crack direction. Intralaminar cracks also have formed in the -45° plys, with a higher density than the Baseline specimens, particularly within the middle plys (ply 6 and 7). Many ply thickness fibre-breakage events are visible however as described in Chapter 6, these are likely from the initial compression event.

Figure 6.6 shows an image of Specimen 2-1-6 after an initial compression load and approximately one million cycles. As seen in the Baseline samples, damage quantity is significantly reduced in the $[\pm 45_2/90_2]_s$ specimens compared to the $[\pm 45_3]_s$ layup. Intralaminar cracks are seen in all the plys but in smaller quantities. A large intralaminar crack in plys 5-8 is also visible; in the same way it was seen in the Baseline and Impact specimens.

9.5 Failed Specimen

Figure 9.10 looks at the cross-section of Specimen 1-2-7, a baseline specimen, which was the only specimen to reach failure (after 15.7million cycles). Primarily the major difference between this cross-section and the Baseline specimens previously reviewed is the large increase in intralaminar crack density in -45° plys and the significant amount of delamination growth that accompanies the lead crack (which is growing left to right).

Large amount of delaminations are seen on every ply boundary, which shows the importance of understanding delamination in CFRP damage tolerant structure. Delamination growth is seen to be periodic (stops and starts) on a number of ply boundaries (1-2, 2-3, 3-4 in particular). Full length delaminations are seen on the boundary of ply 5-6. It is possible that the partial intermittent delaminations seen on ply boundaries 1-2, 2-3, 3-4 are actually full image length delaminations, but it is just not seen at this particular cross-section. This is verified for the delamination on ply 1-2 and 2-3 as the delamination was seen to be constant at other cross-sections ($-20\mu m$ of cross-section seen in Figure 9.10).

Particularly interesting is that there are a number of delamination ply-crossover events occurring, where a delamination evolves into a intralaminar crack and crosses to the other

side of a ply, where it continues to grow as a delamination. This is seen twice on ply-4 and twice on ply-11.

Not pictured is further images along the length of the lead crack which shows that the delamination of ply boundary 1-2 and 11-12 travels approximately 8mm in total length. Fracture occurred on Specimen 1-2-7 at ~10.60mm for reference.

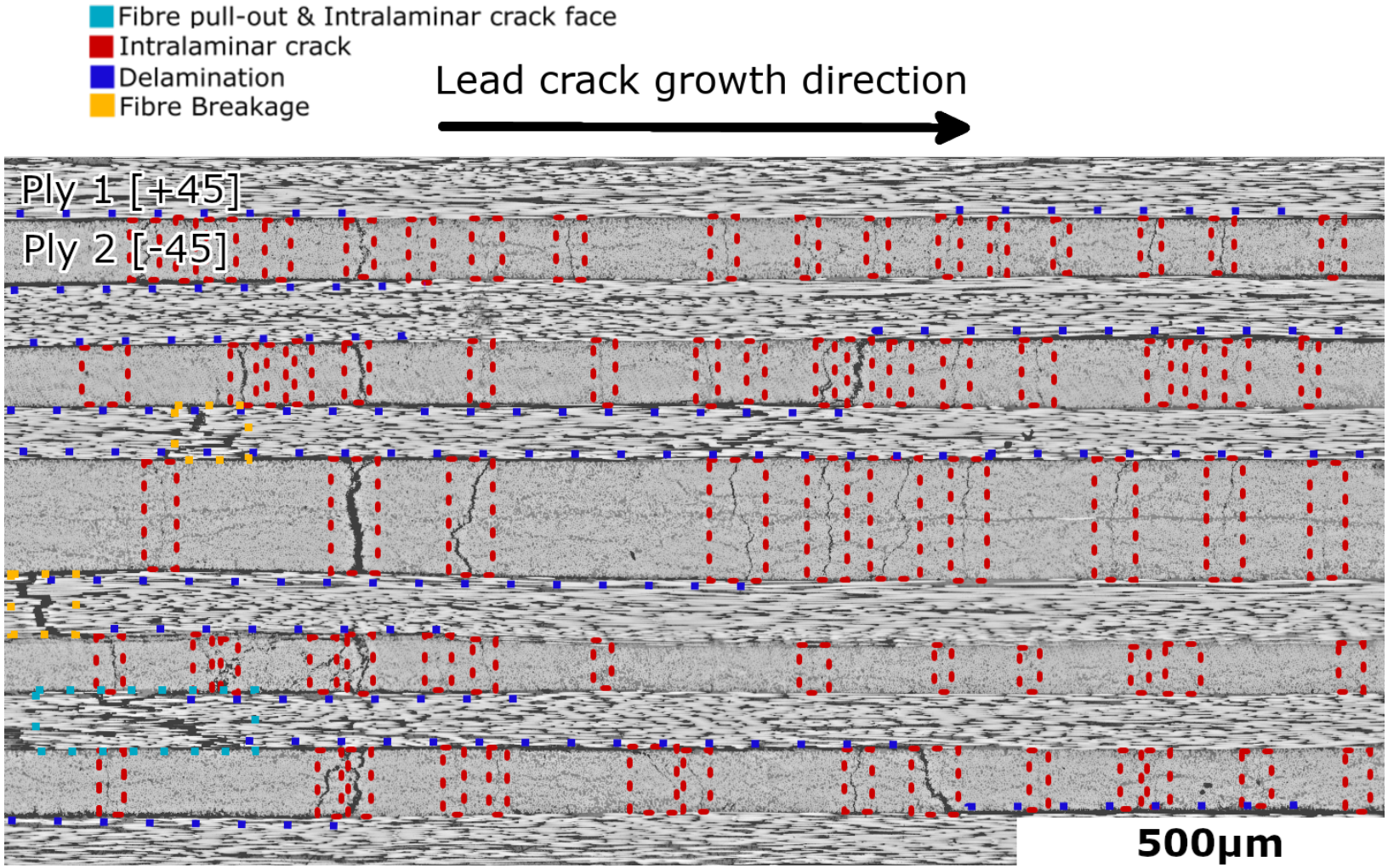

Figure 9.10. Cross-section microscopy of failed specimen - Specimen 1-2-7

9.6 Damage Quantification

Damage was quantified in the six $[\pm 45_3]_s$ sectioned layups that underwent one million cycles. Two types of damage were analysed; intralaminar cracking and delamination length. To be consistent, all damage within 12 ply thicknesses, or 1 thickness of the laminate, of the notch-tip location in the lead crack direction was counted.

Intralaminar cracks were quantified separately on each ply in which they occurred. As the specimens were created to be symmetrical and the loading constant across the thickness of the specimen, the damage would be expected to be the same in each of the symmetric plys, being plys 1 and 12, 2 and 11, 3 and 10, 4 and 9, 5 and 8, 6 and 7. The damage in symmetric plys were therefore added together to provide a more succinct count of the damage.

Delamination was measured in length within the same region as above at each ply-ply interface. It was then divided by the width of a ply in order to provide a non-dimensional count of the delamination length.

Figure 9.11 shows the count of intralaminar cracks in each of the six $[\pm 45_3]_s$ specimens analysed, in each of the plys, however all $[\pm 45_3]_s$ specimens are listed. Note that the Impact specimens were not able to be quantified as no sectioning occurred at the lead crack location. No trend is visible in the quantity of cracks occurring in each individual ply relative to each other. The quantity of intralaminar cracks on each specimen was approximately equal, if not slightly decreasing at the higher mean loads. This is examined further in Chapter 10.

The total amount of intralaminar cracks within the -45° plys along the lead crack exceeded 20 in all specimens but reached as high as 29 in the low load (R=0.1) compression specimen.

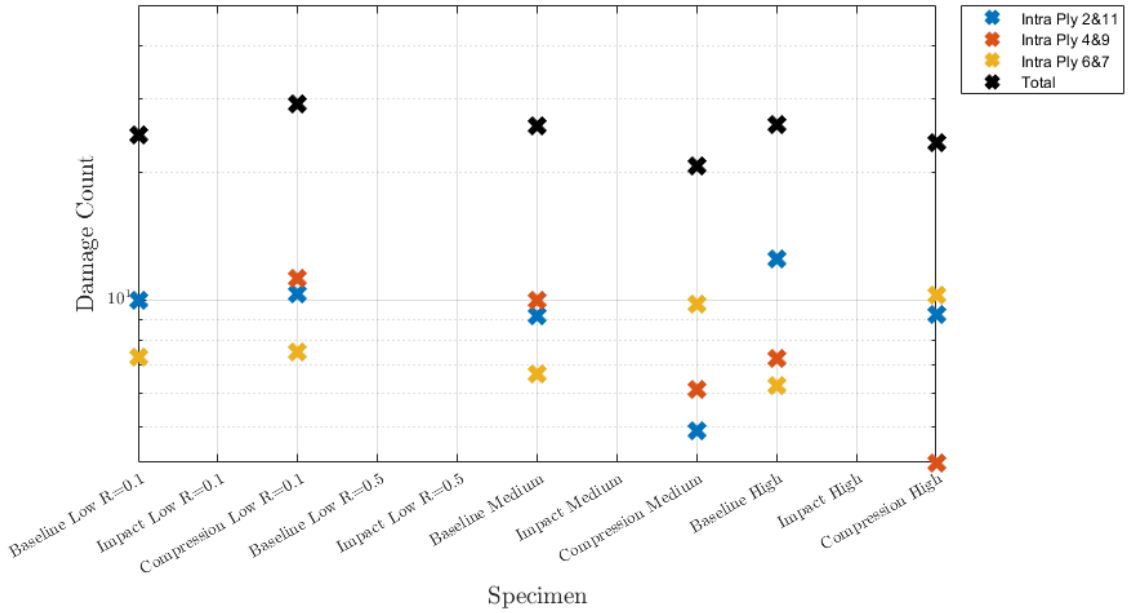

Figure 9.11. Intralaminar crack count by specimen

Figure 9.12 shows the non-dimensional delamination length in each of the $[\pm 45_3]_s$ specimens at each interface.

In general, the middle plys had less delamination than plys closer to the surface however the outer plys did not necessarily have the highest amounts of delamination. No delaminations were found on any specimen on the interface of ply 6-7, the joined -45° plys.

The overall sum of delamination length (black) across all ply boundaries shows no obvious trend. Baseline specimens had lower delamination lengths than compression specimens in two cases, but not in the third. Higher loaded specimens also did not necessarily have the largest quantity of delaminations, with the Compression damaged medium loaded specimen having the largest quantity. Significant amounts of delamination were in each specimen, with the minimum length being 11 ply thickness lengths.

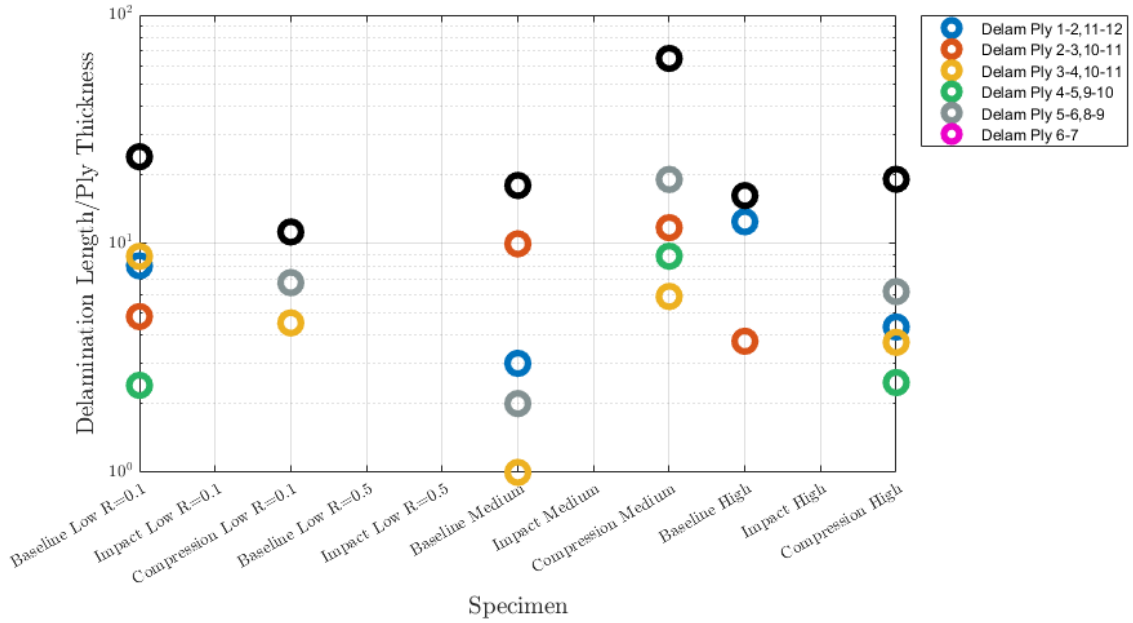

Figure 9.12. Delamination length by specimen

Figure 9.13 shows the mean damage count of each type of specimen, being Baseline or Compression, as Impact specimens were not assessed in the same way. For intralaminar crack quantity (sub-figure a), due to the standard deviations being large there seems to be no direct connection between specimen type and intralaminar crack quantity.

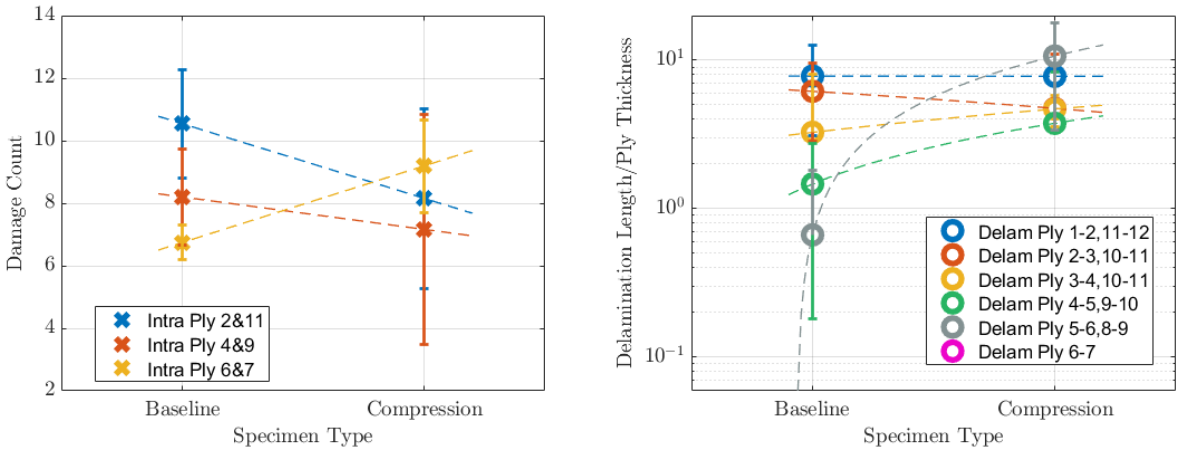

(a) Intralaminar cracks

(b) Delaminations

Figure 9.13. Mean damage quantity by specimen type

Figure 9.13b shows the mean delamination length by specimen type. It shows that there is relatively consistent damage in each specimen type on the outer plys however the inner ply boundaries show greatly increased delamination lengths over the Baseline specimens. The length increase in these ply 5-6 and 8-9, is approximately 1400% for example in the Compression specimens over the Baseline.

Further, the relation between loading level, or mean stress, was examined to see if a correlation existed between damage formation. As can be seen in Figure 9.14, there is significant scatter for both Intralaminar crack quantity and delamination length, making the correlation most likely insignificant.

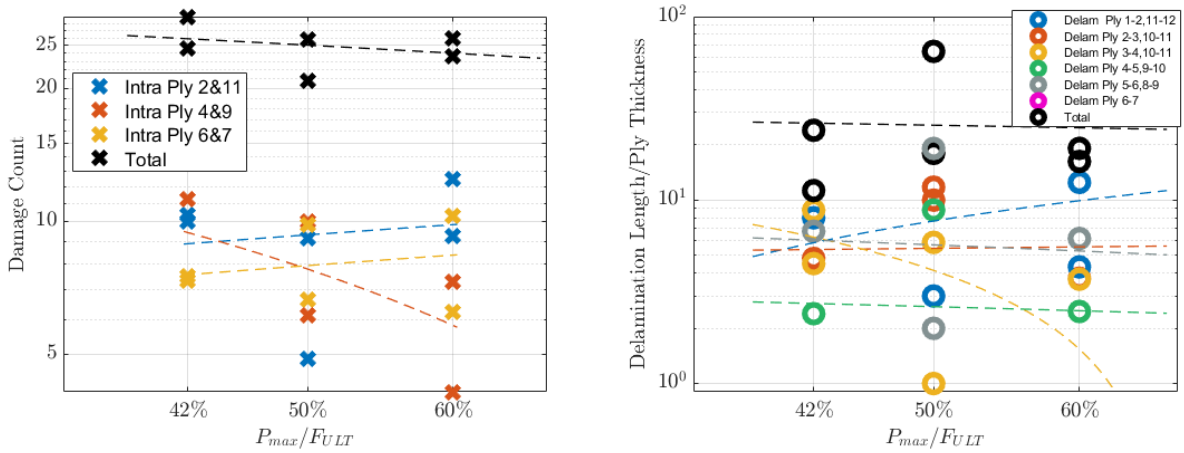

(a) Intralaminar cracks

(b) Delamination

Figure 9.14. Max fatigue load vs damage

10. DISCUSSION

Aerospace composite materials generally consist of multiple uni-axial plys stacked together in multiple directions, called laminates. Due to the strength of fibres within each ply being along the fibres axis, plys are aligned within a laminate to take predominately tensile loading. It is however possible that the laminate, or individual plys, are subjected to non-tensile loads, either in-plane or out-of-plane. These loads can be from numerous external events such as impact damage from foreign objects or unforeseen out-of-plane loads.

These compression and impact loads predominately lead to the initiation of delamination within the layup [4]. As seen in Chapter 5 and 6, both loads led to significant amounts of damage including large delaminations. The Impact specimens were created through the application of a $50kg \cdot f$ force to the outer plys, 5mm from the notch tip. This created an approximately $600\mu m$ delamination on two faces of the specimen approximately 5mm from the front of the notch-tip, within the highly stressed area. The Compression specimen used a single elastic compression load until the proportional limit was reached, creating kink-bands on the outer plys, and significant fibre-breakage and intralaminar cracks on internal plys.

Since the FAA issued guidance on the use of slow-growth and damage tolerant lifing of aircraft composite primary structure in 2009 [5], significant work on finding a similitude parameter for composite materials, allowing for the prediction of damage growth rates in the specified material independant of the part's thickness, initial crack length and layup.

The majority of tests analysing fatigue crack growth in composite materials look at double cantilever beam (DCB) specimens in order to understand the rate at which delamination grows under cyclic loading [19, 13, 28, 23, 79, 80, 29]. Whilst delaminations tend to be more prevalent than other damage types and potentially more detrimental to aircraft structural integrity [81], they are not the only damage to exist within a fatigue loaded CFRP. In fact, numerous damage mechanisms can be present within a layup, in some cases competing to grow damage within the part. These mechanisms and this interaction is highlighted well by Hanhan et al. [34], where the interaction of delaminations and intralaminar crack growth created fluctuating crack growth rates within multiple plys. In other work, debate

is occurring about whether delamination actually leads to laminate failure, or whether it is fibre failures from delamination stress concentrations that lead to failure [27].

DCB specimens are typically used as they offer an easy way to measures Mode I delamination growth. It is however a 1D measure of how damage grows in a material and does not necessarily take into account multi-directional interfaces or more than one delamination being present [27], nor account for the intrinsic connection between intralaminar and interlaminar crack growth [29, 22, 30]. This is especially relevant when it has been shown that CFRPs can have negligible difference in intralaminar and interlaminar fracture toughness[24]. Further, most fatigue crack growth experiments are on uni-directional composites whilst the majority of composite materials used in real aerospace applications are multi-directional [82, 83, 27], leading to an under-supply of fatigue crack growth data to make design decisions in multi-directional layups [83]. These issues have led for some authors to question whether the similitude parameters measured from DCBs are appropriate for more complex specimen geometries and stress states[82, 23, 27].

The use of compact tension (CT) specimens in this research aimed to partially fulfill the requirement for using a more complex stress state and layup to the analysis of fatigue damage growth in CFRP laminates. This should have the affect of assessing the IM7/5320 laminate in Mode I whilst allowing the damage to progress as is energetically viable for the loading and material. CT specimens have been used in a a multitude of other studies into fatigue in composite materials[43, 58, 31, 34, 69] however most have been limited to quasi-static fracture toughness investigations or limited sample size.

10.1 Monotonic Tension

The monotonic tension tests carried out in this work saw that the Baseline specimens had a higher ultimate failure load than the damaged impact and compression specimens as should be expected. In both layups, the Impact specimen had similar performance to the Baseline specimen, with approximately identical Young's modulus values. Cracking was initiated from the Impact site in each case, however the overall strength was similar to the undamaged specimen, with the damage being too far from the notch tip and the material

too damage tolerant to make much of a difference to overall material performance. The Compression specimens however had decreased values of Young's modulus and decreased ultimate loads owing to the severe damage created subsurface in the specimens, with the outer two plys of the layup having partially buckled plys in the most high stressed region of the specimen. The outer ply buckling and internal damage caused the lead crack to shift from the notch tip to the opposite side of the buckling damage as seen in Figure 9.9.

Regardless of the change of lead crack location, yield point or ultimate load, it was shown that within a reasonable degree of accuracy, the critical strain energy release rate (G_{IC}) was the same for both the Baseline and damaged specimen types (Table 7.2). Indeed it was also shown that the difference in critical SERR was very similar between each layup type, with the Baseline specimens in each layup type having a difference in G_{IC} of just $0.001 MJ/m^2$. This may be because critical SERR is heavily dependent on matrix material properties[84] which were the same in both layups. From Ortiz-morales et al.[31] who looked at a similar material in CT specimens, some fibre bridging is expected to have occurred on the centre -45° plys, and even between ±45° plys where delamination is present however to a significantly reduced degree than expected in DCB specimens, and therefore significant error caused by fibre bridging is not likely. Czabaj et al.[24] did however find that the their intralaminar fracture toughness calculations may have been affected by fibre bridging in the 90° plys which would only affect the $[\pm 45_2/90_2]_s$ layup in this study, in which they saw fluctuations of ~4% in $G_{IC-Intra}$. This may account for the increased variability that was seen in the $[\pm 45_2/90_2]_s$ fracture toughness values in Table 7.2 over the alternate layup.

A larger difference was seen between layup types when the mode I stress intensity factor (SIF) was reviewed, showing a critical SIF difference of $\sim 16 MPa\sqrt{m}$, though this may be because of inaccuracies in the use of Equation 7.3 due to the specimen being under minimum thickness as per the ASTM Standard [51].

Analysis of the monotonic tests through the area rule to find the change in potential energy, dU, show that regardless of layup the Compression specimen has a much large crack extension (da) than the Baseline and Impact specimens for the same energy (Figure 7.6), which is expected due to the extent of damage sub-surface within the specimens. The inverse

of the gradient divided by the thickness was taken to be the average SERR, G^* (Equation 2.8, per Amaral et al. [26]).

10.2 Fatigue Testing

This section will look specifically at the fatigue loaded specimens.

10.2.1 Strain Energy Release Rate, G

Under fatigue loading for low, medium and high loading levels, the SERR was measured across 17 specimens. Significant scatter was seen across both SERR parameters measured, G_{max} and $\Delta\sqrt{G}$, across both layup types as seen in Figures 8.4, 8.5, 8.6 and 8.7. It is known from literature that both of these parameters are not similitude parameters in their own right due to dependencies on R-ratio, delamination length and thickness[13, 14, 15, 16, 17, 18, 19]. In this work it was seen that a lot of scatter was present within the material, with the SERR variation for a constant crack growth rate varying by an order of magnitude across the most and least damage tolerant specimens tested in all cases except for $\Delta\sqrt{G}$ in the $[\pm 45_2/90_2]_s$ layups where a 2.5x scatter across the most and least damage tolerant specimens was seen.

Based on our intuitive understanding of damaged materials, it was hoped to see a delineation in damage tolerance across damaged and undamaged specimens, with lower SERRs required for damaged specimens than undamaged specimens for the same crack growth rate. This trend was visible at two load levels during fatigue cycling (Low load, R=0.1 - Figures 8.8a, and Medium load - 8.8c) but not in the remainder of the $[\pm 45_3]_s$ tests, and never occurred in the $[\pm 45_2/90_2]_s$ layup tests.

Unfortunately, it is likely that the fatigue results for the $[\pm 45_2/90_2]_s$ specimen are likely invalidated, due to the lead crack being found to be in the middle 90° plys (plys 5-8) rather than being on the surface as expected. This was seen in the microscopy investigation of Specimen 2-1-7 which was loaded at $P_{max} = 42\% \cdot F_{ULT}$. Due to this occurring on the low load test, it is predicted that this likely occurred in all $[\pm 45_2/90_2]_s$ specimens invalidating the SERR results which rely on accurate crack length calculations. The propensity of the lead crack to grow in the middle plys is somewhat expected due to low energy cost of growing

damage parallel to the fibre direction, and perpendicular to the load in Mode I loading. The $[\pm 45_2/90_2]_s$ layup will therefore not further be discussed where reference to crack length or parameters requiring it for measurement are required (G).

Fibre bridging is not expected to have significantly influenced the results of the $[\pm 45_3]_s$ tests. Hanhan et al.[34] investigated similar CT CFRP specimens and found that fibre bridging between $\pm 45°$ plys typically lasted a few cycles at most, causing small fluctuations in crack growth rates and faster intralaminar crack growth than delamination growth, all of which were rectified in a small number of cycles. The sustainment of such fibre bridging effects over the million cycles in each test is therefore unlikely to have largely affected results.

It must be understood that the strain energy release rate, G, is an empirical correlation between crack growth and the energy release from the crack growth, and it does not have an underlying physical theory behind it [25, 27, 26]. Irwin's early work states that G is the result of crack extension not the cause of it. Likewise, whilst the lead crack framework has been shown to be applicable to composite materials [73], it has limitations surrounding in this type of experiment where the lead crack is relied upon to be visible on the surface.

Many studies with DCB based tests have shown consistent results for $\Delta\sqrt{G}$ vs da/dN with comparatively little scatter [13, 23, 21], however it should be noted that only a 1D delamination on a single interface is being assessed. Inherently, the crack extension on a single interface is bound to produce results of less scatter than a more complex layup, geometry and stress state. Results could have also been influenced by the out-of-plane bending issues discussed in Section 4.3.

Reasonably, as SERR is the result of crack growth not the cause of it, it is expected that there will be a visible relationship between damage within the layups tested and the SERR at which they occurred. Investigation of this will show whether the scatter is the result of analysis error or natural material and damage growth scatter.

To investigate this, SERR parameters were plotted against the quantity of intralaminar cracks and delamination within the layup along the lead crack as per Section 9.6. Yao et al.[20] specifically recommends correlation between energy dissipation and the in-situ damage in the composite of interest to validate crack driving force models. A study by Khan et al.[84] has similarly analysed SERR parameters against damage features in DCB specimens.

In this work, the logarithmic mean of $\Delta\sqrt{G}$ for each test was taken as the x-axis value for damage comparison. In reality, the values of this parameter varied across the individual tests, however the mean should provide an estimate of the SERR range the specimen underwent during testing. In Figure 9.13, the mean quantity of intralaminar cracks and delaminations was examined in each specimen type. The results showed that the Baseline and Compression specimens did not have comparable distributions of damage when it came to delaminations. This difference in damage make-up is likely a result of initial damage creation before fatigue testing by compression loading in the Compression specimens, and for this reason Baseline and Compression specimens were examined separately. It must be noted that no overall trend was seen for $\Delta\sqrt{G}$ vs damage count until separated by specimen type.

Figure 10.1 examines the intralaminar damage quantity against the mean value of $\Delta\sqrt{G}$ for each of the Baseline and Compression specimens. It would be expected that specimens cyclically loaded at high SERRs would have objectively higher amounts of damage within the layup, as per the definition of SERR. Sub-figure a) shows that the Baseline specimen's intralaminar crack quantity decreases a small amount with increasing SERR range which is not expected. The inner plys experience minor increases in intralaminar crack counts, however the overall count is down. In the Compression specimens it can be seen that an 8% increase in intralaminar crack quantity is seen based on total crack count within the matrix for increasing SERR range. A 31% increase in crack quantity is seen in the outer plys. This appears to reflect what is physically expected in a material loaded with increasing SERR ranges.

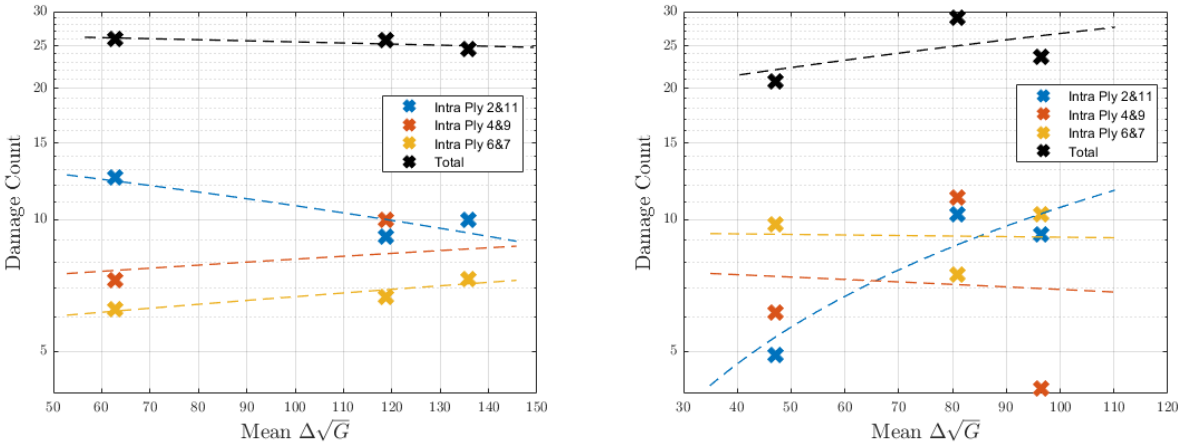

(a) Baseline specimens only

(b) Compression specimens only

Figure 10.1. Analysis of mean SERR range by lead crack intralaminar damage count

Figure 10.2 similarly shows the delamination lengths along the lead crack profile against the SERR range the specimen underwent. As was discussed, there was a significant difference in the amount of delamination damage within the Compression specimens than the Baseline specimens due to the large compressive stresses imparted into the specimens before cyclic loading causing severe damage. For increasing SERR range, the Baseline specimen increased delamination length by approximately 20% for the same amount of cycles. The outer-plys saw no trend in general however the inner plys saw substantial increases. For the Compression specimen, a nonphysical reduction in delamination length was seen at higher SERR ranges. This is likely due to material scatter, or differences in the way the specimen was loaded in monotonic compression. Specimen 1-2-5 (Compression, Medium Load) may be an outlier in this way as it has significantly higher delamination levels than any other specimen.

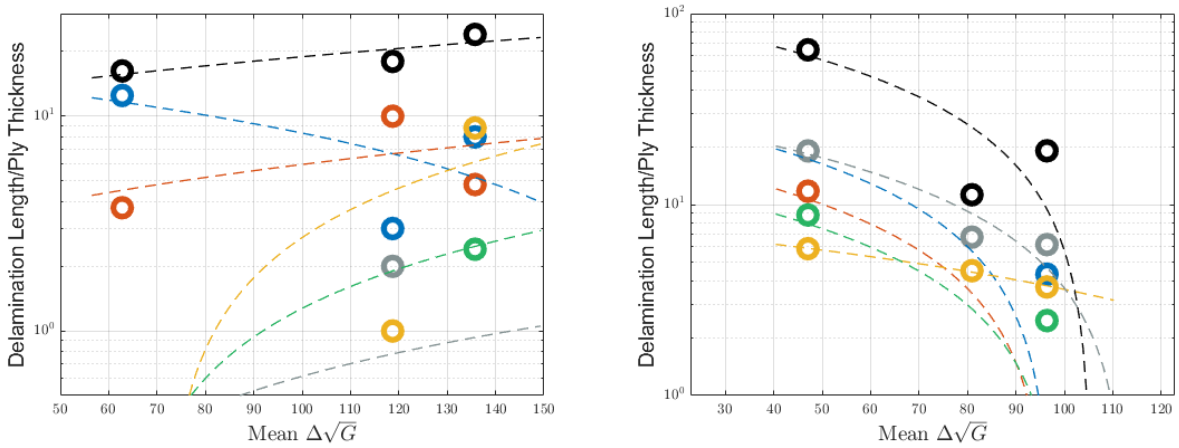

(a) Baseline specimens only

(b) Compression specimens only

(c) Legend

Figure 10.2. Analysis of mean SERR range by delamination length

The SERR parameter, $\Delta\sqrt{G}$, therefore does seem to have a physical connection to the SERR range fatigue results in Figure 8.6, however the physical energy released from crack extensions are not necessarily for the same damage growth mechanism (in the few samples analyzed), as seen by the Baseline specimen growing through predominately delamination along the lead crack and the Compression specimens growing through increased intralaminar cracking along the lead crack. More microscopy analysis is recommended to verify that these damage mechanism trends are persistent across a larger dataset.

Whilst the differences in damage quantity appear to be connected to the SERR it does not necessarily account for the order of magnitude of scatter seen in the maximum SERR and SERR range in the $[\pm 45_3]_s$ specimens. Why the same specimens tested at higher mean stresses have lower SERR ranges, or why Baseline specimens are sometimes more critical than their damage counterparts remains unknown. The damage growth within a multi-

directional laminate is therefore complex and its damage tolerant properties may rely on the damage mechanisms present, loading and individual specimen differences.

There is potential that the large scatter in results may be due to only calculating crack growth from only a single outer ply, whereas the SERR metrics take into account damage across the laminate thickness, and not necessarily just along the lead crack. For damage assessment, the cross-section was taken along the outer-ply intralaminar crack as visible from the surface, however there is also potential that intralaminar cracks or delaminations grew in the -45° plys (which are not visible) in equal or greater quantity or severity. Further computed tomography work to look across all plys, or ultrasonic inspection for bulk damage area analysis, may be useful for further analysing CT specimens loaded in fatigue for this reason.

Due to the large scatter of the fatigue results, a damage tolerant, 3-standard deviation analysis for $\Delta\sqrt{G}$ would be difficult. To rectify this issue, the modified Hartman-Schijve equation similitude parameter, $\Delta\kappa$ was implemented from Jones et al.[18], a seen in Figure 8.10. This was able to greatly reduce the scatter of all curves and form a line of best fit with the equation $da/dN = 7.93\text{e}-49 \cdot \Delta\kappa^{20.145}$, and a R^2 equal to 0.78. This was a lower fit than desired for a similitude parameter, however the reduction of scatter should allow the calculation of an upper bound relationship. Yao et al.[13] and Jones et al.[23] discuss the calculation of the upper bound relation which involves solving Equation 2.2 with the 3-standard deviation values of the constants $A = G_{c0}$ (quasi-static value of the initiation fracture energy) and ΔG_{thr}. It was not possible to calculate this for this paper as both papers do not make it immediately obvious how to solve for $\Delta\sqrt{G}$ with the a large spread of G_{max} values in the denominator.

10.2.2 Potential Stored Energy, U

Per Section 8.7, the average strain energy release rate of each specimen was analysed through the change in potential energy each cycle (Equation 2.7). The average SERR (G^*) is determined to be the inverse gradient of the change in stored potential energy per cycle and the crack growth rate as per Equation 2.8[26], divided by thickness. The function dU/dN

or dU_{cycle}/dN has also been proposed to be a similitude parameter in its own right [77, 15, 78]. Much better alignment of results was seen using this method with the coefficient of determination exceeding 0.95 in both layups.

This method was also able to show that on average each specimen type (Baseline, Impact, Compression) performed differently. This was intuitively expected but was not an outcome possible with the modified Hartman-Schijve equation similitude parameter. Additionally, the calculation of U_{cycle} does not involve the use of crack length which makes its analysis against the crack growth rate (of the visible lead crack) possible for the $[\pm 45_2/90_2]_s$ specimen. The ease of determination of this parameter from test results and its ability to more readily show differences in energy required per crack growth rates for damaged specimens may potentially make its appeal as a similitude parameter.

In order to assess the use of performance of each specimen type, the relation of the change in potential energy per cycle, per cycle (dU_{cycle}/dN) against the load it was tested at was analysed to ensure no correlation existed. This occurred in Figure 10.3 a) and b). The overall material line of best fit as calculated for Figure 8.12 and 8.13 is plotted against the line of best fit for the tests carried out at low, medium and high load levels. All lines of best fits exceed $R^2 = 0.97$. Both sub-figures a) and b) have a similar relation with the specimens cyclically loaded at the low mean stresses having a faster crack growth rate at low energies than the damage specimens, and having lower crack growth rates at high energies. The fact that this cross-over occurs at the approximate mean crack growth rate and the mean dU_{cycle}/dN likely means that these curves are actually converged to the material mean fit, and thus the determination is made that no correlation between energy release rate and crack growth rate for different mean stresses exists - i.e. the crack growth rate at various energy levels is a material property. This is as expected.

Figure 10.3 c) and d) show the line of best fits for different specimen types (Baseline, Impact and Compression). The expected trend is seen in these - much less energy is required in the compression specimens than in the Baseline/Impact specimens, with an order of magnitude less energy per cycle required in the Compression specimens than in the material standard at a threshold crack growth rate of $da/dN = 10^{-10}$ $m/cycle$. The Impact specimen similarly requires less energy per crack extension, but only by a factor of ~2. This accounts

for the residual damage within both specimen types after creation in Chapters 5 and 6 making damage growth easier within a laminate.

Sub-figure d) looks at the $[\pm 45_2/90_2]_s$ specimen. In general it is seen to perform close to the material's overall fit. This may be due to the relatively unobstructed damage growth in each of the specimens in the true lead crack that was seen running the centre 90° plys of Specimen 2-1-7, and is likely on all other $[\pm 45_2/90_2]_s$ specimens. The $[\pm 45_2/90_2]_s$ layup in general saw greatly reduced damage count on the ±45° lead crack as seen from the surface, so most energy was likely expended extending the crack on the centre plys leading to very similar energy release rates per crack growth in both damaged and baseline specimens.

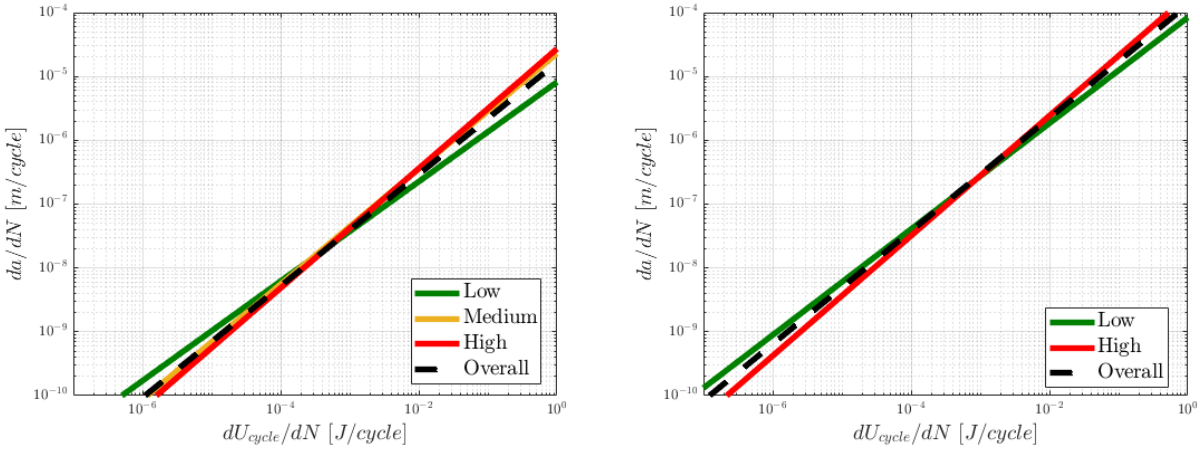

(a) Load level fit $[\pm 45_3]_s$

(b) Load level fit $[\pm 45_2/90_2]_s$

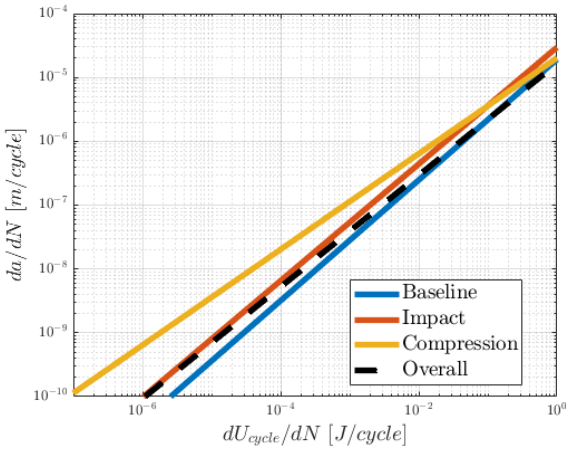

(c) Specimen type fit $[\pm 45_3]_s$

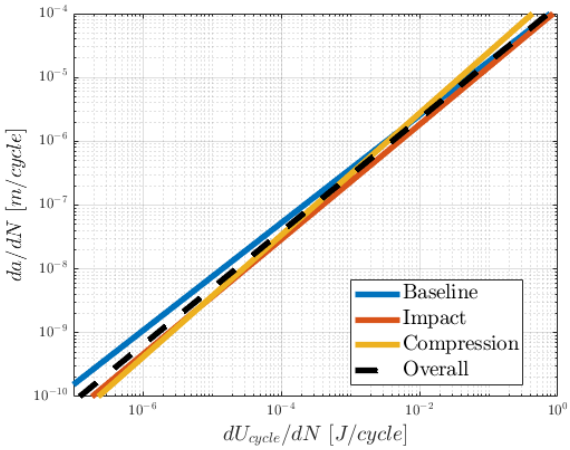

(d) Specimen type fit $[\pm 45_2/90_2]_s$

Figure 10.3. Change in potential energy per cycle dU_{cycle}/N analysis

The use of G^* to readily show the decreased energy required to grow damaged specimens was also shown in quasi-static loading. Figure 7.6 shows that in the an order to generate the same crack extension, the Compression sample required an order of magnitude less energy than the Baseline specimen for the $[\pm 45_3]_s$ layup. The Impact was equally shown to require slightly increased energy to the Baseline, which may relate to the impact site showing crack growth in addition to the lead crack. In the $[\pm 45_2/90_2]_s$ layup, the Compression and Impact specimens were shown to both require less energy for the same crack extension than the Baseline.

Amaral et al.[26] found that for the same layup, rougher fracture surfaces or more damage is expected for specimens with a higher dU/dN as more energy is being applied per increment of crack. They found this to be the case by looking at the relative roughness of the fracture surface of DCB specimens, however this roughness was not quantified. In this study's $[\pm 45_3]_s$ Baseline and Compression specimens, it was shown in Figure 10.3c that the Baseline specimens required more energy per crack extension, and hence per Amaral's work, more or rougher damage is expected. Figure 9.13 shows that increased damage is seen in the form of intralaminar cracking on the Baseline specimens but not in delamination. The intralaminar crack increase is however small. The total damage count in each specimen type is seen in Figure 10.4.

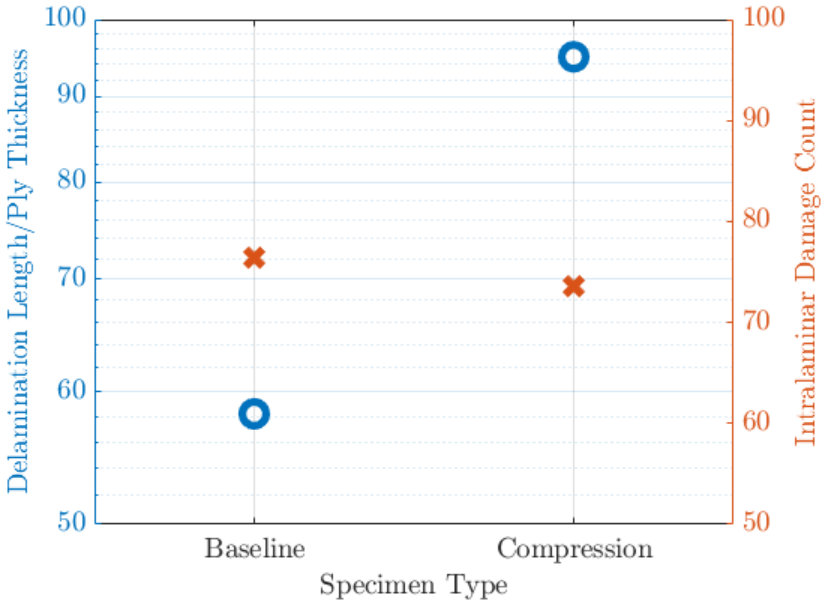

Figure 10.4. Total damage in each specimen type

Figure 10.4 however does not take into account the qualitative damage features within lead crack surfaces. Figure 6.5 shows the cross-section of the lead crack in a Compression sample and Figure 9.4 and 9.10 show two examples of the cross-section of a Baseline $[\pm 45_3]_s$ lead crack. Comparison of the nature of the damage shows that the Baseline specimens have much harsher lead crack surfaces, compared the Compression sample which has a relatively benign surface apart from the initial compression damage features. In general, the Baseline specimen appears to have more warping of plys and increased intralaminar crack growth in the +45° plys following the lead crack (the alternate plys not specified in Figure 10.4 which looked at -45° plys only).

Amaral et al.[26] also look at the normalisation between quasi-static and fatigue average strain energy release rate per cycle (G^*) as they are mathematically equivalent parameters. The comparison can be viewed in the Appendix however it is not further discussed here.

11. CONCLUSION

This study has investigated fatigue crack growth in carbon fibre compact tension specimens. Two layups were tested, $[\pm 45_3]_s$ and $[\pm 45_2/90_2]_s$, each in a mixture of damage states. Baseline, Impact damaged and Compression damaged specimens were examined in order to analyse the damage tolerance of a layup in multiple damage states and load levels in order to gain an understanding how strain energy release rate was affected. In total 18 specimens were tested.

The fatigue loading of a multi-directional laminate Compact Tension specimen is a much more complex stress state than the single dimension crack growth measured in Double Cantilever Beam tests. Interpretation of the results was therefore complicated due to the range of factors that could be involved in fatigue crack growth within the specimen.

The following was points of interest were made:

1. A Vikers-hardness indenter proved a reliable and quick way to impart damage into CFRP specimens consistent with impact damage seen in literature.

2. A single monotonic compression load to the material's proportional limit created damage formations consistent with kink-bands on outer plys of the laminate, and significant internal damage.

3. Strain energy release rate parameters G_{max} and $\Delta\sqrt{G}$ had significant scatter across specimens tested with the same layup and the same mean stress levels.

4. Intuitive results were not always obtained. There was little correlation between G_{max}, $\Delta\sqrt{G}$ and expected results for different damage and loading conditions.

   (a) Only two of four fatigue load levels for the $[\pm 45_3]_s$ specimens saw the Baseline specimen being more damage tolerant than the damaged specimens.

   (b) Little correlation was seen between SERR and the mean stress it was tested at.

5. Cross-sectioning of the lead crack, for the samples analyzed, saw:

   (a) Baseline specimens tended to grow through delamination.

(b) Impact specimens had no increase in delamination at the impact site but saw intralaminar crack growth on the outer plys.

(c) Compression specimens tended to grow intralaminar cracks perpendicular to the lead crack.

6. $\Delta\sqrt{G}$ appeared to have a connection to increasing damage across the lead crack cross-section. This does not necessarily explain the order of magnitude SERR scatter but does show increased damage was present in the specimen at higher SERRs as per the definition of SERR.

7. Due to the complex damage make-up of the lead crack cross-section as examined under microscopy, and as the calculated SERR will be affected by damage across the whole specimen, it is likely that the inherent interaction of intralaminar and interlaminar cracking in a fatigue damaged composite has a large effect on SERR measured. This may be why SERR scatter was an order of magnitude higher in this work than in literature assessing DCB specimens.

8. The use of da/dn vs dU_{cycle}/dN (and therefore also the average SERR per cycle parameter G^*) proved a more reliable way to analyse results and attain results similar to what was expected.

9. The parameter dU_{cycle}/dN showed higher alignment of specimen data than the Hartman-Schijve Similitude parameter $\Delta\kappa$ for the data attained.

It is possible that the comparison of measurement of the lead crack on the outer ply to SERR has led to error as the SERR is a whole of laminate metric rather crack growth rate attained which is only looking at a single outer ply. For this reason further work with computed tomography or ultrasonic inspection may be valuable.

12. RECOMMENDATIONS

The following recommendations are made:

1. Further testing should be done on Compact Tension specimens that have a larger thickness to width ratio to stop out-of-plane bending. Otherwise, the use of of a more sophisticated jig will be required to stop out-of-plane bending.
2. Use clip-on extensometer to measure specimen displacement.
3. Use compliance or a back face strain gauge to calculate crack length.
4. Conduct fatigue testing of DCB specimens of the same material to assess SERR scatter.
5. Consider repeating work with:
   (a) A higher resolution camera to increase crack growth rate accuracy, or
   (b) Ultrasonic inspection to look at change in damage area rather than lead crack length, or
   (c) Computed tomography to ensure that the lead crack across all plys is being analysed.

Bibliography

[1] W Roeseler, B Sarh, and M Kismarton. "Composite Structure: The First Hundred Years". In: *International Conference on Composite Materials*. 2007.

[2] Federal Aviation Authority. *Airworthiness advisory circular No: 20-107A: Tech. Rep.* Tech. rep. 1984, pp. 1–11.

[3] S Chisholm et al. "Forty Years of Structural Durability and Damage Tolerance at Boeing Commercial Airplanes". In: *Boeing Technical Journal* (2016).

[4] J Rouchon. "Fatigue and Damage Tolerance Evaluation of Structures : The Composite Materials Response". In: *International Committee on Aeronautical Fatigue* May (2009).

[5] Federal Aviation Authority and Federal Aviation Authority. *Airworthiness advisory circular No: 20-107B: Tech. rep.* Tech. rep. 2. 2009, pp. 1–3.

[6] A Baker and M Scott. *Composite Materials for Aircraft Structures, Second Edition*. Third Edit. AIAA, 2004. DOI: 10.2514/5.9781600861680.0081.0112.

[7] P Irving and C Soutis. *Polymer Composites in the Aerospace Industry*. Second Edi. Woodhead Publishing, 2020. ISBN: 978-0-08-102679-3.

[8] B. Harris. *A historical review of the fatigue behaviour of fibre-reinforced plastics*. Woodhead Publishing Limited, 2003, pp. 3–35. DOI: 10.1533/9781855738577.1.3.

[9] W Stinchcomb and C Bakis. "Fatigue Behavior of Composite Laminates". In: *Composite Materials Series*. Vol. 4. C. 1991, pp. 105–180. DOI: 10.1016/B978-0-444-70507-5.50008-1.

[10] C Kassapoglou. "Stiffness & strength of composite structural elements". In: *Polymer Composites in the Aerospace Industry*. 2020, pp. 147–193. URL: https://doi.org/10.1016/B978-0-08-102679-3.00007-1.

[11] T.P. Philippidis and A.P. Vassilopoulos. *Fatigue strength of composites under variable plane stress*. Woodhead Publishing Limited, 2003, pp. 504–525. DOI: 10.1533/9781855738577.4.504.

[12] L Molent and A Haddad. "A critical review of available composite damage growth test data under fatigue loading and implications for aircraft sustainment". In: *Composite Structures* 232.July 2019 (2020), p. 111568. ISSN: 02638223. DOI: 10.1016/j.compstruct.2019.111568.

[13] L Yao et al. "Delamination fatigue growth in polymer-matrix fibre composites: A methodology for determining the design and lifing allowables". In: *Composite Structures* 196.May (2018), pp. 8–20. ISSN: 02638223. DOI: 10.1016/j.compstruct.2018.04.069.

[14] R Jones et al. "Delamination growth in polymer-matrix fibre composites and the use of fracture mechanics data for material characterisation and life prediction". In: *Composite Structures* 180 (Nov. 2017), pp. 316–333. ISSN: 02638223. DOI: 10.1016/j.compstruct.2017.07.097.

[15] L Yao et al. "Discussion on the use of the strain energy release rate for fatigue delamination characterization". In: *Composites Part A: Applied Science and Manufacturing* 66 (Nov. 2014), pp. 65–72. ISSN: 1359835X. DOI: 10.1016/j.compositesa.2014.06.018.

[16] C Rans, R Alderliesten, and R Benedictus. "Misinterpreting the results: How similitude can improve our understanding of fatigue delamination growth". In: *Composites Science and Technology* 71.2 (2011), pp. 230–238. ISSN: 02663538. DOI: 10.1016/j.compscitech.2010.11.010.

[17] M Hojo et al. "Effect of stress ratio on near-threshold propagation of delimination fatigue cracks in unidirectional CFRP". In: *Composites Science and Technology* 29.4 (Jan. 1987), pp. 273–292. ISSN: 02663538. DOI: 10.1016/0266-3538(87)90076-5.

[18] R Jones, W Hu, and A J Kinloch. "A convenient way to represent fatigue crack growth in structural adhesives". In: (2014). DOI: 10.1111/ffe.12241.

[19] I Simon, L Banks-Sills, and V Fourman. "Mode I delamination propagation and R-ratio effects in woven composite DCB specimens for a multi-directional layup". In: *International Journal of Fatigue* 96 (Mar. 2017), pp. 237–251. ISSN: 01421123. DOI: 10.1016/j.ijfatigue.2016.12.005.

[20] L Yao et al. “A novel total fatigue life model for delamination growth in composite laminates under generic loading”. In: *Composite Structures* 258 (Feb. 2021), p. 113402. ISSN: 02638223. DOI: 10.1016/j.compstruct.2020.113402.

[21] R Jones et al. “Crack growth in adhesives: Similitude and the Hartman-Schijve equation”. In: *Composite Structures* 273 (Oct. 2021), p. 114260. ISSN: 02638223. DOI: 10.1016/j.compstruct.2021.114260.

[22] E. Altus and O. Ishai. “Transverse cracking and delamination interaction in the failure process of composite laminates”. In: *Composites Science and Technology* 26.1 (1986), pp. 59–77. ISSN: 02663538. DOI: 10.1016/0266-3538(86)90056-4.

[23] R Jones and A Kinloch. “A way forward for industry to determine valid cyclic-fatigue relationships for polymer-matrix fibre composites”. In: *Procedia Structural Integrity*. Vol. 28. Elsevier, Jan. 2020, pp. 26–38. DOI: 10.1016/j.prostr.2020.10.005.

[24] M Czabaj and J Ratcliffe. “Comparison of intralaminar and interlaminar mode I fracture toughnesses of a unidirectional IM7/8552 carbon/epoxy composite”. In: *Composites Science and Technology* 89 (2013), pp. 15–23. DOI: 10.1016/j.compscitech.2013.09.008.

[25] G. R. Irwin. “Analysis of Stresses and Strains Near the End of a Crack Traversing a Plate”. In: *Journal of Applied Mechanics* 24.3 (Sept. 1957), pp. 361–364. ISSN: 0021-8936. DOI: 10.1115/1.4011547.

[26] L Amaral et al. “The relation between the strain energy release in fatigue and quasi-static crack growth”. In: *Engineering Fracture Mechanics* 145.December 2019 (2015), pp. 86–97. ISSN: 00137944. DOI: 10.1016/j.engfracmech.2015.07.018.

[27] John Alan Pascoe. “Slow-growth damage tolerance for fatigue after impact in FRP composites: Why current research won’t get us there”. In: *Procedia Structural Integrity* 28 (2020), pp. 726–733. ISSN: 24523216. DOI: 10.1016/j.prostr.2020.10.084.

[28] G Murri. “Evaluation of delamination onset and growth characterization methods under mode i fatigue loading”. In: *27th Annual Technical Conference of the American Society for Composites 2012, Held Jointly with 15th Joint US-Japan Conference on Composite Materials and ASTM-D30 Meeting* February (2012), pp. 601–620.

[29] X Ni et al. “Interlaminar to intralaminar mode I and II crack bifurcation due to aligned carbon nanotube reinforcement of aerospace-grade advanced composites”. In: *Composites Science and Technology* 190.December 2019 (2020), pp. 19–27. ISSN: 02663538. DOI: 10.1016/j.compscitech.2020.108014.

[30] S. S. Wang. “Fracture Mechanics for Delamination Problems in Composite Materials.” In: *Studies in Applied Mechanics* 17.May (1984), pp. 369–383. DOI: 10.1016/b978-0-444-42169-2.50029-2.

[31] Al Ortiz-morales et al. “3D in-situ X-ray tomography analysis of progressive damage in carbon fiber epoxy laminate composites during monotonic tensile loading”. In: *Engineering Fracture Mechanics* 246.February (2021), p. 107626. ISSN: 0013-7944.

[32] S. C. Garcea, Y. Wang, and P. J. Withers. *X-ray computed tomography of polymer composites*. Mar. 2018. DOI: 10.1016/j.compscitech.2017.10.023.

[33] P Wright et al. “Ultra high resolution computed tomography of damage in notched carbon fiber-epoxy composites”. In: *Journal of Composite Materials* 42.19 (2008), pp. 1993–2002. ISSN: 00219983. DOI: 10.1177/0021998308092211.

[34] I Hanhan et al. “Slow crack growth in laminate composites via in-situ X-ray tomography and simulations”. In: *International Journal of Fatigue* 155 (Feb. 2022), p. 106612. ISSN: 01421123. DOI: 10.1016/j.ijfatigue.2021.106612.

[35] Y Feng et al. “Investigation on impact damage evolution under fatigue load and shear-after-impact-fatigue (SAIF) behaviors of stiffened composite panels”. In: *International Journal of Fatigue* 100 (2017), pp. 308–321. ISSN: 01421123. DOI: 10.1016/j.ijfatigue.2017.03.046.

[36] G Davies and P Irving. *Impact, post-impact strength, and post-impact fatigue behavior of polymer composites*. Elsevier Ltd, 2019, pp. 303–330. ISBN: 9780081026793. DOI: 10.1016/B978-0-08-102679-3.00011-3.

[37] D Hull and YB Shi. “Damage mechanism characterization in composite damage tolerance investigations”. In: *Composite Structures* 23.2 (1993), pp. 99–120. ISSN: 02638223. DOI: 10.1016/0263-8223(93)90015-I.

[38] W Cantwell and J Morton. “The impact resistance of composite materials - a review”. In: *Composites* 22.5 (Sept. 1991), pp. 347–362. ISSN: 00104361. DOI: 10.1016/0010-4361(91)90549-V.

[39] H Han and S Choi. *The Effect of Loading Parameters on Fatigue of Composite Laminates: Part IV Information Systems*. July. Washington, D.C. : 2001, p. 58. URL: http://hdl.handle.net/2027/uc1.c101370264.

[40] E Correa et al. “Microscopical observations of inter-fibre failure under tension”. In: *Composites Science and Technology* 155 (2018), pp. 213–220. ISSN: 02663538. DOI: 10.1016/j.compscitech.2017.12.009.

[41] F París, E Correa, and V Mantič. “Kinking of transversal interface cracks between fiber and matrix”. In: *Journal of Applied Mechanics, Transactions ASME* 74.4 (Sept. 2007), pp. 703–716. ISSN: 00218936. DOI: 10.1115/1.2711220.

[42] B Budiansky and N Fleck. “Compressive Kinking of Fiber Composites: A Topical Review”. eng. In: *Applied Mechanics Reviews* 47.6S (June 1994), S246–S250. ISSN: 0003-6900. DOI: 10.1115/1.3124417.

[43] S Pinho. “Modelling composites failure laminated of using physically-based failure models”. PhD thesis. Imperial College London, 2005, pp. 1–226.

[44] S Kyriakides et al. “On the compressive failure of fiber reinforced composites”. In: *International Journal of Solids and Structures* 32.6-7 (1995), pp. 689–738. ISSN: 00207683. DOI: 10.1016/0020-7683(94)00157-R.

[45] S Hsu, T Vogler, and S Kyriakides. “On the axial propagation of kink bands in fiber composites : Part ii analysis”. In: *International Journal of Solids and Structures* 36.4 (1999), pp. 575–595. ISSN: 00207683. DOI: 10.1016/S0020-7683(98)00030-4.

[46] S Pimenta et al. “A micromechanical model for kink-band formation: Part I — Experimental study and numerical modelling”. In: *Composites Science and Technology* 69.7-8 (June 2009), pp. 948–955. ISSN: 02663538. DOI: 10.1016/j.compscitech.2009.02.010.

[47] A Bergan and S Garcea. “In-situ observations of longitudinal compression damage in carbon-epoxy cross ply laminates using fast synchrotron radiation computed tomography”. In: *32nd Technical Conference of the American Society for Composites 2017* 4 (2017), pp. 2988–3003. DOI: 10.12783/asc2017/15404.

[48] E. K. Gamstedt and B. A. Sjögren. “Micromechanisms in tension-compression fatigue of composite laminates containing transverse plies”. In: *Composites Science and Technology* 59.2 (Feb. 1999), pp. 167–178. ISSN: 02663538. DOI: 10.1016/S0266-3538(98)00061-X.

[49] Hextow. *IM7 Technical Data Sheet*. Tech. rep. 2020, pp. 1–2.

[50] Cycom. *5320-1 Technical Data Sheet*. Tech. rep. 0. 2021, pp. 1–11.

[51] ASTM. “ASTM E1820, Standard Test Method for Measurement of Fracture Toughness”. In: *Astm* November (2015), pp. 1–54.

[52] ISO/TC 213. *ISO 286-1:2010 Geometrical product specifications (GPS) — ISO code system for tolerances on linear sizes — Part 1: Basis of tolerances, deviations and fits*. Tech. rep. ISO, 2010.

[53] Basler AG. *Pixel Formats*. 2021. URL: https://docs.baslerweb.com/pixel-format.

[54] Allied Vision. “Getting Started with MATLAB Required host adapter cards Installing Vimba”. In: (), pp. 1–10.

[55] Allied Vision. “Manta Technical Manual V7.2.0”. In: (2020). URL: http://www.alliedvision.com/fileadmin/content/documents/products/cameras/Manta/techman/Manta_TechMan.pdf.

[56] ASTM. “ASTM D3479, Standard Test Method for Tension-Tension Fatigue of Polymer Matrix Composite Materials”. In: *Annual Book of ASTM Standards* i.August (2012), p. 6. DOI: 10.1520/D3479.

[57] ASTM. “ASTM E647, Standard Test Method for Measurement of Fatigue Crack Growth Rates”. In: *American Society for Testing and Materials* 03 (2014), pp. 1–50. DOI: 10.1520/E0647-15E01.

[58] H Liu et al. “An experimental method to determine the intralaminar fracture toughness of high-strength carbon-fibre reinforced composite aerostructures”. In: *Aeronautical Journal* 122.1255 (2018), pp. 1352–1370. ISSN: 00019240. DOI: 10.1017/aer.2018.78.

[59] E Correa et al. “Effects of the presence of compression in transverse cyclic loading on fibre-matrix debonding in unidirectional composite plies”. eng. In: *Composites Part A: Applied Science and Manufacturing* 38.11 (2007), pp. 2260–2269. ISSN: 1359835X. DOI: 10.1016/j.compositesa.2006.11.002.

[60] K Im, S Kim, and I Yang. “Effects of temperature on impact damages in CFRP composite laminates”. In: *Composites Part B:Engineering* 32.8 (Dec. 2001), pp. 669–682. ISSN: 13598368. DOI: 10.1016/S1359-8368(01)00046-4.

[61] D Cartié and P Irving. “Effect of resin and fibre properties on impact and compression after impact performance of CFRP”. In: *Composites Part A: Applied Science and Manufacturing* 33.4 (Apr. 2002), pp. 483–493. ISSN: 1359-835X. DOI: 10.1016/S1359-835X(01)00141-5.

[62] M Found, I Howard, and A Paran. “Size effects in thin CFRP panels subjected to impact”. In: *Composite Structures* 38.1-4 (1997), pp. 599–607. ISSN: 02638223. DOI: 10.1016/S0263-8223(97)00098-6.

[63] C Völlmecke and R Zidek. “Kink banding in laminated composite structures”. In: *Pamm* 15.1 (2015), pp. 237–238. DOI: 10.1002/pamm.201510109.

[64] Y Wang et al. “X-ray computed tomography study of kink bands in unidirectional composites”. In: *Composite Structures* 160 (Jan. 2017), pp. 917–924. ISSN: 02638223. DOI: 10.1016/j.compstruct.2016.10.124.

[65] S Hörrmann et al. “The effect of fiber waviness on the fatigue life of CFRP materials”. In: *International Journal of Fatigue* 90 (Sept. 2016), pp. 139–147. ISSN: 01421123. DOI: 10.1016/j.ijfatigue.2016.04.029.

[66] R Gutkin et al. “On the transition from shear-driven fibre compressive failure to fibre kinking in notched CFRP laminates under longitudinal compression”. In: *Composites*

Science and Technology 70.8 (Aug. 2010), pp. 1223–1231. ISSN: 02663538. DOI: 10.1016/j.compscitech.2010.03.010.

[67] M Ahmer Wadee et al. "Geometric modelling of kink banding in laminated structures". In: *Philosophical Transactions of the Royal Society A: Mathematical, Physical and Engineering Sciences* 370.1965 (2012), pp. 1827–1849. ISSN: 1364503X. DOI: 10.1098/rsta.2011.0380.

[68] D Roylance. "Introduction to Fracture Mechanics". In: *MIT Courseware online* (2001).

[69] JM Slepetz and L Carlson. "Fracture of Composite Compact Tension Specimens". In: *Fracture Mechanics of Composites* STP 593 (1975), pp. 143–143. DOI: 10.1520/stp34796s.

[70] ASTM. "ASTM D6671, Standard Test Method for Mixed Mode I-Mode II Interlaminar Fracture Toughness of Unidirectional Fiber Reinforced Polymer Matrix Composites". In: *ASTM International* i.Mode I (2006), p. 15. DOI: 10.1520/D6671.

[71] N Perez. *Fracture Mechanics*. Cham: Springer International Publishing, 2017, pp. 1–418. ISBN: 978-3-319-24997-1. DOI: 10.1007/978-3-319-24999-5.

[72] A Bower. *Applied Mechanics of Solids*. CRC Press, Oct. 2009, pp. 1–795. ISBN: 9781439802489. DOI: 10.1201/9781439802489.

[73] L Molent and C Forrester. "The lead crack concept applied to defect growth in aircraft composite structures". In: *Composite Structures* 166 (2017), pp. 22–26. ISSN: 02638223. DOI: 10.1016/j.compstruct.2016.12.076.

[74] D Virkler, B Hillberry, and P Goel. "The statistical nature of fatigue crack propagation". In: *Journal of Engineering Materials and Technology, Transactions of the ASME* 101.2 (1979), pp. 148–153. ISSN: 15288889. DOI: 10.1115/1.3443666.

[75] R Jones, S Stelzer, and A Brunner. "Mode I, II and Mixed Mode I/II delamination growth in composites". In: *Composite Structures* 110.1 (Apr. 2014), pp. 317–324. ISSN: 02638223. DOI: 10.1016/j.compstruct.2013.12.009.

[76] R Jones, A Kinloch, and W Hu. "Cyclic-fatigue crack growth in composite and adhesively-bonded structures: The FAA slow crack growth approach to certification and the problem of similitude". In: *International Journal of Fatigue* 88 (2016), pp. 10–18. ISSN: 01421123. DOI: 10.1016/j.ijfatigue.2016.03.008.

[77] R Jones. *Presentation at US-Japan-Aust Workshop March 2021*. 2021.

[78] L Yao et al. "Mode I fatigue delamination growth with fibre bridging in multidirectional composite laminates". In: *Engineering Fracture Mechanics* 189 (2018), pp. 221–231. ISSN: 00137944. DOI: 10.1016/j.engfracmech.2017.11.013.

[79] R Khan et al. "Crack closure and fibre bridging during delamination growth in carbon fibre/epoxy laminates under mode i fatigue loading". In: *Composites Part A: Applied Science and Manufacturing* 67 (2014), pp. 201–211. ISSN: 1359835X. DOI: 10.1016/j.compositesa.2014.08.028.

[80] A Brunner, N Murphy, and G Pinter. "Development of a standardized procedure for the characterization of interlaminar delamination propagation in advanced composites under fatigue mode I loading conditions". In: *Engineering Fracture Mechanics* 76.18 (2009), pp. 2678–2689. ISSN: 00137944. DOI: 10.1016/j.engfracmech.2009.07.014.

[81] B Bak et al. *Delamination under fatigue loads in composite laminates: A review on the observed phenomenology and computational methods*. Nov. 2014. DOI: 10.1115/1.4027647.

[82] A Brunner, B Blackman, and P Davies. "A status report on delamination resistance testing of polymer-matrix composites". In: *Engineering Fracture Mechanics* 75.9 (2008), pp. 2779–2794. ISSN: 00137944. DOI: 10.1016/j.engfracmech.2007.03.012.

[83] T Khan, H Kim, and H Kim. "Fatigue delamination of carbon fiber-reinforced polymer-matrix composites". In: *Failure Analysis in Biocomposites, Fibre-Reinforced Composites and Hybrid Composites*. Woodhead Publishing, Jan. 2018, pp. 1–28. ISBN: 9780081022931. DOI: 10.1016/B978-0-08-102293-1.00001-2.

[84] R Khan, R Alderliesten, and R Benedictus. “Two-parameter model for delamination growth under mode i fatigue loading (Part A: Experimental study)”. In: *Composites Part A: Applied Science and Manufacturing* 65 (Oct. 2014), pp. 192–200. ISSN: 1359835X. DOI: 10.1016/j.compositesa.2014.06.007.

APPENDIX

The relation between the average strain energy release rate per cycle, G^*, for quasi-static and fatigue growth in both layup types is shown in Table 13.1.

Table 13.1. G^* for Quasi-Static and Fatigue Crack Growth

Specimen Layup	**Damage Type**	**Test Type**	$\mathbf{G^*}$ $[\mathbf{MJ/m^2}]$	$\frac{\mathbf{G^*_{fatigue}}}{\mathbf{G^*_{quasi-static}}}$	**Mean Ratio for Layup**
$[\pm 45_3]_s$	Baseline	Fatigue	24.327	44.231	39.147
		Monotonic	0.550		
	Impact	Fatigue	15.780	26.212	
		Monotonic	0.602		
	Compression	Fatigue	23.123	46.997	
		Monotonic	0.492		
$[\pm 45_2/90_2]_s$	Baseline	Fatigue	3.768	2.628	3.298
		Monotonic	1.343		
	Impact	Fatigue	4.049	4.098	
		Monotonic	0.988		
	Compression	Fatigue	2.085	3.169	
		Monotonic	0.658		